PERFORMANCE ANALYSIS OF TRELLIS CODES TRANSMITTED OVER FADING CHANNELS

by

Chinthananda Tellambura

B.Sc., University of Moratuwa, 1986

M.Sc., University of London, 1988

A DISSERTATION SUBMITTED IN PARTIAL FULFILLMENT
OF THE REQUIREMENTS FOR THE DEGREE OF
DOCTOR OF PHILOSOPHY

in the Department of Electrical and Computer Engineering

We accept this dissertation as confirming
to the required standard.

Dr. V. K. Bhargava, Supervisor (Department of ECE)

Dr. Q. Wang, Departmental Member (Department of ECE)

Dr. P. Agathoklis, Departmental Member (Department of ECE)

Dr. D. M. Miller, Outside Member (Department of CS)

Dr. J. K. Cavers, External Examiner (Simon Fraser University)

Supervisor: **Professor Vijay K. Bhargava**

ABSTRACT

Trellis coded modulation (TCM) schemes, due to their bandwidth efficiency and coding gain, have been proposed for multipath fading (MF) channels. The object of this research is to analyze the performance of TCM schemes in MF channels. While many excellent studies have already been reported, they share some of the following restrictions: (1) an assumption of ideal channel measurements and ideal interleaving, (2) use of Chernoff bounds, which are loose in this case, (3) analysis of only the Rayleigh channel, ignoring the Rician channel, and (4) reliance on computer simulation to get the actual performance. Extending analytical results without these restrictions is addressed in this work.

This thesis derives a saddle point approximation (SAP) method to compute the pairwise error probability (PEP) of TCM schemes transmitted over Rician fading channels. It can be applied under several conditions, including finite or ideal interleaving, and is derived for a pilot-tone model, encompassing ideal coherent detection, pilot-tone aided detection, pilot-symbol aided detection, and differential detection. Its accuracy is demonstrated by comparison to the results of numerical integration. Under ideal interleaving, the approximation can be further simplified to an expression, which is in a product form and is much tighter than the ordinary Chernoff bound on the PEP. Also, based on the SAP, the effect of finite interleaving depth on the error performance is studied.

The Canadian mobile satellite (MSAT) channel has been modelled as the sum of lognormal and Rayleigh components. Previously, the performance of TCM schemes in this channel has been obtained via computer simulation. In this thesis, new analytical expressions are derived for the PEP of TCM schemes transmitted over this channel employing ideal interleaving, and the results are substantiated

by means of computer simulation. In addition, first order statistics of absolute and differential phases of a shadowed Rician process are derived.

This thesis presents new performance bounds of TCM schemes over nonindependent (i.e , finite interleaving) Rician fading channels. In addition, for Rayleigh fading channels with an exponential auto-covariance function, bounds resembling those for memoryless channels are derived. The bounds, being more accurate than Chernoff bounds, permit accurate estimation of system performance.

The performance of concatenated coding systems and automatic-repeat-request (ARQ) systems operating on fading channels is addressed. New error expressions, which show asymptotic error behaviour, are derived for systems which use a modified Viterbi decoding algorithm. They allow useful evaluation of the coding gain and throughput.

Finally, the performance of convolutional codes in fading channels is analyzed. An upper bound on the bit error probability, the optimum power split ratio between the data and pilot signals, and the channel cut-off rate are derived.

Examiners:

Dr. V. K. Bhargava, Supervisor (Department of ECE)

Dr. Q. Wang, Departmental Member (Department of ECE)

Dr. P. Agathoklis, Departmental Member (Department of ECE)

Dr. D. M. Miller, Outside Member (Department of CS)

Dr. J. K. Cavers, External Examiner (Simon Fraser University)

Contents

List of Tables

List of Figures

Acknowledgements

I owe a great deal of thanks to my supervisor, Professor Vijay K. Bhargava, for his guidance, inspiration and friendship. I would also like to thank Dr. Qiang Wang for his advice and help with my work. Many thanks are due to the following friends: Ivan Fair for proof reading parts of this thesis and some of my papers, Dave Peterson for proof reading some of my papers, and Roman Pichna for helping me with a few figures in the thesis. Finally, I am grateful to the Canadian Commonwealth Association for funding my research.

Dedication

To My Parents

Notation

List of Abbreviations

ARQ	automatic-repeat-request
AWGN	additive white Gaussian noise
CSI	channel state information
LOS	line-of-sight
MF	multipath fading
PDF	probability density function
PEP	pairwise error event probability
PSAM	pilot symbol assisted modulation
PSK	phase shift keying
PTAM	pilot tone assisted modulation
QAM	quadrature amplitude shift keying
SAP	saddle point approximation
SNR	signal-to-noise ratio
TCM	trellis-coded modulation
VA	Viterbi algorithm
TC-MDPSK	trellis-coded multilevel differential phase shift keying
TC-MPSK	trellis-coded multilevel phase shift keying

List of Principal Symbols

α_k channel gain for the k-th symbol interval

$\hat{\alpha}_k$ channel gain estimate for the k-th symbol interval

b_0 variance of channel gain

b_1 variance of channel gain estimate

Ξ	Viterbi decision variable
$\overline{E}_b$	average bit energy
$\overline{E}_s$	average signal energy
μ	correlation coefficient between α_k and $\hat{\alpha}_k$
N_0	single-sided noise spectral density ratio
γ_s	average signal energy to noise spectral density ratio
k	the time index
$\mathbf{x}$	transmitted codeword
$\hat{\mathbf{x}}$	erroneous codeword
f_D	maximum Doppler frequency
N_d	interleaving depth
N_s	interleaving span
P_b	the average bit error probability
σ^2	variance of additive noise
T_s	channel symbol interval

Chapter 1

Introduction

Mobile communication services have experienced a dramatic growth recently, and this trend is expected to continue unabated in the foreseeable future. Specifically, mobile communications encompass the following scenarios: satellite-mobile, aeromobile, maritime mobile, radio paging, cellular, etc. The ubiquitous term "mobile" refers to the fact that either the transmitter or receiver is capable of moving. In order to meet the ever increasing demand for these services, the service carriers are turning to digital networks where digital techniques such as channel coding can be used to provide robustness against channel impairments.

In this channel (i.e., the transmission medium), the transmitted signal can be degraded in many ways, including shadowing, fading, adjacent and co-channel interference, etc. Since complete characterization of all such degradations would require extremely complicated models, the system designer often resorts to computer simulation and/or field tests.

One prevalent signal degradation mechanism with which we are concerned in this thesis is multipath fading (MF). Consider a typical mobile communication scenario where a radio signal is transmitted between a fixed base station and a moving vehicle. The amplitude and apparent frequency of the received signal varies a great deal (e.g, amplitude fades of 40 dB below the mean level are not uncommon,) and the rate of these variations is directly related to the vehicle speed. Buildings and other structures in the vicinity of the mobile act as independent scatterers, and,

hence, the electromagnetic field at the receiving antenna can be expressed as a linear superposition of a large number of plane waves of random phase and Doppler shift, each being reflected from a distinct scatterer. As a consequence of the central limit theorem, the electromagnetic field components may be approximately described as Gaussian processes [1]. When a direct line-of-sight signal component does not exist, the received signal entirely consists of such scattered components, and its envelope has a Rayleigh distribution, whereas the presence of direct line-of-sight signal component results in a Rician distributed signal envelope. Since excellent discussions of fading channels are available elsewhere [1-3], we content ourselves with this very limited introduction .

Rayleigh fading applies to cellular systems operating in an urban environment where tall buildings may completely block line-of-sight between the mobile and the base station. However, the Rician model is applicable in rural areas and satellite communication systems.

Traditionally, diversity schemes have been used to mitigate the effects of multipath fading. These schemes can be classified into at least three forms: space, frequency, and time diversity. Space diversity schemes rely on the use of multiple antennas (≥ 2), while frequency diversity uses the transmitted signal in different frequencies. In this thesis, we will investigate the use of coding (i.e., time diversity) in MF channels. We concentrate on trellis codes (i.e., with a convolutional type encoder), although most of the results of this study can be extended to block-codes provided that they can be decoded with the Viterbi algorithm (e.g., [4]).

Trellis coded modulation, proposed by Ungerboeck [5], combines power gain and bandwidth efficiency, and hence has spawned a great deal of research. Without any bandwidth expansion, coding gains of 2-3 dB are possible with very simple codes in AWGN channels, while complex codes may provide coding gains in excess of 5 dB (see [6] for the detailed theory and application of TCM). The use of TCM in MF channels, however, can result in even more dramatic coding gains, as we

will see later.

To gain the full benefits of coding requires accurate measurement of channel gain as well as independent fading, just as in the case of maximal-ratio diversity combining. For analytical purposes, we assume that the effect of the channel on the transmitted signal is described by a multiplicative stationary Gaussian process, $\alpha(t)$. Then, making "channel gain measurements" means forming an estimate of $\alpha(t)$ at the receiver.

There are several techniques for obtaining channel gain measurements. One technique is to transmit a pilot-tone (or tones) [7-9] along with the data signal, where the pilot and data signals fall within the coherence bandwidth of the fading process. At the receiver, the pilot tone is extracted with carefully designed filters and is used to provide fading compensation. Secondly, by periodically inserting pilot symbols in the data symbol sequence and optimally filtering them, channel gain estimates can be made [10, 11]. Thirdly, differential techniques exploit the fact that in slow fading channels the channel gain remains roughly constant over several channel symbol intervals.

Taking the channel measurements into account, analyzing the performance of TCM will provide insight into the dominant parameters affecting the performance in this channel, and will be useful in coding system design.

1.1 Previous Results

The following is a survey of some of the relevant papers in the literature (each chapter also gives further citations). Most studies deal with PSK (phase shift keying) signalling, and assume ideal interleaving.

Divsalar and Simon [12] presented the performance of TC-MPSK (trellis-coded multilevel phase shift keying) with or without CSI (channel state information) in Rician fading. The upper bounds on the PEP were obtained via the Chernoff bounding technique. TC-MPSK performance in Rayleigh fading was studied by

Wilson and Leung [13].

The performance of TC-MDPSK (trellis-coded multilevel phase shift keying) was treated in [14, 15] using the Chernoff bounding technique.

The above mentioned studies used the Chernoff bound technique in conjunction with the transfer bound technique to upper bound the average bit error probability (P_b). It turned out that the resulting bounds were rather weak: 3-4 dB (in terms of SNR) away from simulation results. To get more accurate estimates of P_b, Cavers and Ho [16] derived an exact analytical expression of the PEP for the Rayleigh channel; it involves computing residues. Under certain conditions, the residue computation could be simplified (Chan and Bateman [17, 18]).

When the interleaving capacity is finite, as happens in practice, the performance analysis of coded systems becomes more difficult; consequently, most studies in the literature rely on computer simulation. Recently, however, several analytical advances have been made. For Rayleigh fading, Ho and Fung [19, 20] and Fung [21] derived an exact expression for the PEP of TC-MPSK or TC-MDPSK with a finite interleaving depth.

Some of the studies above, and many others reported in the literature, use Chernoff bounds which, in this case, only yield qualitative descriptions of bit error performance, and hence accurate results must be obtained by computer simulation. More accurate methods (e.g., [16, 19]) are limited to the Rayleigh fading channel.

1.2 Objectives

This study analyzes TCM performance in fading environments. Its objectives are to:

1. provide the analytical means for evaluation of coded error performance for Rician fading channels, thus alleviating the need for computer simulation;

2. enhance the insight into the basic parameters governing the performance. These include the code parameters, the interleaving capacity, and the fading bandwidth;

3. extend analytical results to more complex channel models and coding strategies. For instance, error bounds are derived for TCM over shadowed fading channels as well as concatenated coding systems and ARQ systems.

1.3 Contribution of This Thesis

In this work the following contributions have been made.

1. As mentioned above, the difficulty of obtaining tight upper bounds on P_b stems from the lack of an accurate expression for the PEP. To avoid this problem, this thesis presents a saddle point approximation method to compute the PEP of TCM schemes over Rician fading channels. The approximation is applicable under several conditions such as finite and ideal interleaving, ideal coherent and pilot-tone aided detection, pilot-symbol aided detection, and differential detection. When ideal interleaving is assumed, an asymptotic approximation for the PEP of TCM in conjunction with these detection methods is derived. This asymptotic approximation of the PEP is in a product form and is much tighter than the ordinary Chernoff bound. Also, based on the SAP, the effect of finite interleaving depth on the error performance of TCM schemes over Rician and shadowed Rician channels is studied. These results can be used for fast and accurate performance evaluation of coded systems as well as a search of optimum trellis codes for fading channels. In addition, they provide insight into the effect of channel measurement accuracy on the performance of the coded system.

2. The Canadian mobile satellite channel has been modelled as the sum of lognormal and Rayleigh components to represent foliage attenuation and multipath fading, respectively. In this thesis, new analytical expressions are

derived for the PEP of TCM schemes over this channel under ideal interleaving. The analysis is applied to the pilot-tone based detection strategy, and the results are substantiated by means of computer simulation. In addition, first order statistics of absolute and differential phases of a shadowed Rician process are derived. Our analysis establishes that, on a first order basis, the light and shadowed fading channels are Rician.

3. In fading channels, interleaving can significantly improve coded communication system performance. Although most theoretical results in the literature assume that the interleaving capacity is infinite, end-to-end delay caused by interleaving limits it in practice. This thesis presents new upper bounds on the PEP of TCM schemes over *nonindependent* Rician fading channels. The analysis is applied to the pilot-tone model. In addition, for Rayleigh fading channels with an exponential auto-covariance function, bounds resembling those for memoryless channels have been derived. The bounds are substantially more accurate than Chernoff bounds, and hence allow for an accurate estimation of system performance when the assumption of ideal interleaving is relaxed.

4. The performance of concatenated coding systems and ARQ systems operating on fading channels is addressed. New error expressions, which show the asymptotic error behaviour, are derived when the decoding is accomplished using a modified Viterbi algorithm. These expressions allow useful evaluation of the coding gain and throughput.

5. Finally, the performance of convolutional codes in fading channels is analyzed. An upper bound on the bit error probability, the optimum power split ratio between the data and pilot signals, and the channel cut-off rate are derived.

1.4 Thesis Outline

The subsequent chapters are developed as follows. In Chapter 2, the concept of TCM, the system and channel models, and the concept of interleaving are briefly described.

Using the saddle point approximation method, approximate expressions for the PEP of TCM transmitted over Rician fading are derived in Chapter 3. For ideally interleaved Rician channels, new performance bounds are developed.

In Chapter 4, the expressions developed in Chapter 3 are extended to study the performance of TCM in the shadowed Rician fading channel. To assess the tightness of the bounds, simulation results are presented.

The effects of finite interleaving capacity on the performance of TCM are examined in Chapter 5. Accurate error bounds are derived and then simplified for the Rayleigh channel.

In Chapter 6, for the Rayleigh fading environment, expressions for the throughput of ARQ systems and the bit error performance of concatenated coding systems are derived.

Convolutional code performance in Rayleigh fading channels is addressed in Chapter 7.

A summary of results and suggestions for future research are provided in Chapter 8.

Appendix A details the characteristic function of a Hermitian quadratic form of complex Gaussian variates. Appendix B describes a numerical method for contour integration. First-order statistics of the differential phase of a shadowed Rician process are derived in Appendix C. An upper bound on the positive eigenvalues of a weighted covariance matrix is derived in Appendix D. In Appendix E, an approximate determinant required in Chapter 6 is derived.

Chapter 2

Fundamentals

2.1 Introduction

The purpose of this chapter is to describe the concept of TCM, the system and channel models, and the block interleaver.

In Section 2.2, we describe the concept of TCM. Our description of TCM is necessarily brief, and the reader is referred to [22, 23] for excellent tutorial overviews of TCM. Since the provision of channel gain measurements is essential in realizing the potential benefits of using codes for fading channel communications, a pilot-tone based communication system model is presented in Section 2.3. The Rician channel model is introduced in Section 2.4. For fading channels, channel symbol interleaving plays an essential role in breaking up bursts of errors, which ensures the memoryless channel condition. This technique and its effect on the channel auto-covariance function are explained in Section 2.4.

2.2 TCM Concept

The main application of TCM is for bandlimited channels where the channels symbols must carry at least 2 information bits per symbol. Consequently, such channels need multilevel PSK or QAM. Since traditional convolutional codes, which are optimized for binary PSK, are ineffective when combined with multilevel signals, Ungerboeck [5] proposed TCM.

The general coding procedure outlined by Ungerboeck is as follows. To transmit n bits/symbol in one signal interval T_s, a signal set of size $M = 2^{n+1}$ is used, and m ($\leq n$) input bits are expanded in $m+1$ bits by a rate $m/(m+1)$ convolutional encoder. The signal mapper uses $n+1$ bits ($m+1$ coded bits and the remaining $n-m$ bits) to select one signal out of the selected M-level signal set. The TCM scheme in Figure 2.1 is an example of this procedure.

The minimum Euclidean distance between any two codewords $\mathbf{x}$ and $\hat{\mathbf{x}}$ is called the free Euclidean distance:

$$d^2_{free} = \underset{\mathbf{x} \neq \hat{\mathbf{x}}}{\text{Min}} \sum_{k=1}^{N} |x_k - \hat{x}_k|^2 \ \forall N, \tag{2.1}$$

where N is the length of the codewords. In AWGN channels, optimal performance is achieved if codes are designed to maximize the free distance.

The mapping of output codewords to the signal set is crucial for maximizing d^2_{free}. To facilitate this, Ungerboeck introduced the important concept of *set partitioning*. With set partitioning, a signal set is partitioned into subsets where each partition divides a previous set into two subsets having the same number of elements. This division continues until only one point remains in each subset.

Partitioning is usually done such that the minimum squared Euclidean distance between all non-equal points in each subset is as large as possible. The minimum of these distances over all the subsets is called the *Minimum Squared Subset Distance(MSSD)* at partition level p, and is denoted Δ_p. Partition levels start at 0 for the full signal set and increment by one for each two-level partition. Due to symmetry in the signal set, Δ_p is usually the same in each subset. Generally, set partitioning results in subsets with increasing minimum distances $\Delta_0 < \Delta_1 < \Delta_2, \cdots$ between the signals of these subsets. Figure 2.2 provides an example [5] of such set partitioning for 8-PSK signal set.

Ungerboeck [5] gives three heuristic rules for mapping by set partitioning, the conformity to which guarantees the maximum d^2_{free}. They are: use all signals with

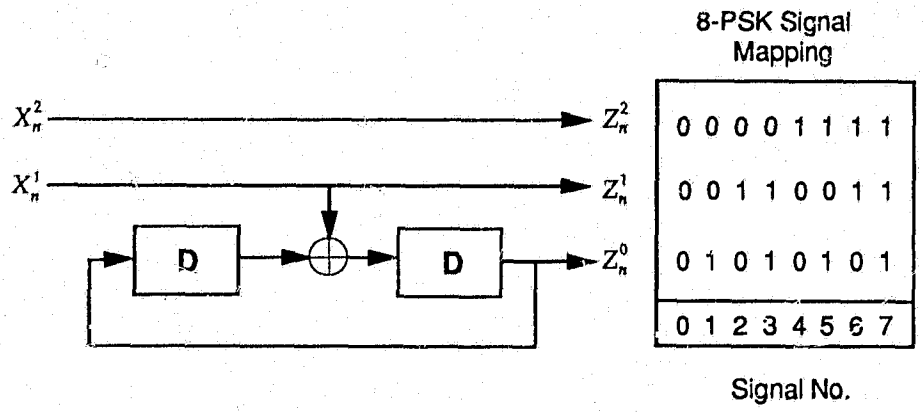

(a) 4-State convolutional encoder

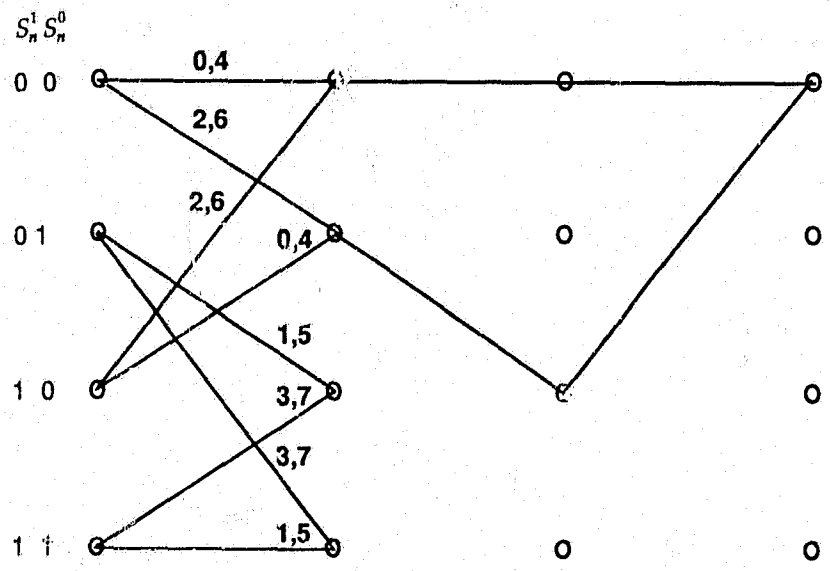

(b) Four-state Trellis

Figure 2.1: Realization of 8-PSK TCM with a 4-state Encoder.

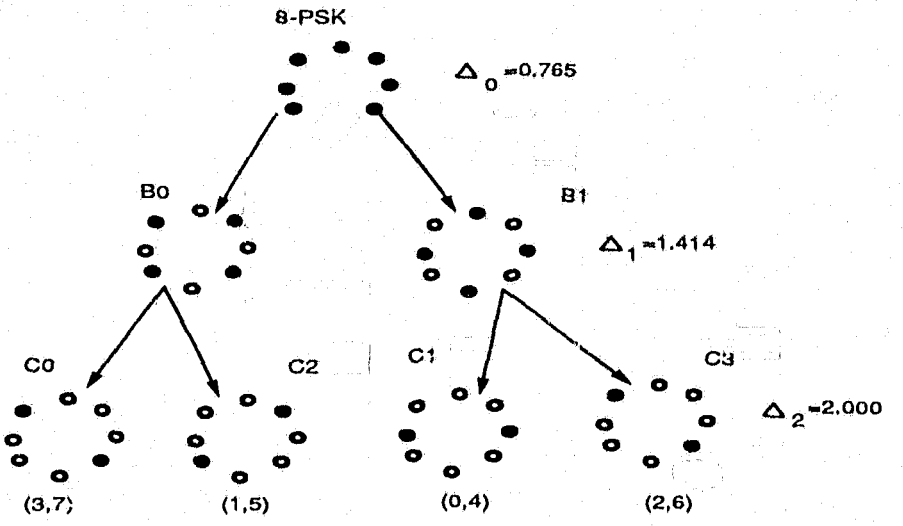

Figure 2.2: Set Partitioning for 8-PSK Constellation.

equal frequency and with a fair amount of regularity and symmetry, maximize the distance between parallel transitions, and maximize the distance between transitions originating or ending in the same state next. This TCM scheme of Figure 2.1 is given in Ungerboeck's key paper [5]. It is seen that the trellis branches are labeled in accordance the three rules above.

Maximization of d^2_{free} is effective only for AWGN channels. For MF channels, the design criterion is completely different. The problem of TCM design for MF channels has been considered in [24-28].

The energy savings that arise with the use of coding are quantified by coding gain. For AWGN channels, coding gain is defined as

$$G \triangleq 10 \log_{10} \left[\frac{d^2_{free,c}}{d^2_{free,u}} \right] \tag{2.2}$$

where $d^2_{free,c}$ and $d^2_{free,u}$ are the free Euclidean distances for coded and uncoded systems, respectively, and both coded and uncoded systems have the same average power and noise variance. Typical coding gains are in the range 3 to 6 dB for AWGN channels.

The above coding gain definition is meaningless for MF channels, where coding can provide dramatic power savings. For instance, at high SNR the average bit error probability of a TCM scheme in MF channels varies as [6]

$$P_b \sim \left(\frac{1}{\overline{E}_s/N_0}\right)^L \tag{2.3}$$

where $\overline{E}_s/N_0$ is the average signal-to-noise ratio, and L is the minimum Hamming distance between any two valid codewords of the TCM scheme. Typically, for TCM schemes $L \geq 2$, whereas for uncoded systems, $L = 1$. This implies that significant power savings are possible in coded systems in comparison to uncoded systems.

2.3 System Description

The system under consideration, as described in [6, 12], is shown in Fig. 2.3. Binary input data is convolutionaly encoded at rate $n/(n+1)$ where n is the number of information bits per encoding interval. The encoded $n+1$ bit words are mapped into a sequence $\mathbf{x} = (x_1, x_2, \ldots, x_N)$ of M-ary PSK symbols and block interleaved (note that both the encoder and the mapping rule are specified by the TCM scheme). Following the interleaver, we assume that a pilot tone is added to the data signal in order to recover the faded carrier at the receiver. The composite signal is then pulse shaped (to limit intersymbol interference) and transmitted. The receiver deinterleaves and then applies soft-decision Viterbi decoding.

A block interleaver of N_s (interleaving span) columns and N_d (interleaving depth) rows of memory is considered here. The encoder output is written into the memory column by column and read out row by row. The received symbols are reordered in the reverse manner. Interleaving is further described in Section 2.5.

We note that this is a generic channel estimation model, as typified by the pilot-tone concept [29]. As will be seen later, this model encompasses ideal coherent detection, differential detection, pilot-tone and pilot-symbol aided detection.

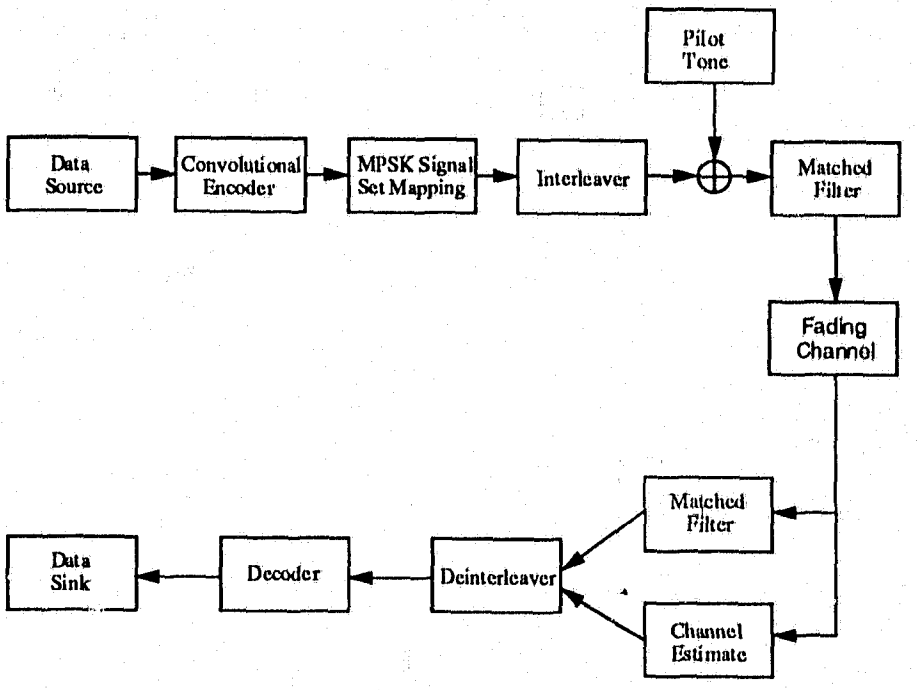

Figure 2.3: System Model.

2.4 Channel Model

The representation of PSK symbols is $x_k \in \{\exp(j2\pi i/M) : i = 0, 1, \ldots, M-1\}$ for all symbols, where $j^2 = -1$.

The transmitted signal is represented in the baseband as [16]

$$e(t) = B \sum_{k=-\infty}^{\infty} v_k s(t - kT_s) \tag{2.4}$$

where T_s is the symbol duration, B is an amplitude factor, and $s(t)$ is a Nyquist pulse (a pulse which result in zero inter-symbol interference) with unit energy:

$$\int_{-\infty}^{\infty} |s(t)|^2 \, dt = 1. \tag{2.5}$$

In (2.4) v_k is the k-th transmitted signal, defined in order to account for the differential encoder that might be placed after the interleaver, which relates to x_k

(the k-th output of the encoder) in the following manner:

$$v_k = \begin{cases} x_k & \text{TC-MPSK,} \\ v_{k-1}x_k & \text{TC-MDPSK.} \end{cases} \tag{2.6}$$

Although interleaving implies that the order of the transmitted sequence will be a scrambled version of the order of the encoder output sequence, to simplify notation, this rearrangement is not explicitly shown in (2.4). Instead, the effect of interleaving is accounted for by modifying the channel auto-covariance function (see Section 2.5).

The random process observed at the output of the fading channel is

$$y(t) = \alpha(t)e(t) + n(t) \tag{2.7}$$

where $\alpha(t)$ is a stationary, complex Gaussian random process representing the multiplicative fading (frequency nonselective Rician), and $n(t)$ is the additive white Gaussian noise (AWGN) process whose two-sided power spectral density is N_0. We assume that $\alpha(t)$ varies slowly in comparison to the data rate $1/T_s$; that is, we assume $\alpha(t)$ remains constant over each symbol period, and let α_k denote its value for the k-th interval. The signal is demodulated using a filter matched to $s(t)$. Hence, the above assumption implies that the received sample corresponding to the k-th coded symbol can be denoted by

$$y_k = \alpha_k v_k + n_k, \tag{2.8}$$

which is normalized by dividing by B. For notational brevity, we normalize the amplitude of the fading process; that is,

$$\langle |\alpha_k|^2 \rangle = 1 \tag{2.9}$$

where $\langle \bullet \rangle$ denotes a statistical average. In (2.8) n_k is a complex-Gaussian random variable with zero mean and variance σ^2. It can be readily shown that $\sigma^2 = (2\gamma_s)^{-1}$

where $\gamma_s = \overline{E}_s/N_0$. Here $\overline{E}_s/N_0$ denotes the average signal energy-to-noise spectral density ratio.

The channel gain α_k is modelled as a complex-Gaussian random variable having the following statistical parameters:

$$\langle \alpha_k \rangle = A, \;\; \frac{1}{2}\langle (\alpha_k - A)(\alpha_k - A)^* \rangle = b_0 \tag{2.10}$$

where the constant mean A denotes the line-of-sight (LOS) and specular components of the received signal, and b_0 is the variance of the diffuse component (Rayleigh fading) of the received signal. Note that (2.9) implies that $A^2 + 2b_0 = 1$. The ratio $K = A^2/2b_0$ is known as the Rician factor. For Rayleigh fading, $A = 0$ and $b_0 = 0.5$.

Clearly, the α_k's form a piece-wise constant approximation to the continuous random process $\alpha(t)$, and this approximation converts, in effect, the continuous random process into one with a discrete time parameter. Assuming, temporarily, that no interleaving is employed, two possible models for the covariance between α_{k_1} and α_{k_2} in this discrete channel are

$$\rho(k_1 - k_2) = \begin{cases} J_0(2\pi f_D T_s |k_1 - k_2|) \\ \exp(-2\pi f_D T_s |k_1 - k_2|), \;\; k_1, k_2 \in \{0, 1, 2, \ldots\} \end{cases} \tag{2.11}$$

where f_D is the Doppler spread of the fading process and $J_0(\cdot)$ is the zero-order Bessel function. In the above, the Bessel auto-covariance corresponds to the land mobile spectrum, while the exponential corresponds to the first order Butterworth spectrum. Other possible correlation models are given in [6]. It should also be mentioned that the exponential model usually results in correlation matrices that are easier to manipulate algebraically.

Note that for a memoryless channel, Eq. (2.11) would be

$$\rho(k_1 - k_2) = \begin{cases} 1 & k_1 = k_2 \\ 0 & k_1 \neq k_2 \end{cases} . \tag{2.12}$$

v_1	v_{11}	v_{21}	v_{31}	v_{41}
v_2	v_{12}	v_{22}	v_{32}	v_{42}
v_3	v_{13}	v_{23}	v_{33}	v_{43}
v_4	v_{14}	v_{24}	v_{34}	v_{44}
v_5	v_{15}	v_{25}	v_{35}	v_{45}
v_6	v_{16}	v_{26}	v_{36}	v_{46}
v_7	v_{17}	v_{27}	v_{37}	v_{47}
v_8	v_{18}	v_{28}	v_{38}	v_{48}
v_9	v_{19}	v_{29}	v_{39}	v_{49}
v_{10}	v_{20}	v_{30}	v_{40}	v_{50}

Figure 2.4: Operation of a Block Interleaver ($N_d = 5$, $N_s = 10$).

Clearly, to achieve this condition, f_D must be very large compared to $1/T_s$, which is not true in practice. In fact, in most practical situations $f_D T_s \ll 1$. A method to increase the apparent Doppler spread at the receiver is interleaving, which is described next.

2.5 Interleaving

Coding gain of TCM, like most of other codes, is realized only when the channel errors are independent, as is the case with memoryless channels. However, since amplitude fades caused by MF produce bursts of errors, the mobile communication channel is not memoryless. Channel symbol interleaving can be used to alleviate this problem. That is, by scrambling the order of symbols at the transmitter and unscrambling it at the receiver, the channel memory can be reduced or effectively eliminated.

For simplicity, we use only the block interleaver, althougth other types of interleavers are available, including convolutional and pseudo random interleavers [30].

The operation of an interleaver is illustrated in Figure 2.4. The encoder output symobls are numbered consequtively 1 through 50. The order of transmission out of the interleaver is $v_1, v_{11}, v_{21}, v_{31}, v_{41}, v_2, \ldots$. At the receiver, following deinterleaving, the decoder procesess the receive symbols in the correct order: $v_1, v_2, v_3, \ldots$. As a result of this operation, the channel gains corresponding to any two consequtive v_k's are spaced by $N_d T_s$, compared to T_s in the case of no interleaving.

Accordingly, the time separation between, say, α_{k_1} and α_{k_2} in (2.8) is $N_d T_s|k_1 - k_2|$ instead of $T_s|k_1 - k_2|$ (for no interleaving). Therefore, Eq. (2.11) can be modified to model the normalized auto-covariance function of an interleaved channel:

$$\rho(k_1 - k_2) = \begin{cases} J_0(2\pi f_D N_d T_s|k_1 - k_2|) \\ \exp(-2\pi f_D N_d T_s|k_1 - k_2|) \triangleq q^{|k_1 - k_2|}, \quad k_1, k_2 \in \{0, 1, 2, \ldots\} \end{cases} \tag{2.13}$$

Alternatively, (2.13) can be interpreted as indicating that the effective Doppler rate seen at the decoder is $N_d f_D$[1].

Since Eq. (2.13) does not hold in all cases, its validity must be qualified as follows. Consider a set of N channel gains in (2.8) $\alpha_1, \ldots, \alpha_N$ corresponding to a transmitted codeword of the same length. The above time-separation relation holds only if all components of the transmitted codeword had been confined to a single column of the transmitter buffer. Fortunately, for most dominant error events, $N \ll N_s$, and hence we assume that this condition is true. This phenomenon has been described in detail in [19] for the block interleaver.

One might define the normalized effective Doppler rate as $N_d f_D T_s$, which adequately describes the interleaved fading channel. As $N_d f_D T_s \to \infty$, Eq. (2.13) approaches Eq. (2.12). In the literature, this situation is referred to by several synonymous terms: independent fading, full interleaving, ideal interleaving, and infinite interleaving capacity. The following terms describe the instances where

[1] As noted previously (see page 14), since the effect of interleaving is accounted for by replacing f_D by $N_d f_D$, the scrambling of the order of the channel encoder output sequence because of interleaving will not be shown in Eq. (2.4).

$N_d f_D T_s$ is finite: partial interleaving, non-ideal interleaving, nonindependent fading, and finite interleaving capacity.

2.6 Summary

In this chapter we have described fundamentals that will be used later in this thesis. In Section 2.2, we introduced the concept of TCM, gave an example scheme, and defined coding gain for AWGN and MF channels. The system model to be used in Chapters 3-6 was provided in Section 2.3. The Rician channel model and the received random process were presented in Section 2.4, and the models of channel auto-covariance function were given. The technique of interleaving and its effect on the apparent Doppler shift at the receiver were explained in Section 2.5.

Chapter 3

Performance of TCM in Rician Fading Channels

3.1 Introduction

In this chapter, we evaluate the performance of the coded system described in Sections 2.3 and 2.4 when the signals are transmitted over frequency-nonselective, slowly fading channels. As mentioned in Chapter 1, to mitigate the effects of fading, TCM schemes have been proposed for such fading channels (e.g. mobile satellite and cellular mobile systems). Typically, the analytical performance evaluation of such systems has been limited to upperbounds and ideal interleaving. Due to their looseness, upper bounds based on the Chernoff bound only yield qualitative descriptions of error performance. Accurate results must be obtained by computer simulation.

In order to obtain improved analytical estimates, Cavers and Ho [16] have proposed a method to compute the exact PEP of trellis coded multilevel phase shift keying (TC-MPSK) and multilevel differential phase shift keying (TC-MDPSK) over ideally interleaved Rayleigh fading channels. Ho and Fung [19] have extended the results of [16] to non-ideally interleaved Rayleigh fading channels. The residue method proposed in [16, 19] does not apply in the case of Rician fading channels. To remedy this situation, Huang and Campbell [31] have derived a SAP for the

exact PEP of TC-MDPSK over ideally interleaved Rician and shadowed Rician fading channels.

In this chapter, we derive a general approximation for the PEP of TCM schemes transmitted over Rician type fading channels, including both ideal and non-ideal interleaving. Our approximation is based on the saddle point method [32, 33, 34], and its accuracy is confirmed by comparing it to the results of numerical integration. We then apply the approximate PEP to evaluate the performance of TC-MPSK and TC-MDPSK schemes. Both schemes are studied for Rician channels [12] and the effects of non-ideal interleaving are taken into account. TC-MDPSK over shadowed Rician channels [35] is also studied, taking into consideration the effects of non-ideal and ideal interleaving. When ideal interleaving is employed to combat the fading (the interleaving depth sufficiently large for this requirement will be given later in this chapter), an asymptotic approximation to the PEP of TC-MPSK (ideal or pilot-tone based) and TC-MDPSK over Rician fading channels is derived. It directly leads to a union upper bound on the bit error probability via the transfer function bounding technique. Also, it resembles the well-known Chernoff bound [12] for the PEP and differs only by a multiplying factor that improves the approximation.

The chapter is organized as follows. Section 3.2 presents the system model used here and the characterisation of shadowed Rician fading models. In Section 3.3, a general approximation for the PEP of TCM schemes transmitted over Rician fading is derived and then specialized for several cases. Several examples are presented in Section 3.4. Finally, conclusions are provided in Section 3.5.

3.2 System Model

The system and the Rician channel model used here have been described in Sections 2.3 and 2.4. Hence, we describe only the shadowed Rician model. For shadowed Rician fading, A, the mean of the channel gain, is a lognormally distributed random

parameter	Light	Average	Heavy
b_0	0.158	0.126	0.0631
μ_0	0.115	-0.115	-3.91
$\sqrt{d_0}$	0.115	0.161	0.806

Table 3.1: Shadowed Rician Model.

variable having the probability density function

$$p(x) = \begin{cases} \frac{1}{\sqrt{2\pi d_0 x}} \exp\left(-\frac{(\log(x)-\mu_0)^2}{2d_0}\right), & x > 0 \\ 0, \quad \text{elsewhere} \end{cases} \tag{3.1}$$

Note that A is a constant for the Rician channel. The shadowing model parameters are from [35]. It should be noted that a more detailed treatment of this channel model will be presented in the next chapter, and hence our discussion of it will be very limited in this chapter.

In the following section the SAP for the PEP of a TCM scheme will be introduced.

3.3 Analysis

Consider a transmitted codeword $\mathbf{x} = (x_1, x_2, \ldots, x_N)$, and the corresponding received symbols $\mathbf{y} = (y_1, y_2, \ldots, y_N)$ where y_k for $(k = 1, 2, \ldots, N)$ is defined by Eq. (2.8). Recall the pilot-tone model given in Section 2.3. Let the pilot-tone estimates of the actual channel gains be denoted by $\hat{\boldsymbol{\alpha}} = (\hat{\alpha}_1, \hat{\alpha}_2, \ldots, \hat{\alpha}_N)$. A maximum likelihood estimate of $\mathbf{x}$ is obtained by selecting the codeword $\hat{\mathbf{x}} = (\hat{x}_1, \hat{x}_2, \ldots, \hat{x}_N)$ that maximizes the a-posteriori probability $P(\hat{\mathbf{x}}|\mathbf{y}, \hat{\boldsymbol{\alpha}})$. If all codewords are equally likely, this is equivalent to maximizing $P(\mathbf{y}|\hat{\mathbf{x}}, \hat{\boldsymbol{\alpha}})$. If the channel is memoryless, we have

$$P(\mathbf{y}|\hat{\mathbf{x}}, \hat{\boldsymbol{\alpha}}) = \prod_{k=1}^{N} p(y_k|\hat{x}_k, \hat{\alpha}_k). \tag{3.2}$$

It is often convenient to maximize the logarithm of this:

$$M_{\hat{\mathbf{x}}} = \log P(\mathbf{y}|\hat{\mathbf{x}}, \hat{\boldsymbol{\alpha}}) = \sum_{k=1}^{N} \log p(y_k|\hat{x}_k, \hat{\alpha}_k) \tag{3.3}$$

Thus the Viterbi decoder selects the $\hat{\mathbf{x}}$ that maximizes $M_{\hat{\mathbf{x}}}$.

To proceed further, we need a statistical description of $\hat{\boldsymbol{\alpha}}$. Recall that α_k is a Gaussian process. As will be seen later, the pilot-tone estimates are usually noisy versions of α_k. Hence, $\hat{\alpha}_k$ is also Gaussian with mean $\langle\hat{\alpha}_k\rangle = A$ and variance $b_1 = \frac{1}{2}\langle(\hat{\alpha}_k - \langle\hat{\alpha}_k\rangle)(\hat{\alpha}_k - \langle\hat{\alpha}_k\rangle)^*\rangle$. The normalized correlation coefficient between α_k and $\hat{\alpha}_k$ is $\mu = \frac{1}{2}\langle(\alpha_k - \langle\alpha_k\rangle)(\hat{\alpha}_k - \langle\hat{\alpha}_k\rangle)^*\rangle/\sqrt{b_0 b_1}$. Given that α_k and $\hat{\alpha}_k$ are jointly Gaussian, it can be readily proven that the conditional mean and variance [29, (11-1-15)] of α_k given $\hat{\alpha}_k$ are

$$\begin{aligned} Var(\alpha_k)|_{\hat{\alpha}_k} &= b_0(1 - |\mu|^2) \\ \langle\alpha_k\rangle|_{\hat{\alpha}_k} &= A + \mu\sqrt{\frac{b_0}{b_1}}(\hat{\alpha}_k - A). \end{aligned} \tag{3.4}$$

These can be readily used with Eq. (2.8), to obtain $p(y_k|x_k, \hat{\alpha}_k)$, which when substituted in (3.3) yields

$$M_{\hat{\mathbf{x}}} = \log P(\mathbf{y}|\hat{\mathbf{x}}, \hat{\boldsymbol{\alpha}}) = -\sum_{k=1}^{N} |y_k - \beta\hat{\alpha}_k\hat{x}_k|^2 \tag{3.5}$$

where $\beta = \mu\sqrt{b_0/b_1}$. Also, in deriving this, the term $A - A\beta$ in (3.5) has been neglected, since $\beta \approx 1$ for most cases of practical interest.

Depending on the detection technique used, the estimate $\hat{\alpha}_k$ is obtained as follows:

$$\hat{\alpha}_k = \begin{cases} \alpha_k & \text{TC-MPSK,} \\ y_{k-1} & \text{TC-MDPSK,} \\ \alpha_k + \zeta_k & \text{TC-MPSK with a pilot} \end{cases} \tag{3.6}$$

where ζ_k is the additve noise term, appearing because of the non-zero bandwidth of the pilot tone extraction filter. This will be considered later. We remark that decoding with the first estimate is optimal (i.e. in a maximum likelihood sense) but unachieveable while the last two are non-optimal but easily implementable.

The PEP $P(\mathbf{x} \rightarrow \hat{\mathbf{x}})$ is defined to be the probability of choosing the coded sequence $\hat{\mathbf{x}} = (\hat{x}_1, \hat{x}_2, \ldots, \hat{x}_N)$ when $\mathbf{x} = (x_1, x_2, \ldots, x_N)$ was transmitted. Since, of the two coded symbol sequences, only the components that differ contribute to the PEP, assign the set of subscripts k_i, $(i = 1, 2, \cdots, L)$, arranged in ascending order, for which $x_{k_i} \neq \hat{x}_{k_i}$. Note that L is the Hamming distance between $\mathbf{x}$ and $\hat{\mathbf{x}}$. The smallest possible L, L_{min}, is known as the code *diversity*. The PEP, by using the fact that the total metric for a codeword is the sum of component metrics, is

$$P(\mathbf{x} \rightarrow \hat{\mathbf{x}}) = \Pr\{\Xi < 0\} \tag{3.7}$$

where

$$\Xi = \sum_{i=1}^{L} y_{k_i} \beta^* \hat{\alpha}_{k_i}^* (x_{k_i} - \hat{x}_{k_i})^* + y_{k_i}^* \beta \hat{\alpha}_{k_i} (x_{k_i} - \hat{x}_{k_i}) \tag{3.8}$$

Let V_i denote the 2×1 column matrix

$$V_i = (\hat{\alpha}_{k_i} \;\; y_{k_i})^T. \tag{3.9}$$

Thus the decision variable Ξ can be compactly represented as

$$\Xi = \sum_{i=1}^{L} V_i^\dagger F_i V_i = \mathbf{V}^\dagger \mathbf{F} \mathbf{V} \tag{3.10}$$

where the dagger denotes conjugate transpose, and $\mathbf{V}$, $\mathbf{F}$ are given by

$$\mathbf{V} = \begin{pmatrix} V_1 \\ \vdots \\ V_L \end{pmatrix}, \quad \mathbf{F} = \begin{pmatrix} F_1 & \cdots & 0 \\ \vdots & \ddots & \vdots \\ 0 & \cdots & F_L \end{pmatrix} \tag{3.11}$$

with

$$F_i = \begin{pmatrix} 0 & \beta^*(x_{k_i} - \hat{x}_{k_i})^* \\ \beta(x_{k_i} - \hat{x}_{k_i}) & 0 \end{pmatrix}. \tag{3.12}$$

From (2.8), (2.10) and (7.22), it follows that each V_i is Gaussian with the 2×2 covariance matrix

$$R_i = \begin{pmatrix} b_1 & \mu\sqrt{b_0 b_1}x_{k_i} \\ \mu^*\sqrt{b_0 b_1}x_{k_i}^* & b_0 + \sigma^2 \end{pmatrix}. \tag{3.13}$$

For the two cross correlation terms in this, x_{k_i} appears instead of v_{k_i}, as necessitated by (2.8), because for TC-MDPSK the term $\alpha_{k_i} v_{k_i - 1}$ is considered the true channel gain. We also need the covariance matrix $\mathbf{R}$ of the random vector $\mathbf{V}$. $\mathbf{R}$ is defined as the $2L \times 2L$ matrix

$$\mathbf{R} = \frac{1}{2}\langle [\mathbf{V} - \langle \mathbf{V} \rangle]^* [\mathbf{V} - \langle \mathbf{V} \rangle]^T \rangle. \tag{3.14}$$

Next we obtain a SAP to the PEP given by Eq. (3.7).

3.3.1 The SAP

From Eq. (3.7), the PEP is

$$P(\mathbf{x} \to \hat{\mathbf{x}}) = \Pr(\Xi < 0) = \int_{-\infty}^{0} p_\Xi(\Xi) d\Xi. \tag{3.15}$$

In terms of the characteristic function $G_\Xi(\nu)$ of Ξ, the above can be expressed as [36, Eq.(4B.4)]

$$P(\mathbf{x} \to \hat{\mathbf{x}}) = \frac{-1}{2\pi j} \int_{-\infty + j\epsilon}^{\infty + j\epsilon} \frac{G_\Xi(\nu)}{\nu} d\nu, \tag{3.16}$$

where $\epsilon > 0$, to avoid the singularity at the origin. The characteristic function of Ξ is given by [29, App. B]

$$G_\Xi(\nu) = \frac{\exp\left(j\nu \langle \mathbf{V} \rangle^\dagger (\mathbf{F}^{-1} - 2j\nu \mathbf{R}^*)^{-1} \langle \mathbf{V} \rangle\right)}{\det(\mathbf{I} - 2j\nu \mathbf{R}^* \mathbf{F})} \tag{3.17}$$

where **V**, **R**, **F** are defined above. Except for the case of Rayleigh fading, the above integral appears to defy an analytical solution. It is, however, not difficult to compute the above integral numerically as the absolute value of the integrand can be made to decrease to zero quickly as $|\nu| \to \infty$ by choosing a suitable ϵ. Neverthless, it is desirable to avoid the numerical integration of Eq. (3.16) and find an efficient and accurate alternative. Therefore, we turn to the SAP method for this type of contour integral [32-34].

By substituting $s = j\nu$, Eq. (3.16) can be converted to an equivalent contour integral

$$P(\mathbf{x} \to \hat{\mathbf{x}}) = \int_{-\infty}^{0} p_{\Xi}(\Xi) d\Xi = \frac{1}{2\pi j} \int_{c-j\infty}^{c+j\infty} \exp\left(\phi(s)\right) ds, \quad c < 0, \tag{3.18}$$

where

$$\phi(s) = \log(M_{\Xi}(s)) - \log(-s). \tag{3.19}$$

Here $M_{\Xi}(s)$ is the moment generating function of the random variable Ξ. The basis of the SAP is as follows. The above contour of integration can be moved to the left (i.e., the choice of c) provided that it does not cross any singularities of $\phi(s)$, by virtue of the Cauchy theorem [37]. Thus, the choice of c is limited to the range $\text{Real}(p_-) < c < 0$ where p_- is the rightmost singularity of $\phi(s)$ in the left complex plane. If a $c = c_0$ can be found such that $\phi'(c_0) = 0$ and $\phi''(c_0) > 0$, then consider the vertical contour $s = c_0 + jy$, $-\infty < y < \infty$. Expanding the exponent $\phi(s)$ about the point $s = c_0$ in a Taylor series and negelecting higher order terms, we have

$$\phi(s) \approx \phi(c_0) - \frac{1}{2}\phi''(c_0) y^2. \tag{3.20}$$

Substituting (3.20) into (3.19) and integrating along the above contour results in the expression

$$P(\mathbf{x} \to \hat{\mathbf{x}}) \cong \frac{1}{\sqrt{2\pi\phi''(c_0)}} \exp\left(\phi(c_0)\right). \tag{3.21}$$

This is termed as a zero-order SAP [33], and c_0 is known as a saddle point of $\phi(s)$. Also, fortunately, it suffices to compute an approximate value of c_0.

For the validity of (3.21), the following three conditions must be satisfied:

1. Real$(p_-) < c < 0$;
2. c_0 is unique; and
3. $\phi''(c_0) > 0$.

In order to prove that these conditions are met, we utilize, instead of using the charateristic function given in Eq. (3.17), an equivalent form Eq. (A.1.7) (see Appendix A). As will be soon evident, the use of this equivalent form of the characteristic function immediately confers a range for c_0. Eq. (3.19) then becomes

$$\phi(s) = \sum_{i=1}^{2L} \frac{s\phi_i |\langle \eta_i \rangle|^2}{1 - 2s\phi_i} + \sum_{i=1}^{2L} \log \frac{1}{1 - 2s\phi_i} - \log(-s). \tag{3.22}$$

Differentiating with repect to s yields

$$\phi'(s) = \sum_{i=1}^{2L} \frac{\phi_i |\langle \eta_i \rangle|^2}{(1 - 2s\phi_i)^2} + \sum_{i=1}^{2L} \frac{2\phi_i}{1 - 2s\phi_i} - \frac{1}{s}. \tag{3.23}$$

Differentiating with respect to s once again yields

$$\phi''(s) = \sum_{i=1}^{2L} \frac{4\phi_i^2 |\langle \eta_i \rangle|^2}{(1 - 2s\phi_i)^3} + \sum_{i=1}^{2L} \frac{4\phi_i^2}{(1 - 2s\phi_i)^2} + \frac{1}{s^2}. \tag{3.24}$$

We mention that the ϕ_i's are the eigenvalues of $\mathbf{R}^*\mathbf{F}$, and the η_i's are related to the means of the random variables (Definitions of them can be found in Appendix A). From Eq. (3.23), it is seen that $\phi'(c_0) = 0$ has $4L$ solutions. If ϕ_{-1} denotes the smallest negative eigenvalue of $\mathbf{R}^*\mathbf{F}$ (i.e., the one farthest away from the origin), then the solution satisfying $1/(2\phi_{-1}) < c_0 < 0$ is the only one useful to us. Examining Eqs. (3.23), (3.24) shows that when s increases from $1/(2\phi_{-1})$ to 0, $\phi'(s)$

increases from $-\infty$ to ∞, and $\phi''(s) > 0$. Thus c_0 is unique and is expedetiously obtained via Newton's method. It is also apparent that this root automatically satifies the conditions mentioned above. For the case of Rayleigh fading, the above is somewhat simplified as $\langle \eta_i \rangle$=0.

It should be pointed out that our formulation differs from that of [31]. In [31], to find the PEP of a given error event, the error event is replaced by an equivalent error event that has the same Euclidean distance but equally weighted branches. This replacement introduces some imprecision into the estimate. Also, the method given in [31] is not suitable for the cases of non-ideal interleaving and Rayleigh fading, and is only applicable to differential detection.

In sum, the following steps are needed to calculate the approximate pairwise error probability of any error event: (i) obtain $\mathbf{R}$ and $\mathbf{F}$, (ii) diagonalize both simultaneously, (iii) compute the saddle point using Eqs. (3.23), (3.24), finally (iv) compute the approximation using Eq. (3.21).

3.3.2 Ideal Interleaving

For ideal interleaving/deinterleaving, the covariance matrix $\mathbf{R}$ (3.14) of $\mathbf{V}$ will be formed by placing R_i's diagonally, the other entries of $\mathbf{R}$ being zero. Thus,

$$\mathbf{R} = \begin{pmatrix} R_1 & \cdots & 0 \\ \vdots & & \vdots \\ 0 & \cdots & R_L \end{pmatrix}. \tag{3.25}$$

Now using this $\mathbf{R}$ the approximate PEP can be found. However, in order to obtain more insight into the error performance of TCM schemes, we next derive the asymptotic behaviour of this approximation. As mentioned before, it is expressed in a product form that is usable in the classical generating function method. Because of perfect interleaving/deinterleaving, the eigenvalues of $\mathbf{R}^*\mathbf{F}$ can be determined by considering each 2×2 matrix product $\mathbf{R}_i^*\mathbf{F}_i$. Let ϕ_{i-} and ϕ_{i+} denote

those two. From Eqs. (3.12), (3.13), it follows that

$$\begin{bmatrix} 1/2\phi_{i+} \\ 1/2\phi_{i-} \end{bmatrix} = \frac{-b_0 \pm \sqrt{b_0^2 + 4|x_{k_i} - \hat{x}_{k_i}|^{-2}|\mu|^{-2}b_0((1-|\mu|^2)b_0 + \sigma^2)}}{4b_0((1-|\mu|^2)b_0 + \sigma^2)}. \tag{3.26}$$

Clearly, when $\mu \approx 1$, and $\sigma^2 \to 0$, we have

$$\begin{bmatrix} 1/2\phi_{i+} \\ 1/2\phi_{i-} \end{bmatrix} \approx \begin{cases} 0 \\ -\frac{1}{2((1-|\mu|^2)b_0+\sigma^2)} \end{cases}. \tag{3.27}$$

In other words, at large $\overline{E}_s/N_0$ and with reasonably accurate estimates (i.e, $\mu \approx 1$) the $2L$ eigenvalues of $\mathbf{R}^*\mathbf{F}$ collect into two clusters, with L of them belonging to each. By substituting these in Eq. (3.23), it can be shown that the saddle point is given by

$$c_0 \approx -\frac{1}{4((1-|\mu|^2)b_0 + \sigma^2)}. \tag{3.28}$$

Substituting this c_0 in Eq. (3.21) and manipulating further, we get

$$P(\mathbf{x} \to \hat{\mathbf{x}}) \cong B(L) \prod_{i=1}^{L} \frac{\Gamma}{b_0|\mu|^2|x_{k_i} - \hat{x}_{k_i}|^2 + \Gamma} \exp \frac{A^2\theta|x_{k_i} - \hat{x}_{k_i}|^2}{b_0|\mu|^2|x_{k_i} - \hat{x}_{k_i}|^2 + \Gamma} \tag{3.29}$$

where

$$B(L) \cong \frac{1}{\sqrt{2\pi(2L+1)}}, \qquad \Gamma = 4((1-|\mu|^2)b_0 + \sigma^2), \tag{3.30}$$

and

$$\theta = \left[-\beta + \frac{2(b_0 + b_1 + \sigma^2)|\beta|^2 - 4\beta|\mu|^2 b_0}{\Gamma}\right]. \tag{3.31}$$

To obtain $B(L)$, the first term in Eq. (3.24), which can be shown to be negligible providing $\mu \approx 1$, has been neglected. In deriving θ, we have assumed, without much loss of generality, that β is real. This assumption is true for signals with symmetric spectra [38]. Also, when the quality of the channel estimates is sufficient (i.e. $\beta \approx 1, \mu \approx 1$), the value of θ is negative (≈ -0.5).

3.3.3 Ideal TC-MPSK

Here we have $\hat{\alpha}_k = \alpha_k$. Thus $b_1 = b_0$, $\mu = 1$, and $\beta = 1$. Substituting these values in (3.29) leads to the expression

$$P(\mathbf{x} \to \hat{\mathbf{x}}) \cong B(L) \prod_{i=1}^{L} \frac{1}{\frac{b_0}{2}|x_{k_i} - \hat{x}_{k_i}|^2 \gamma_s + 1} \exp \frac{-\frac{A^2}{4}|x_{k_i} - \hat{x}_{k_i}|^2 \gamma_s}{\frac{b_0}{2}|x_{k_i} - \hat{x}_{k_i}|^2 \gamma_s + 1} \tag{3.32}$$

which is identical to the Chernoff upper bound (e.g [6, (9.17)]) except the multiplier $B(L)$. For Rayleigh fading with $L = 2$, the above requires 3.7 dB less than the Chernoff bound. As shown in [16], the difference between the exact and the Chernoff bound is 3.6 dB. This fact suggests that the above approximation is quite accurate. For Rician fading channels, the accuracy of (3.32) decreases with increasing K.

3.3.4 TC-MDPSK

In this case, for any signalling period, the preceding signal provides the channel estimate (3.6). Hence, $b_1 = b_0 + \sigma^2$ and, assuming a land mobile channel [16], it follows that

$$|\mu|^2 = \frac{b_0 J_0^2(2\pi f_D T_s)}{b_0 + 0.5\gamma_s^{-1}} = \frac{b_0 \delta}{b_0 + 0.5\gamma_s^{-1}} \tag{3.33}$$

where $f_D T_s$ is the maximum normalized Doppler spread. The closer μ to unity, the more pronounced the benefits of using a code and better the approximation (3.29). Hence, we see that two factors degrade the quality of the estimates, one being the Doppler spread and the other being the additive noise (appearing as $(\overline{E}_s/N_0)^{-1}$). Unlike pilot aided detection, the channel estimate, being the time delayed data signal, has the same bandwidth as the data signal. Thus even for slow fading the additive noise degrades the quality of the estimates. In contrast, for pilot tone aided detection systems, as will be seen next, the pilot bandwidth approaches zero for slow fading ($f_D T_s \approx 0$), thus providing an essentially noise free estimate.

Substituting $|\mu|^2$ in (3.29) results in the expression

$$P(\mathbf{x} \to \hat{\mathbf{x}}) \cong B(L) \prod_{i=1}^{L} \frac{b_0(1-\delta)\gamma_s + 1 + (4b_0\gamma_s)^{-1}}{\frac{b_0}{4}\delta|x_{k_i} - \hat{x}_{k_i}|^2\gamma_s + b_0(1-\delta)\gamma_s + 1 + (4b_0\gamma_s)^{-1}} \tag{3.34}$$

$$\times \exp\left\{ \frac{\frac{A^2}{4}\theta\gamma_s|x_{k_i} - \hat{x}_{k_i}|^2(1 + 0.5(b_0\gamma_s)^{-1})}{\frac{b_0}{4}\delta|x_{k_i} - \hat{x}_{k_i}|^2\gamma_s + b_0(1-\delta)\gamma_s + 1 + (4b_0\gamma_s)^{-1}} \right\}.$$

Once again, for Rayleigh fading ($b_0 = 0.5, A = 0$) this reduces to the Chernoff bound (e.g. [6, 9.119]) except the multiplier $B(L)$. For ideal differential detection (i.e., very slow fading) $f_D T_s \to 0$, $J_0(2\pi f_D T_s) \approx 1 - (\pi f_D T_s)^2$, hence the approximate PEP varies as $(\pi f_D T_s)^{2L}$. This implies that the usual diversity effect of coding is applicable to the suppression of error floors as well [16]. Note also that, unless $f_D T_s = 0$, the approximate PEP does not approach 0 as $\overline{E}_s/N_0 \to \infty$. This fact suggests the existence of error floors.

The accuracy of (3.34) will decrease with two increasing factors: the Doppler spread and K. From (3.33), it is seen that for a given signal-to-noise ratio increased K lowers the value of b_0, thereby decreasing $|\mu|^2$ as well.

3.3.5 TC-PT-MPSK

The acronym TC-PT-MPSK denotes a system using a pilot tone as a phase reference. In practice, contrary to the convenient assumption of ideal coherent detection, the α_k's need to be measured using some technique such as a pilot tone [16] or embedded pilot symbols [39]. Cavers and Ho [16] have analyzed the performance of TC-PT-MPSK transmitted over Rayleigh fading channels. Here we obtain the error performance of this technique over Rician fading channels. To evaluate the pairwise error as given by (3.29), we simply need to compute the variance of $\hat{\alpha}_{k_i}$ and the covariance between $\hat{\alpha}_{k_i}$ and α_{k_i} for all k_i's. This can be accomplished by specifying the pilot-tone filter bandwidth and the fraction of power spent on the pilot-tone. As in [16], the estimate $\hat{\alpha}_k$ is obtained by a pilot tone extraction filter

whose frequency response is

$$H(f) = \begin{cases} \frac{1}{P} & -B_p/2 \leq f \leq B_p/2 \\ 0 & \text{otherwise} \end{cases} \tag{3.35}$$

where P is the amplitude of the pilot tone, and B_p is the bandwidth of the pilot tone filter. Now the fraction of the total power spent on the data signal and the pilot tone is $1/(1+r)$ and $r/(1+r)$, respectively, where $r = P^2 T_s$. As mentioned in [16], the bandwidth of the pilot-tone extraction filter should be sufficiently wide to allow for undistorted measurement of the fading process. Thus, $B_p = 2f_d$. Then, the output of this filter is

$$\hat{\alpha}_k = \alpha_k + \frac{\zeta_k}{P} \tag{3.36}$$

where ζ_k is a complex Gaussian random variable with zero mean and a variance of $B_p N_0$. It then follows that

$$var(\hat{\alpha}_k) = b_1 = b_0 + 0.5\,(B_p T_s)\left(\frac{1+r}{r}\right)\gamma_s^{-1}, \tag{3.37}$$

$$|\mu|^2 = \frac{b_0}{b_0 + 0.5\,(B_p T_s)\left(\frac{1+r}{r}\right)\gamma_s^{-1}}$$

where γ_s now accounts for the total symbol energy spent on both the data and pilot-tone. The point to note here is that when $\overline{E}_s/N_0 \rightarrow \infty$, $|\mu|^2$ approaches unity. Thus, at large signal-to-noise ratios, the pilot tone technique is essentially equivalent to ideal coherent detection. By substituting this in (3.29), we have

$$P(\mathbf{x} \rightarrow \hat{\mathbf{x}}) \cong B(L) \prod_{i=1}^{L} \frac{[\frac{B_p T_s(1+r)}{r} + 1 + r] + \frac{B_p T_s (1+r)^2}{2 b_0 r}\gamma_s^{-1}}{\frac{b_0}{2}|x_{k_i} - \hat{x}_{k_i}|^2 \gamma_s + [\frac{B_p T_s(1+r)}{r} + 1 + r] + \frac{B_p T_s (1+r)^2}{2 b_0 r}\gamma_s^{-1}} \tag{3.38}$$

$$\times \exp\left\{ \frac{\frac{A^2}{2} 0 \gamma_s |x_{k_i} - \hat{x}_{k_i}|^2 (1 + \frac{B_p T_s (1+r)^2}{2 b_0 r}\gamma_s^{-1})}{\frac{b_0}{2}|x_{k_i} - \hat{x}_{k_i}|^2 \gamma_s + [\frac{B_p T_s(1+r)}{r} + 1 + r] + \frac{B_p T_s (1+r)^2}{2 b_0 r}\gamma_s^{-1}} \right\}.$$

Note that, unlike the case of differential detection, there doesn't exist an irreducible error floor in this case. This, however, is due to our assumption of an ideal filter – realizable filters introduce a small error floor. Moreover, by neglecting the terms containing γ_s^{-1} in this and minimizing the term $[\frac{B_p T_s(1+r)}{r} + 1 + r]$ with respect to r, the optimum power split ratio becomes

$$r_{opt} = \sqrt{B_p T_s}. \tag{3.39}$$

This agrees well with the numerical values observed in [16]. As might be expected, the optimum choice of r is solely a function of the normalized, maximum Doppler. Also, by substituting r_{opt} in (3.38) and comparing it with (3.32), TCM schemes detected with a pilot tone require $10\log(1+\sqrt{B_p T_s})^2$dB more than TCM schemes with ideal coherent detection.

3.3.6 TC-PS-MPSK

The TC-PS-MPSK systems uses a set of periodically-inserted pilot symbol to derive a phase reference [10, 11, 16]. Let us consider here a frame of size N in which the first symbol is a pilot symbol and the remaining $N-1$ are data symbols. As derived in [16], the optimum interpolator at the receiver must be computed for each symbol position within the frame (i.e., changing interpolator coefficients at each symbol position). In order to simplify the analysis, we assume that the optimum interpolator is a fixed low-pass filter with bandwidth $2f_D$. If the data symbols and pilot symbols have the same amplitudes, the power split ratio r between the pilot and the data is $1/(N-1)$. Then the low-pass filter output can be approximated by Eq. (3.36) and the upper bound on the PEP is

$$P(\mathbf{x} \to \hat{\mathbf{x}}) \cong B(L) \prod_{i=1}^{L} \frac{[B_p T_s N + \frac{N}{N-1}] + \frac{B_p T_s N^2}{2b_0(N-1)}\gamma_s^{-1}}{\frac{b_0}{2}|x_{k_i} - \hat{x}_{k_i}|^2 \gamma_s + [B_p T_s N + \frac{N}{N-1}] + \frac{B_p T_s N^2}{2b_0(N-1)}\gamma_s^{-1}} \tag{3.40}$$

$$\times \exp\left\{ \frac{\frac{A^2}{2}\theta\gamma_s |x_{k_i} - \hat{x}_{k_i}|^2 (1 + \frac{B_p T_s N^2}{2b_0(N-1)}\gamma_s^{-1})}{\frac{b_0}{2}|x_{k_i} - \hat{x}_{k_i}|^2 \gamma_s + [B_p T_s N + \frac{N}{N-1}] + \frac{B_p T_s N^2}{2b_0(N-1)}\gamma_s^{-1}} \right\}.$$

Then the optimum frame length is given by

$$N = 1 + \frac{1}{\sqrt{2 f_D T_s}}. \tag{3.41}$$

This result is intuitively pleasing. The larger the Doppler spread, the smaller the frame size N; that is, more pilot symbols are required as the Doppler spread increases.

3.3.7 Non-ideal Interleaving

For a finite interleaving depth, covariance terms among different V_i's must be included in the covariance matrix $\mathbf{R}$ in Eq. (3.14). For this reason, we need to specify the covariance between α_{k_i} and α_{k_j}. As explained in Section 2.5, interleaving/deinterleaving has the same effect as transmitting at a longer symbol duration $N_d T_s$ [38] or, equivalently, as increasing the Doppler frequency by a factor of N_d [19]. Using Eq. (2.13), we can evaluate the covariance between V_l and V_m $(l, m = 1, \cdots, L)$ defined as

$$r_{l,m} = \frac{1}{2}\langle (V_l - \langle V_l \rangle)^* (V_m - \langle V_m \rangle)^T \rangle. \tag{3.42}$$

For TC-MPSK, by using the definition of V_i's (7.22) and utilizing Eq. (2.13), we have

$$r_{l,m} = b_0 J_0(\rho N_d(k_m - k_l)) \begin{pmatrix} 1 & x_{k_m} \\ x^*_{k_l} & x^*_{k_l} x_{k_m} \end{pmatrix}, \tag{3.43}$$

where $\rho = 2\pi f_d T_s$. Similarly for TC-MDPSK,

$$r_{l,m} = b_0 \begin{pmatrix} J_0(\rho N_d(k_m - k_l)) & J_0(\rho(N_d(k_m - k_l) + 1)) \\ J_0(\rho(N_d(k_m - k_l) - 1)) & J_0(\rho N_d(k_m - k_l)) \end{pmatrix}. \tag{3.44}$$

For the exponential correlation channel model, we can simply replace the Bessel function with the exponential Eq. (2.13). In the case of TC-MDPSK, we have assumed, with little loss of generality, the transmitted sequence $\mathbf{x}$ to be the all-zero sequence.

3.3.8 Bit Error Probability

Typically, the average bit error probability of a communication system is one of the most important performance measures. A tight upper bound on it is obtained via the union bound, which is given by

$$P_b \leq \frac{1}{k_0} \sum_{\mathbf{x},\hat{\mathbf{x}}} a(\mathbf{x} \to \hat{\mathbf{x}}) P(\mathbf{x} \to \hat{\mathbf{x}}) \tag{3.45}$$

where $a(\mathbf{x} \to \hat{\mathbf{x}})$ is the number of bit errors associated with the error event, and k_0 is the number of input bits per encoding interval. Since all possible codeword pairs are included, this will have infinitely many terms. Based on (3.29), all the terms in it may be enumerated using a transfer function. However, the expression (3.29) is not a true upper bound on $P(\mathbf{x} \to \hat{\mathbf{x}})$ but is a close approximation. As a result, by using such approximations with the standard transfer function technique, the bit error probability of a TCM scheme with ideal interleaving/deinterleaving is closely approximated as

$$P_b \approx \frac{B(L_{min})}{k_0} \frac{\partial T(D_1, D_2, \cdots, I)}{\partial I}\bigg|_{I=1} \tag{3.46}$$

where the D_i's are the product terms in (3.29), excluding $B(L)$, with each D_i being associated with $|x_{k_i} - \hat{x}_{k_i}|^2$. Note that the number of distinct D_i's is finite and that $B(L_{min})$ is included because $B(L)$ is a decreasing function of L. The transfer function $T(D_1, D_2, \cdots, I)$ is determined by a signal flow graph having modified branch labels [40]. This approximation can be improved by incorporating more exact (3.21) instead of (3.29) for some error events, an improvement suggested by [41].

When (3.29) breaks down or when finite interleaving is considered, (3.21) must be used to compute the approximate PEP, which is not in a product form. As a result, the union bound must be truncated to include only the dominant error events. This is the approach taken in [16] to compute the bit error probability for uniform [40] TCM. The resulting approximation to the bit error probability is [16], by the truncation of (3.45),

$$P_b \approx \frac{1}{k_0} \sum_{L_{min}}^{N} a(\mathbf{x} \to \hat{\mathbf{x}}) P(\mathbf{x} \to \hat{\mathbf{x}}) \tag{3.47}$$

where L_{min} is the minimum length of the error events included in this sum and N denotes the maximum length. The choice of N should not be too large, which requires an excessive amount of computation, nor be too small, which does not include a sufficient number of dominant error events. $N = 4$ or 5 appears to be satisfactory for trellis codes with L_{min}=2 or 3. Also, it should be pointed out that this technique will not yield a true upper bound because of the truncation.

3.4 Examples

In this section, we analyze the error performance of the two TCM schemes: 4PSK trellis-code shown in Fig. (3.1) [40] and 8PSK TCM scheme shown in Fig. (4.2). We remark that the exact PEP shown for comparison purposes in some of the results is computed by numerical integration of Eq. (3.16) (see Appendix B).

TC-4DPSK

First of all, Fig. 3.2 demonstrates the accuracy of the SAP. It is clear that the SAP is extremely close to the exact value obtained by numerical integration. In Figs. 3.2, 3.3 the interleaving depth $N_d = 16$ appears to be sufficient while N_d=32 provides better performance than ideal interleaving. This anomaly, attributable to the oscillatory nature of the Bessel correlation function, has been observed in [19] too. In contrast, for an exponential type correlation function, Figs. 3.4, 3.5 indicate that increasing N_d always improves the bit error performance. Secondly, it is observed that an increased Rician factor K tends to reduce the interleaving loss due to insufficient N_d. This is due to the fact that for large K the Rician channel approaches the Gaussian channel. The union upper bound on the bit error probability obtained via (3.34) and (3.46) is off by 1, 2 dB for $K = 5$, 10 dB, respectively at large $\overline{E}_s/N_0$. For comparison purposes, the SAP given in [31] is also plotted in these figures. For $K = 10$ dB, [31, Eq. (26)] is virtually identical to the exact PEP and the SAP given in Eq. (3.21), as Fig. (3.3) and Fig. (3.5) show. For $K = 5$ dB, however, [31, Eq. (26)] overestimates the PEP somewhat, which may be due to the fact that the accuracy of [31, Eq. (26)] decreases with decreasing K [31].

TC-4PSK

Figs. 3.6, 3.7 and 3.8 show the error performance of TC-4PSK with ideal channel measurements. They again illustrate the accuracy of the SAP, which is virtually identical to the exact obtained by numerical integration for the Rician channel. In Fig (3.6), for the Rayleigh fading channel the exact PEPs have been computed using the techniques given in [16, 19]. For ideally interleaved Rayleigh channels, the exact PEP and the SAP agree extremely well. From these figures, it is observed that the interleaving depth and the normalized Doppler spread product $N_d f_D T_s$ should be roughly about 0.3 so that the interleaver is as good as an ideal interleaver.

As a point of comparison, for convolutional coded binary PSK this product should be about 0.1 [38, 42]. Also shown is the upper bound on the bit error probability based on the Chernoff bound given in [40]. From Figs. 3.6, 3.7 and 3.8, the Chernoff bound is about 2 dB weaker than (3.32) for these cases.

TC-4DPSK in shadowing

In this case, the PEP is obtained by

$$P(\mathbf{x} \to \hat{\mathbf{x}}) = \int_0^\infty P(\mathbf{x} \to \hat{\mathbf{x}}|A)P(A)dA \tag{3.48}$$

To compute the conditional error probability, the SAP can be used, and the total integral evaluated using a numerical technique. The required interleaving depth appears to be on par with that of Rician channels. From Figs. (3.9) and (3.10), the error performance of this code over both light and average shadowing channels is close to that of a 5 dB Rician channel. This observation is consistent with [31].

TC-PT-4PSK

Fig. 3.11 shows the approximate bit error rate for the TC-4PSK scheme with pilot tone aided detection. We have considered three Doppler rates $f_D T_s$ of 0.01, 0.03, 0.06 and found that the corresponding optimum choice of the energy ratio r (see (3.39)) is 0.14, 0.25, 0.34. This agrees well with [16]. For comparison, also shown are the performance curves of TC-4PSK with ideal channel gain measurements and TC-4DPSK for corresponding Doppler rates. It is observed that for $f_D T_s = 0.01$ the performance of the pilot-tone technique is within 1 dB of unattainable ideal coherent detection and that it outperforms differential detection.

TC-8PSK

Fig. 3.12 depicts P_b for the eight state trellis-code in Rician fading ($K = 2,5$ dB). The upper bound is within 0.5 dB of the simulation points for $P_b \leq 10^{-3}$,

but becomes loose for $P_b > 10^{-3}$. This is a result of the asymptotic nature of the bound. It should be mentioned that a tight upper upper bound on P_b has been obtained in [41], but their method requires time consuming numerical integration.

TC-8DPSK

The bit error probability of the same code used in conjunction with differential detection is shown in Fig. 3.13. Again, the upper bound is quite tight for $P_b \leq 10^{-3}$. The performance degradation due to fast fading is less pronounced in this case than in Rayleigh fading because of the strong LOS component which has an attenuating effect on the phase jitter due to fast Doppler.

TC-PT-8PSK

Intuitively, one expects a pilot-tone based detection scheme to achieve better performance as $f_D T_s \rightarrow 0$, eventually reaching the performance level of ideal channel estimation. This can indeed be observed in Fig. (3.14), which shows P_b of the same trellis-code in Rician fading for $f_D T_s$ equal to 0.05, 0.01, and 0.001. For instance, at 5 % Doppler the performance of the pilot-tone system is 3 dB poorer than the ideal case (Fig. 3.12), and this loss diminishes with decreasing Doppler rates. For these Doppler rates, the power split ratio has been computed as indicated by (3.39). In Fig. 3.15, P_b is plotted as a function of the power split ratio r, which indicates that the choice of r is not critical, provided that it is close to r_{opt} [17].

3.5 Summary

This chapter derives a SAP for the PEP of TCM schemes transmitted over Rician channels. Comparison with the exact PEP computed by numerical quadrature integration indicates that the SAP is sufficiently precise (an error between 3 and 10 percent). Incidentally, by incorporating higher order terms [33] in the saddle point method, this error can be further reduced below 1 percent. It is felt, however,

that the zero-order approximation will suffice for our applications. This technique may also be useful for other cases such as trellis-coded QAM schemes [16], where one needs the probability that the decision variable is less than a certain threshold (not necessarily zero). For ideal interleaving, an asymptotic approximation of the PEP is derived, which is in a product form. For non-ideally interleaved Rician type channels, the performance degradation due to the finite interleaving capacity can be estimated with the help of the SAP approximation. This appears to be an extension of the work reported in [19] for the Rician model. The sufficient interleaving depth is found to be given by $N_d f_D T_s \approx 0.3$.

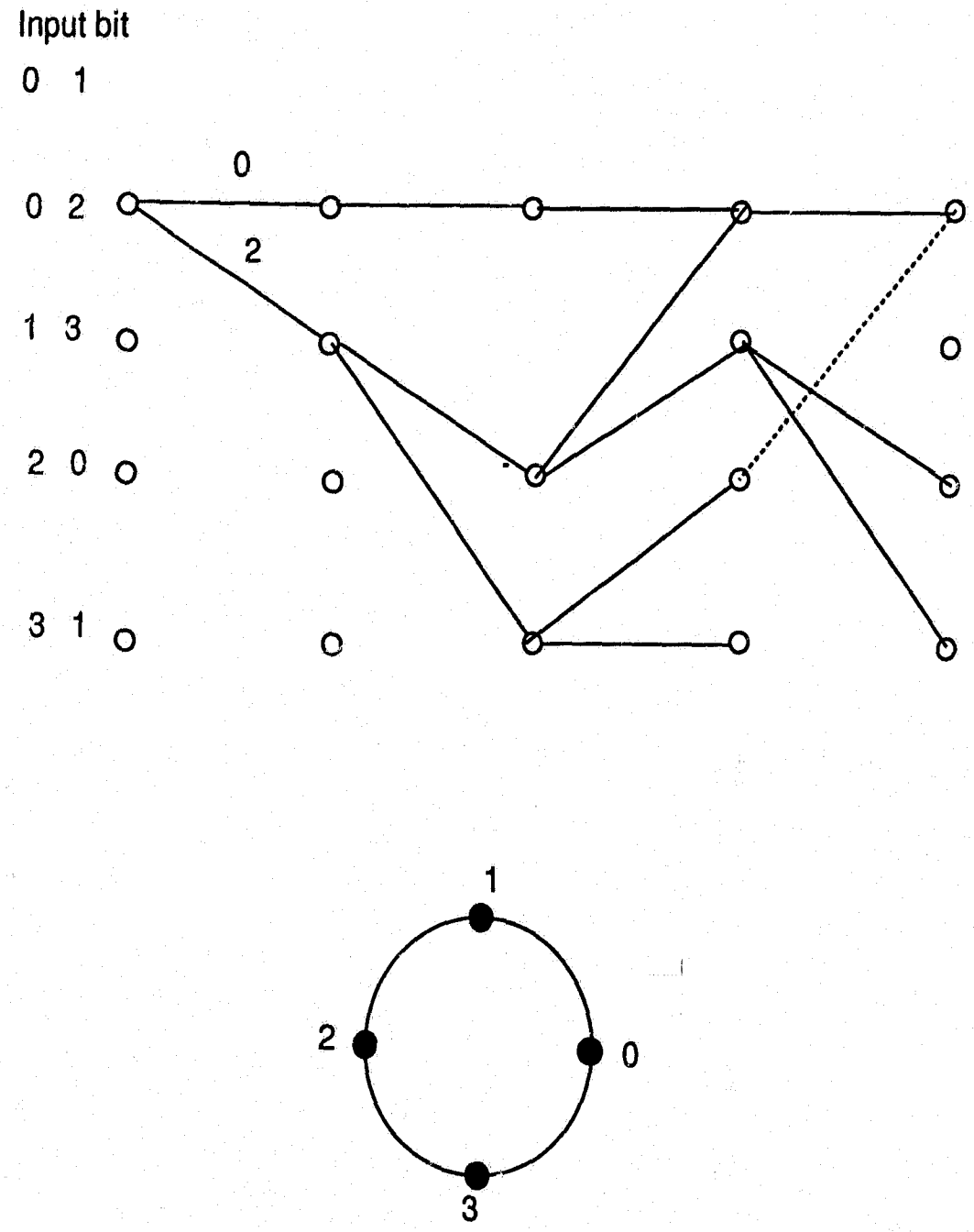

Figure 3.1: Trellis diagram for 4-state, 4PSK TCM Scheme.

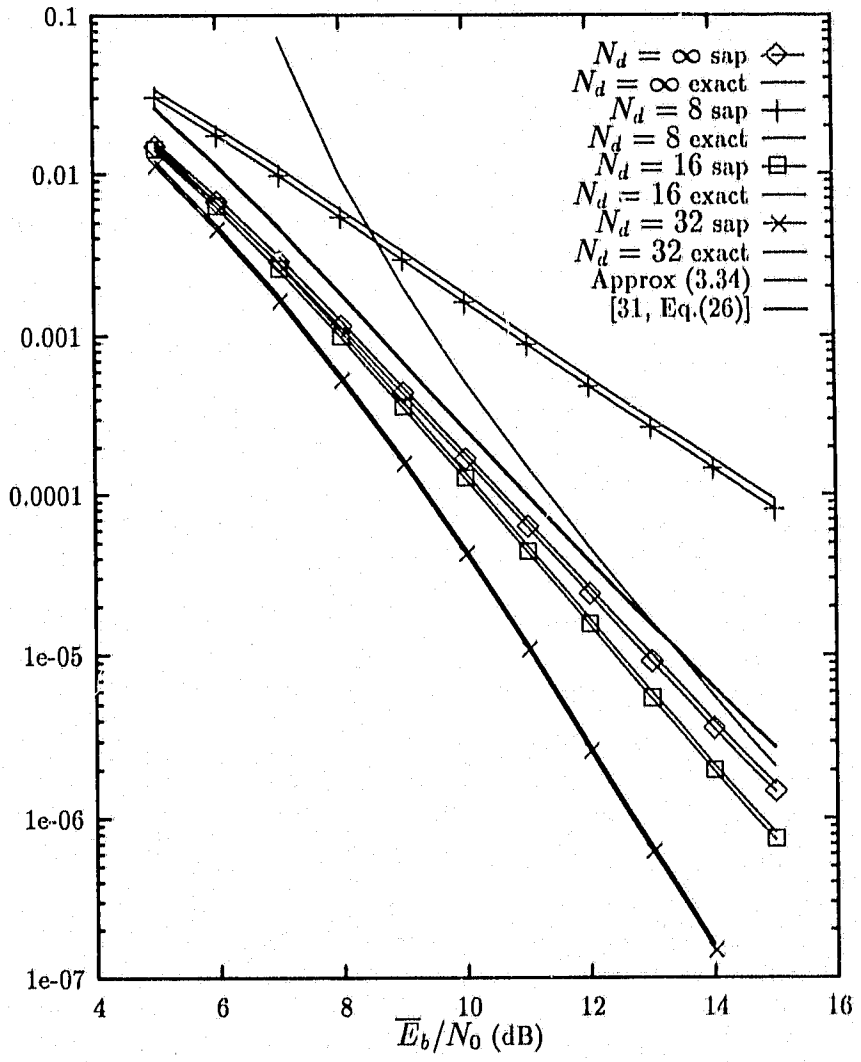

Figure 3.2: Approximate P_b versus $\overline{E}_b/N_0$. Four-state TC-4DPSK, Rician fading ($K = 5$ dB), $f_D T_s = 0.02$ with Bessel correlation.

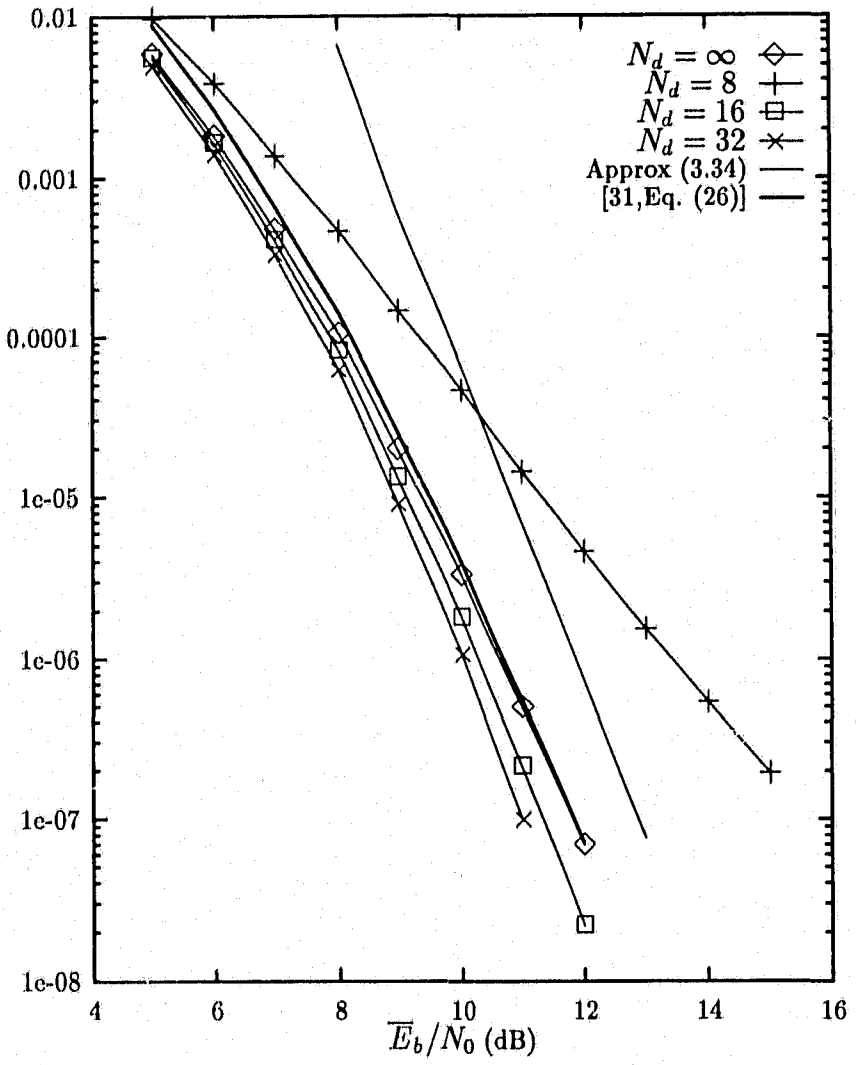

Figure 3.3: Approximate P_b versus $\overline{E}_b/N_0$. Four-state TC-4DPSK, Rician fading ($K = 10$ dB), $f_D T_s = 0.02$ with Bessel correlation.

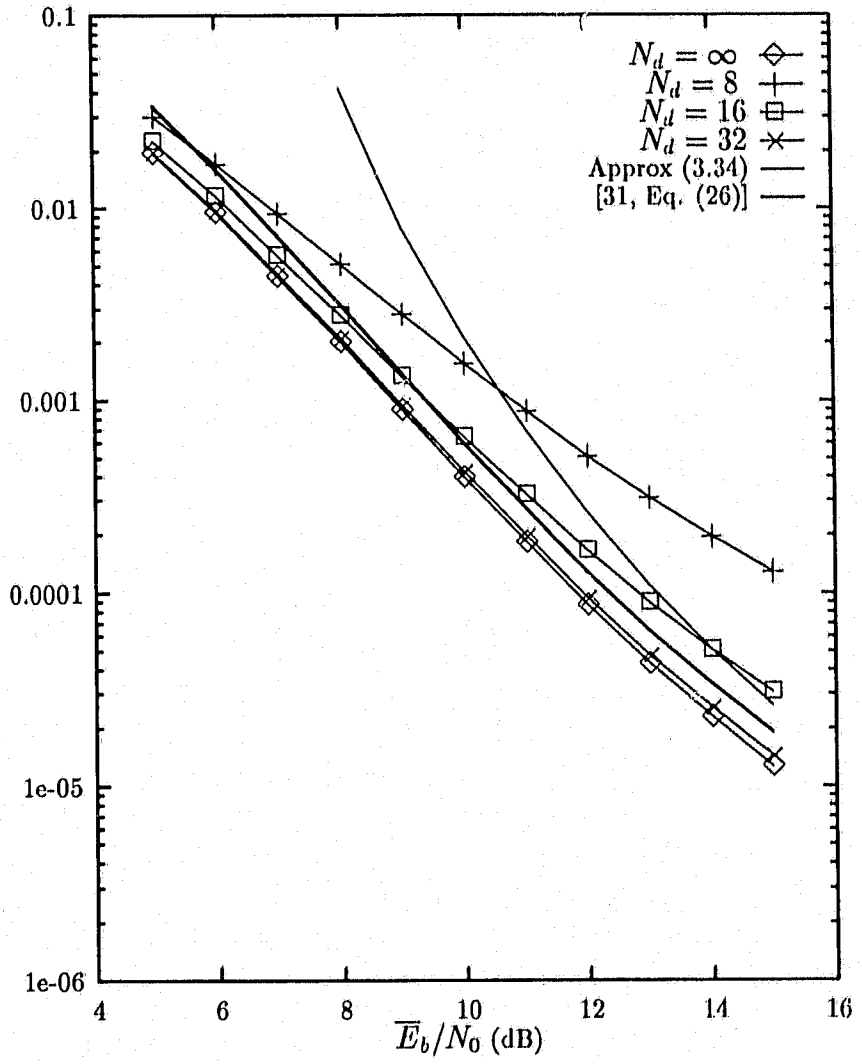

Figure 3.4: Approximate P_b versus $\overline{E}_b/N_0$. Four-state TC-4DPSK, Rician fading ($K = 5$ dB), $f_D T_s = 0.02$ with exponential correlation.

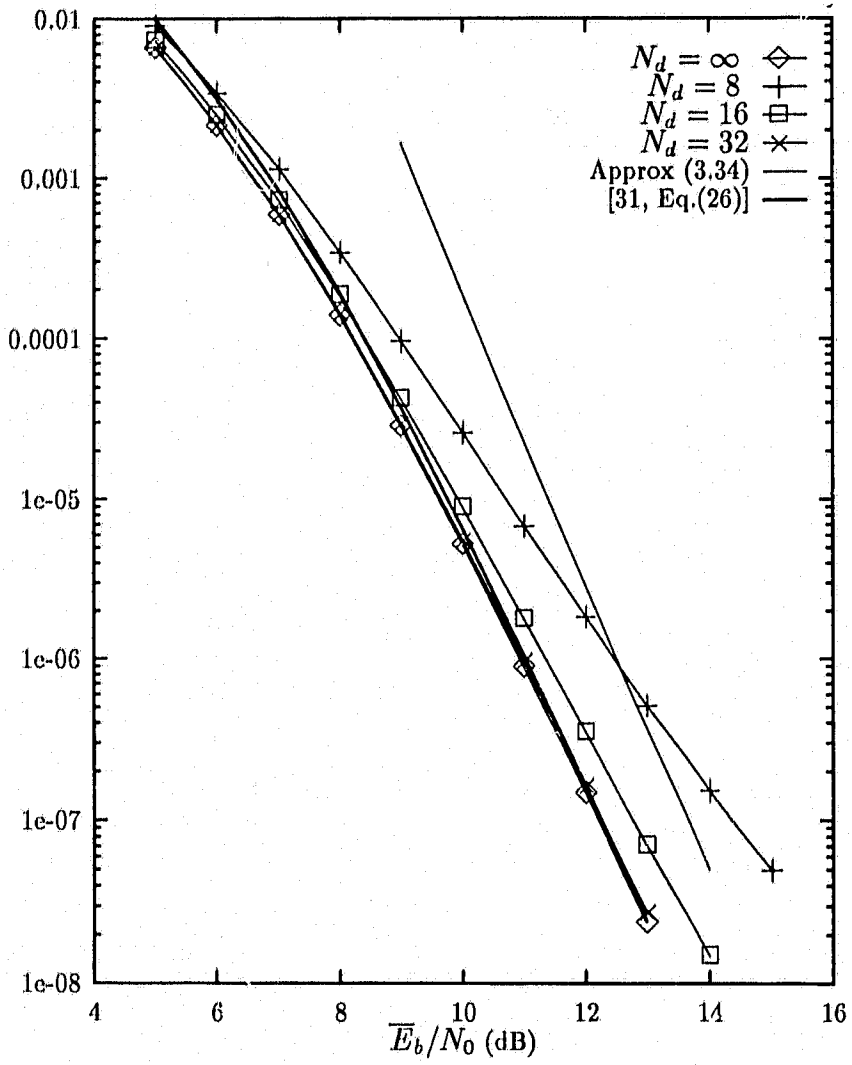

Figure 3.5: Approximate P_b versus $\overline{E}_b/N_0$. Four-state TC-4DPSK, Rician fading ($K = 10$ dB), $f_D T_s = 0.02$ with exponential correlation.

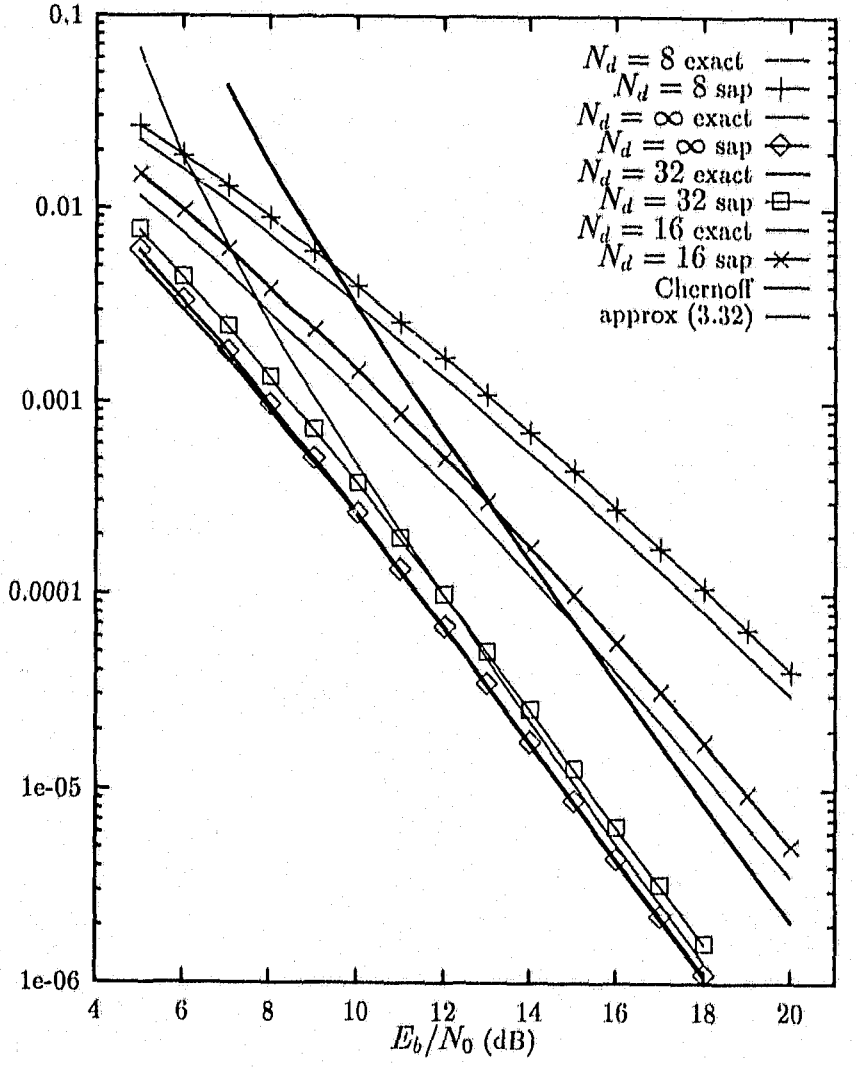

Figure 3.6: Approximate P_b versus $\overline{E}_b/N_0$. Four-state TC-4PSK, Rayleigh fading ($K = -\infty$ dB), $f_D T_s = 0.01$ with Bessel correlation.

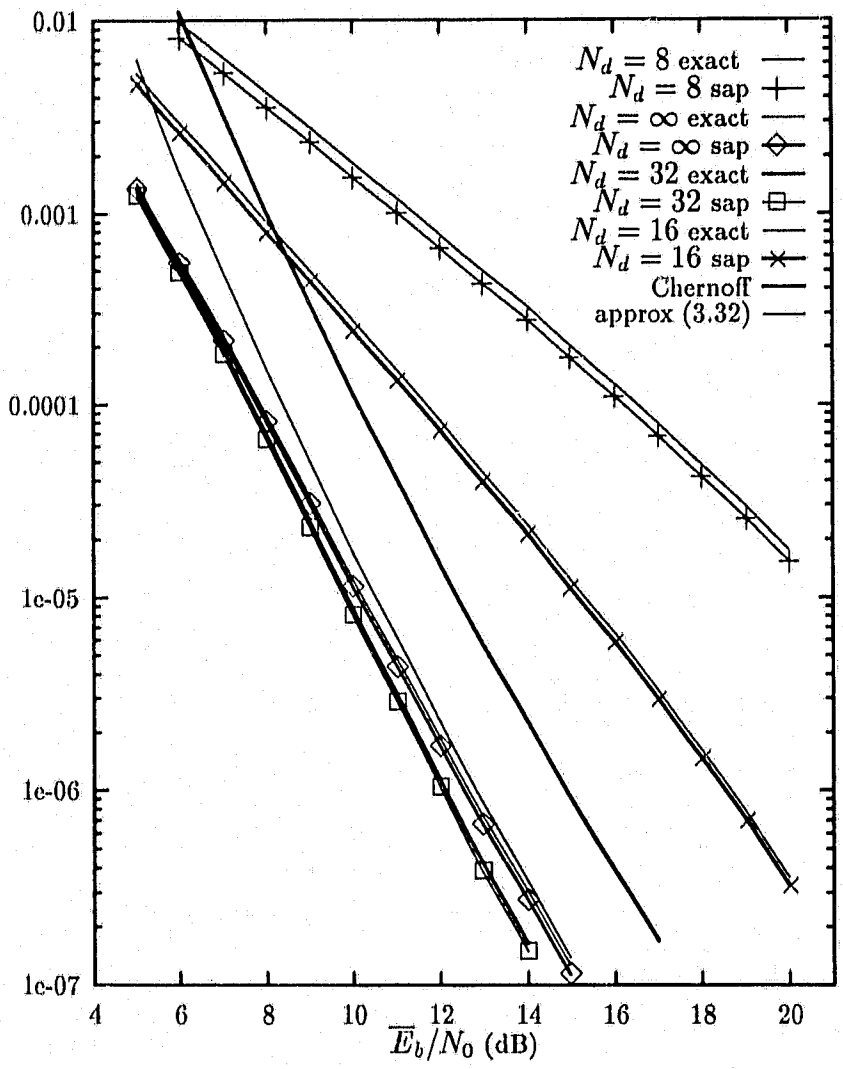

Figure 3.7: Approximate P_b versus $\overline{E}_b/N_0$. Four-state TC-4PSK, Rician fading ($K = 5$ dB), $f_D T_s = 0.01$ with Bessel correlation.

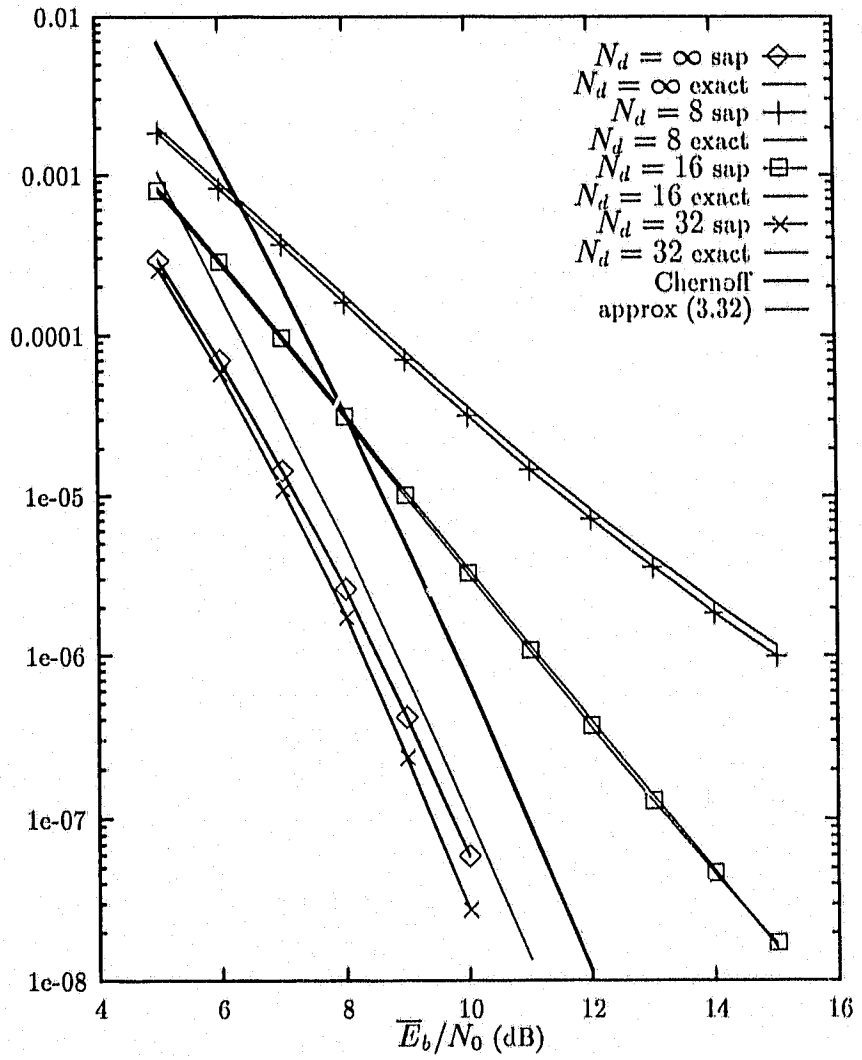

Figure 3.8: Approximate P_b versus $\overline{E}_b/N_0$. Four-state TC-4PSK, Rician fading ($K = 10$ dB), $f_D T_s = 0.01$ with Bessel correlation.

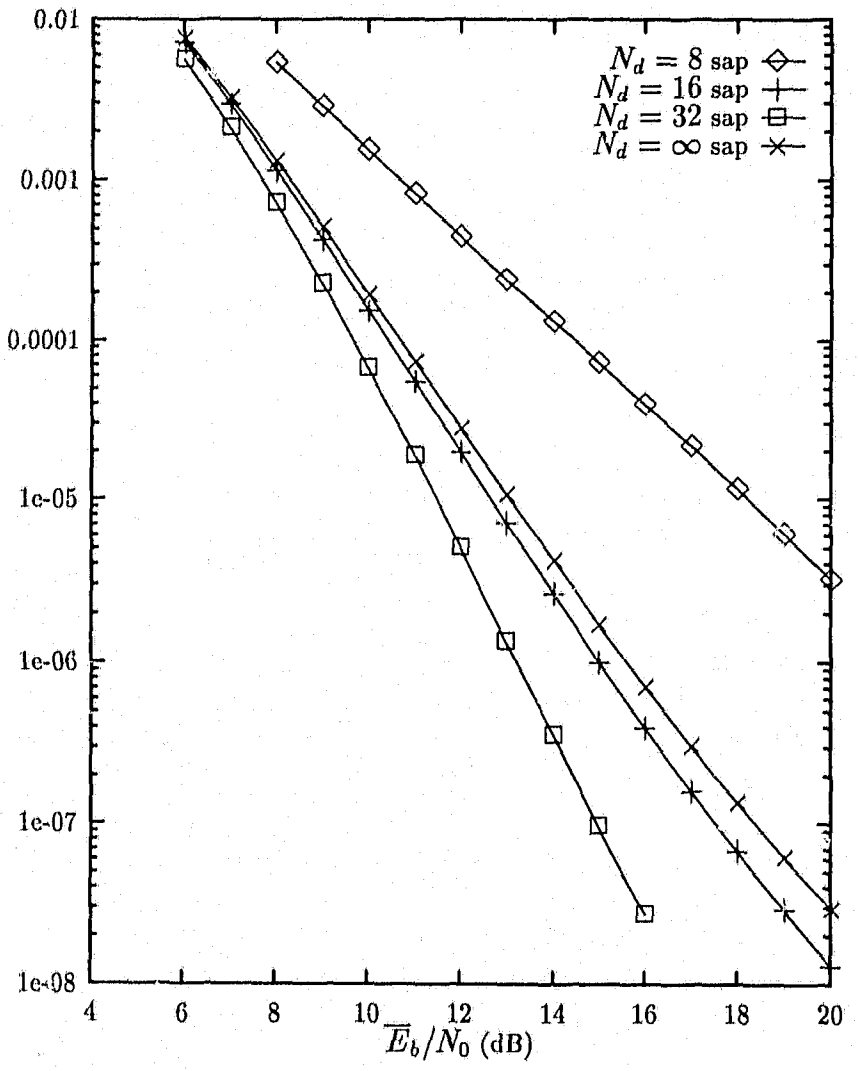

Figure 3.9: Approximate P_b versus $\overline{E}_b/N_0$. Four-state TC-4DPSK, light shadowed Rician fading, $f_D T_s = 0.02$ with Bessel correlation.

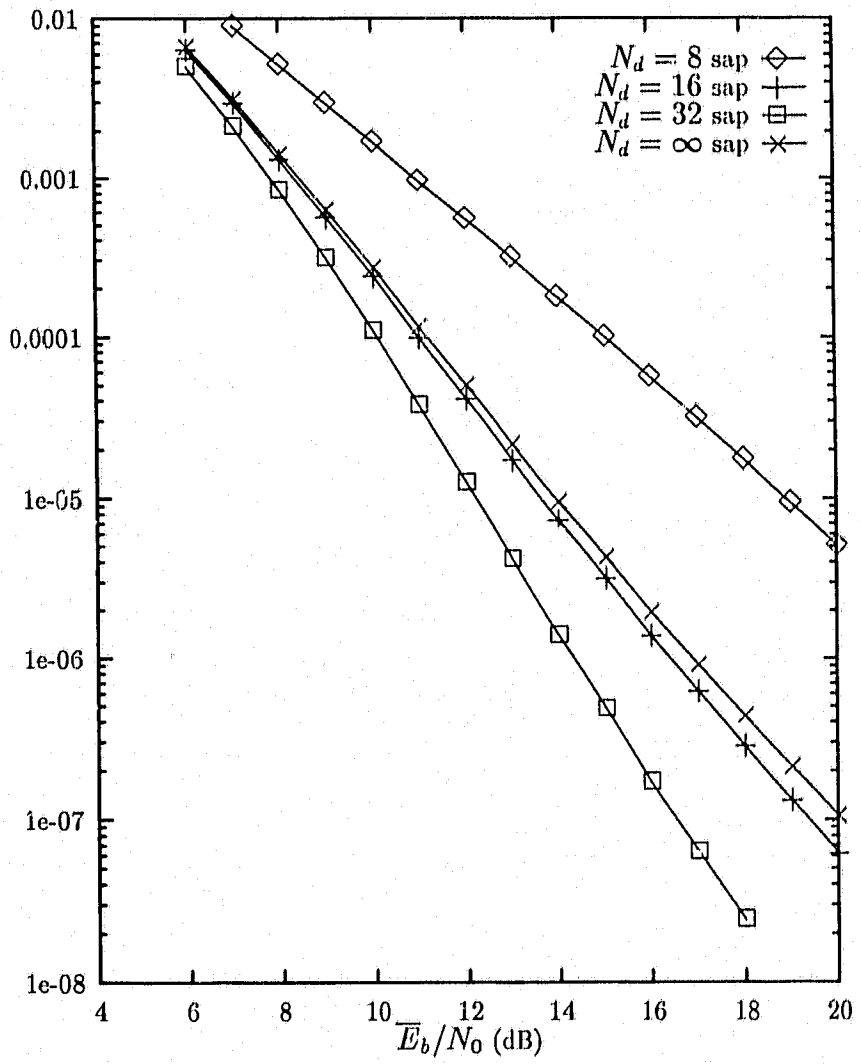

Figure 3.10: Approximate P_b versus $\overline{E}_b/N_0$. Four-state TC-4DPSK, average shadowed Rician fading, $f_D T_s = 0.02$ with Bessel correlation.

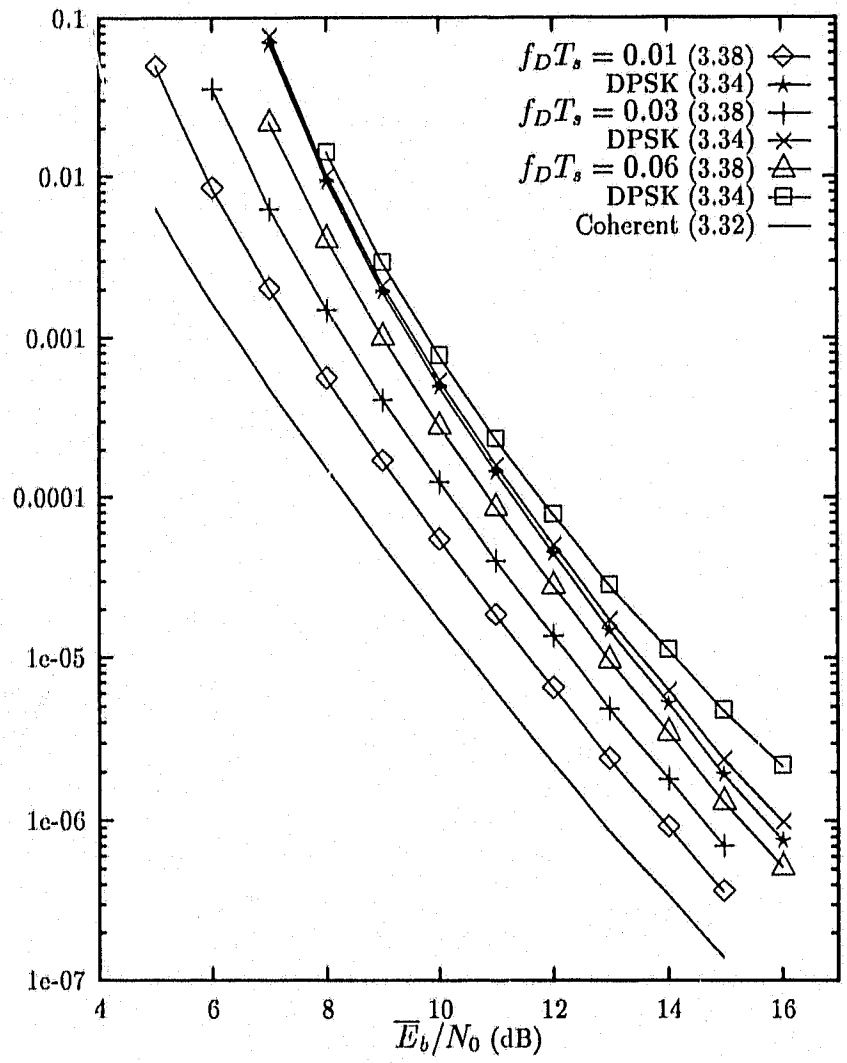

Figure 3.11: Approximate P_b versus $\overline{E}_b/N_0$. Four-state TC-PT-4PSK, Rician fading ($K = 5$ dB).

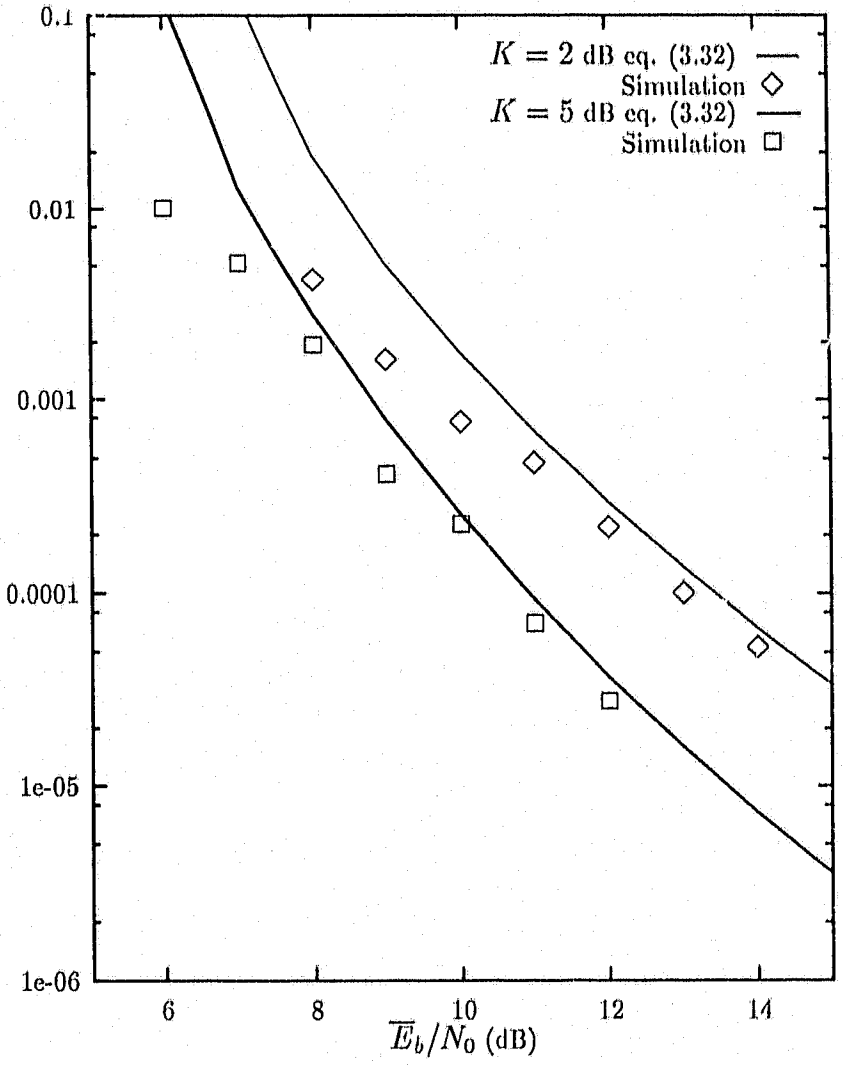

Figure 3.12: P_b versus $\overline{E}_b/N_0$. Eight-state TC-8PSK, Rician fading ($K = 5$ dB).

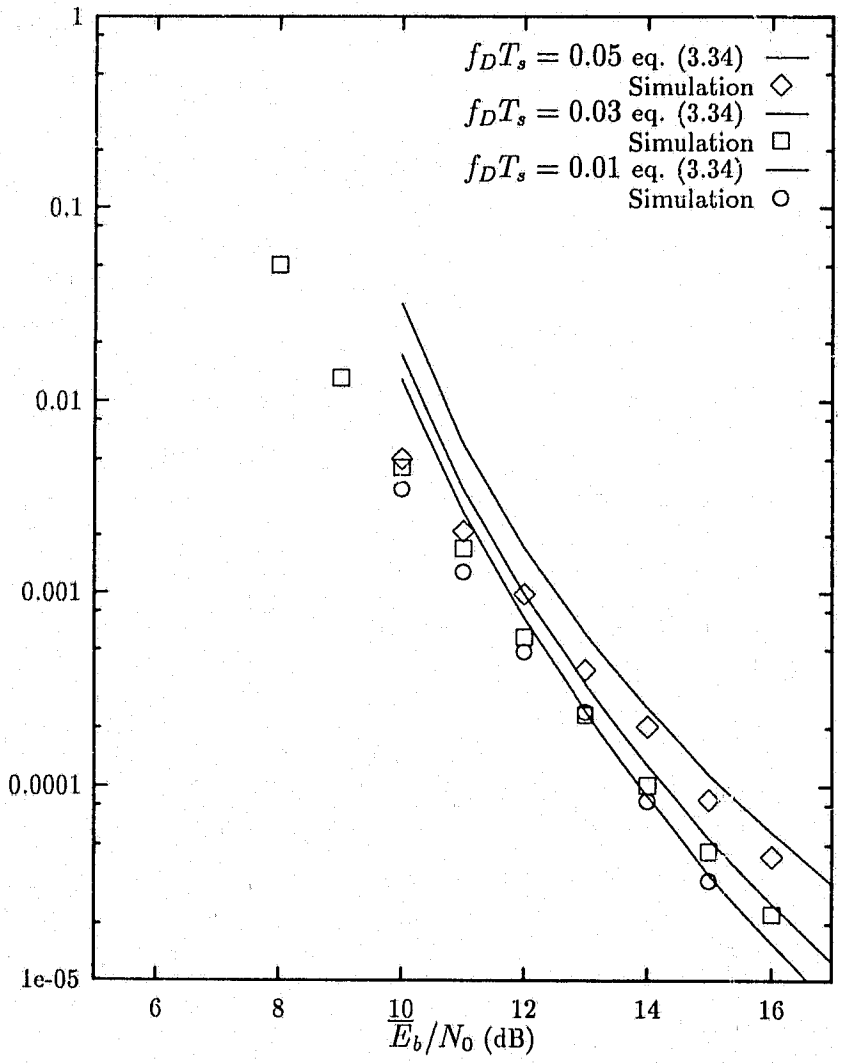

Figure 3.13: P_b versus $\overline{E}_b/N_0$. Eight-state TC-8DPSK, Rician fading ($K = 5$ dB).

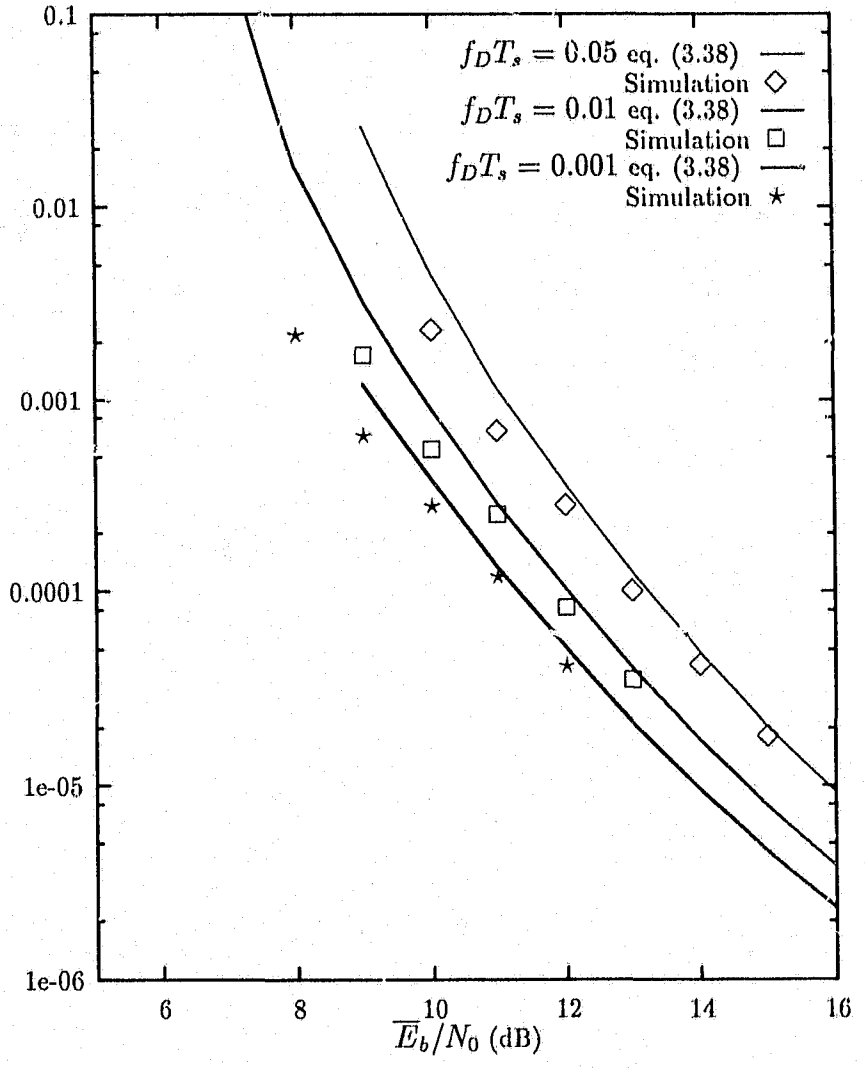

Figure 3.14: P_b versus $\overline{E}_b/N_0$. Eight-state TC-PT-8PSK, Rician fading ($K = 5$ dB).

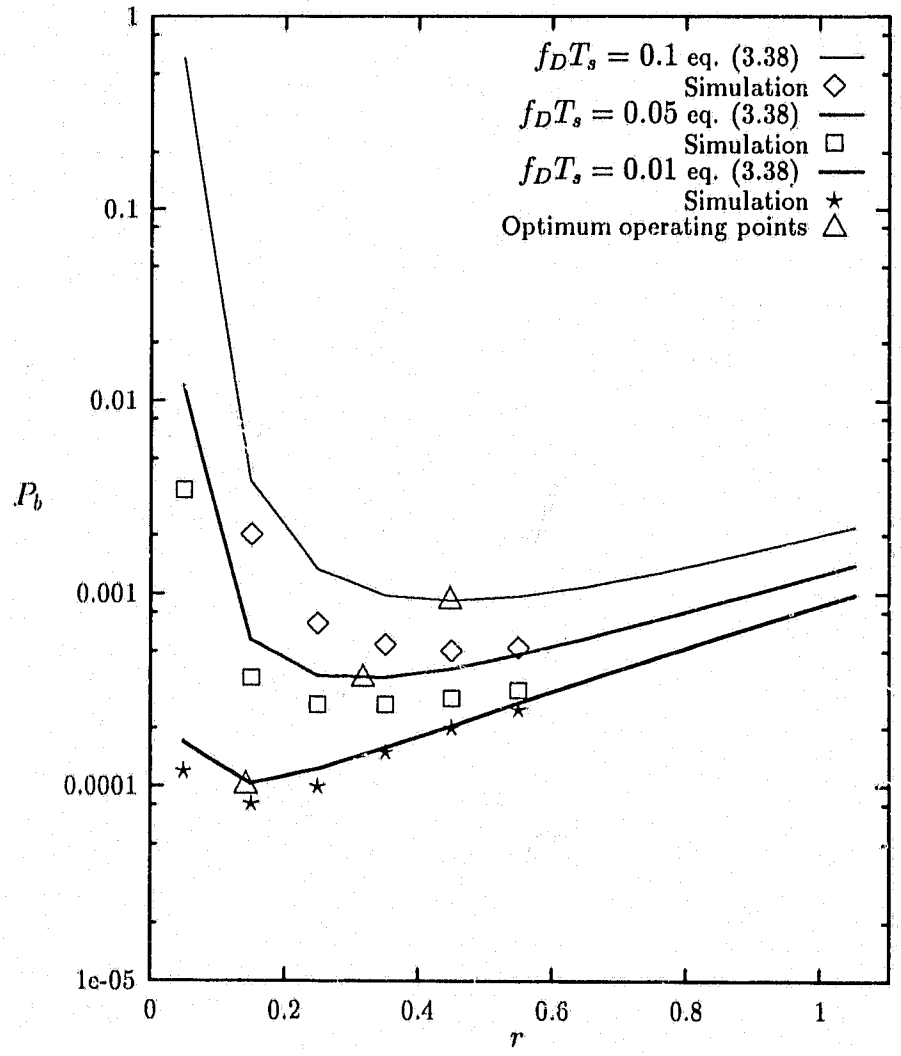

Figure 3.15: P_b versus r, the power split ratio. Rician fading ($K = 5$ dB). $\overline{E_b}/N_0 = 12$ dB.

Chapter 4

Performance of TCM on Shadowed Rician Channels

4.1 Introduction

In this chapter, we evaluate the performance of TCM in shadowed Rician fading channels. To accomplish this, taking an approach similar to that of the last chapter, we derive several new error bounds. While Chapter 3 provided numerical solutions for this case, this chapter develops analytical approximations.

As mentioned in previous chapters, mobile satellite channels are often modelled as Rician; that is, the received signal consists of a *constant* line of sight (LOS) signal component and a Rayleigh distributed diffuse signal component. In contrast, to account for the effect of foliage attenuation or blocking in a shadowed channel, the LOS component is assumed to be distributed as a lognormal variate. In application to the Canadian MSAT program, this model has been presented by Loo [43-46] and has been found to agree with measured data. A lower angle of elevation ($15° - 20°$) between a mobile user and a geosynchronous satellite implies that the effect of shadowing is more pronounced in Canada than in the United States [35]. We shall describe this model in more detail later.

Many studies have been carried out to determine the applicability of TCM to this channel model. McLane *et al.* in [35, 47] have evaluated the performance 8-PSK and 8-DPSK trellis codes over the fast fading, shadowed Rician channel via

computer simulation. In his thesis work, Lee [48] has presented a comprehensive study of *light*[1] and *average* shadowed Rician models, including a chapter on the performance of TCM over such channels. The use of a convolutional interleaver in conjunction with several TCM schemes over the same channel has been presented by Lee and McLane [49]. Again, these two papers rely on computer simulation. The performance of TCM with coherent detection over the shadowed Rician fading channel has been presented by McKay *et al.* where the Chernoff bound on the PEP is computed with the aid of numerical integration [41]. Another related paper [50] has described computer models of the common fading channels based on underlying Gaussian processes.

To date, the only analytical expressions available for this case have been presented by Huang and Campbell [31], and their results are limited to differentially coherent detection and the *slow* fading, shadowed Rician channel. Thus, unlike the case of Rician fading channels, an analytical basis for evaluating the performance of TCM over the shadowed Rician channel is missing. In this chapter, we attempt to fill the gap by providing new, analytical error bounds for TCM schemes over both slow and fast fading, shadowed Rician channels.

In Chapter 3, as well as in [51], the approximate PEP of both TC-MPSK (trellis coded M-ary phase shift keying) and TC-MDPSK (trellis-coded M-ary differential phase shift keying) over Rician, ideally interleaved channels have been derived. Our approximation was based on the saddle point method [32, 33], and its accuracy was confirmed by extensive numerical comparisons. In this chapter, we extend this earlier result by deriving new error bounds for the shadowed Rician fading channel, present Monte-Carlo simulation results to confirm their accuracy. We also derive the approximate probability density functions (PDF's) of both the absolute and differential phases, and show that the absolute phase is Gaussian for small values.

This chapter is organized as follows. Section 4.2 describes the system model

[1]The terms light and average denote the degree of fading, and the heavy fading channel will not be considered here.

used here and the characterisation of the shadowed Rician model. The approximate PEP is derived in Sections 4.3 and 4.4. First order statistics of the phase of a shadowed channel are examined in Section 4.5. Simulation results are presented in Section 4.6. Finally, a summary is provided in Section 4.7.

4.2 System and Channel Model

Our system model is described in detail in Chapter 2. In this chapter, we only consider *ideally interleaved* channels. The ensuing independent fading approximation allows us to obtain a simple upper bound on the average bit error probability, which gives the performance limits of practical systems. In fact, the ideal interleaving condition can be achieved without much difficulty for some mobile communication systems. For instance, typical Doppler spread and the symbol duration product varies in the range $0.01 \leq f_D T_s \leq 0.1$ for L-band frequencies, at 2400 baud rate and at normal vehicle speeds. The use of interleaving for this application has been studied by several authors, and it is found that total interleaving delay requirements can be met by several methods [35].

For the shadowed Rician channel model, as introduced by Loo [43-46], the channel gain α_k, including log normal LOS term and multipath components, is represented as follows:

$$\alpha_k = A_k + \xi_k + j\eta_k \tag{4.1}$$

where both ξ_k and η_k are two real independent Gaussian random variables with zero mean and variance b_0. The remaining term A_k is equal to $\exp(\zeta_k)$ where ζ_k is Gaussian with mean μ_0 and variance d_0 (note that A_k is a constant for non-shadowed Rician fading channels.). The random variables ξ_k, η_k, and ζ_k are generated by filtering three independent Gaussian random number sequences. Three identical third-order Butterworth filters of 3-dB cutoff frequency $f_D T_s$ are used for shaping the fading spectrum (see Fig. 4.1). The measured parameters of this model are given in Table 4.1 [35]. Note that the fading is represented by a single

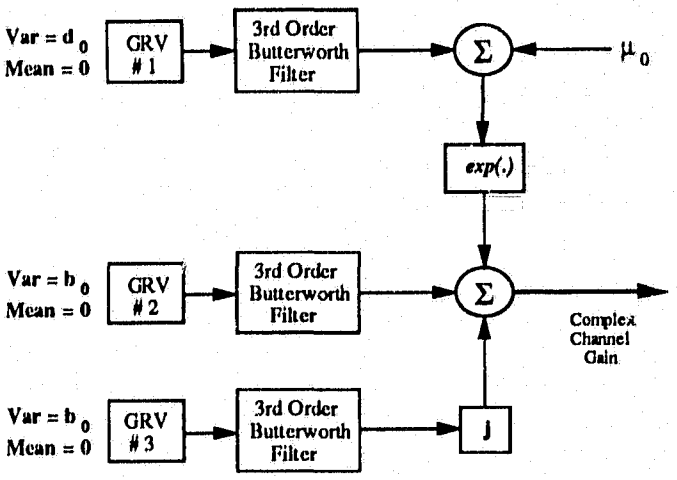

Figure 4.1: The Shadowed Fading Simulator.

sample throughout a symbol interval. This piecewise-constant approximation to the fading process is justified since the fading is slow ($f_D T_s \ll 1$).

Since ξ, η, and ζ have the same fading spectrum, when introducing the autocorrelation function of these, it is convenient to define a wild card # denoting ξ, η or ζ. The filter transfer function of a third-order Butterworth filter is [52]

$$|H(f)|^2 = \frac{3}{2\pi f_0} \frac{1}{1+(f/f_0)^6} \tag{4.2}$$

where f_0 is the 3-dB cut-off frequency. Also this spectrum has unit energy gain; that is, the total area under $|H(f)|^2$ is unity. The output normalized autocorrelation function is given by [52]

$$\begin{aligned} \rho(\tau) &\triangleq \overline{\#(t)\#(t+\tau)}/var(\#) \qquad (4.3) \\ &= \frac{1}{2}\left[\exp(-2\vartheta) + \exp(-\vartheta)(\sqrt{3}\sin(\sqrt{3}\vartheta) + \cos(\sqrt{3}\vartheta))\right] \end{aligned}$$

where $\vartheta = |\pi f_0 \tau|$. We will later need the normalized correlation coefficient between two adjacent samples:

$$\overline{\#_k \#_{k-1}} = \rho(T_s). \tag{4.4}$$

parameter	Light	Average	Heavy
b_0	0.158	0.126	0.0631
μ_0	0.115	-0.115	-3.91
$\sqrt{d_0}$	0.115	0.161	0.806

Table 4.1: Shadowed Rician Model.

As defined in (4.1), A_k is a lognormally distributed random variable having the PDF

$$p(x) = \begin{cases} \frac{1}{\sqrt{2\pi d_0}x} \exp\left(-\frac{(\log(x)-\mu_0)^2}{2d_0}\right), & x > 0 \\ 0, \text{ elsewhere.} \end{cases} \tag{4.5}$$

Note that for Rician we made the normalization $\langle|\alpha_k|^2\rangle = 1$. This, however, is not the case for shadowed Rician channel model. It can be readily shown that

$$\langle|\alpha_k|^2\rangle = \exp(2\mu_0 + 2d_0) + 2b_0, \tag{4.6}$$

which, for example, is 2.06 dB for the light shadowed fading model (Table 4.1). This factor will be included in all signal-to-noise ratio calculations.

For later PEP calculations, we shall first "fix" the additive lognormal component of the channel gain α_k, obtain the PEP conditional on the sequence of the A_k's, and then integrate the conditional PEP over the joint PDF of the A_k's. This approach is justified since the lognormal process is assumed to be completely independent of the multipath process.

4.3 The PEP in Fast Lognormal Shadowing

As in Section 3.3, we assume here the availability of some kind of channel measurements; that is, for a sequence of true channel gains $(\alpha_1, \alpha_2, \ldots, \alpha_N)$, there corresponds a sequence of channel estimator [16] outputs denoted as $(\hat{\alpha}_1, \hat{\alpha}_2, \ldots, \hat{\alpha}_N)$. Obviously, the performance of the coded system will be heavily dependent upon the accuracy of these estimates. Eq. (3.6) shows how these estimates are derived depending on the detection technique used.

According to Section 3.3, the Viterbi decoder metric is defined as

$$m(y_k, x_k) = -|y_k - \beta\hat{\alpha}_k x_k|^2 \tag{4.7}$$

where β is equal to $\mu\sqrt{b_0/b_1}$. Also, the variance of $\hat{\alpha}_k$ is $b_1 = \frac{1}{2}\langle(\hat{\alpha}_k - \overline{\hat{\alpha}}_k)(\hat{\alpha}_k - \overline{\hat{\alpha}}_k)^*\rangle$ where $*$ denotes the complex conjugate. The normalized correlation coefficient between $\hat{\alpha}_k$ and α_k is $\mu = \frac{1}{2}\langle(\alpha_k - \overline{\alpha}_k)(\hat{\alpha}_k - \overline{\hat{\alpha}}_k)^*\rangle/\sqrt{b_0 b_1}$. Note also that if perfect channel estimates are available, this decoding metric becomes optimal (in the maximum likelihood sense). Pilot-tone based detection and differential detection approach this ideal performance limit under slow fading and high signal-to-noise ratio conditions.

As we have seen, the accuracy of the approximations derived depends on the value of μ. The closer μ is to one, the more accurate are the approximations. This phenomenon is analogous to the behaviour of the bit error probability in relation to the accuracy of channel state information. For this reason, we do not consider the absence of channel state information [12], where the channel estimate just consists of phase information and is devoid of amplitude information. In this case, it can be readily shown that the value of μ is less than 0.9, making our approximation inapplicable.

Based on the above decoding metric, the PEP can be expressed as

$$P(\mathbf{x} \to \hat{\mathbf{x}}) = \Pr\{\Xi < 0\} \tag{4.8}$$

where

$$\Xi = \sum_{i=1}^{L} y_{k_i}\beta^*\hat{\alpha}_{k_i}^*(x_{k_i} - \hat{x}_{k_i})^* + y_{k_i}^*\beta\hat{\alpha}_{k_i}(x_{k_i} - \hat{x}_{k_i}). \tag{4.9}$$

For the PEP in (4.8), under the conditions $\gamma_s \to \infty$, and $\mu \approx 1$, an approximation has been derived in Eq. (3.29) (also in [51, Eq. (30)]). As shown there, for the Rician fading channel we have

$$P(\mathbf{x} \to \hat{\mathbf{x}}) \cong B(L)\prod_{i=1}^{L}\frac{\Gamma}{b_0|\mu|^2|x_{k_i} - \hat{x}_{k_i}|^2 + \Gamma}\exp\left(\frac{A^2\theta|x_{k_i} - \hat{x}_{k_i}|^2}{b_0|\mu|^2|x_{k_i} - \hat{x}_{k_i}|^2 + \Gamma}\right) \tag{4.10}$$

where

$$B(L) \cong \frac{1}{\sqrt{2\pi(2L+1)}}, \qquad \Gamma = 4((1-|\mu|^2)b_0 + \sigma^2), \tag{4.11}$$

and

$$0 = \left[-\beta + \frac{2(b_0+b_1+\sigma^2)|\beta|^2 - 4\beta|\mu|^2 b_0}{\Gamma}\right]. \tag{4.12}$$

Although this approximation has been obtained for constant A_k, it is also true when A_k varies over the duration of an error event. This assertion holds because the saddle point in this case (Eq. (3.28)) is completely independent of the value of A. Thus, denoting $\underline{A} = (A_1, A_2, \ldots, A_L)$ the above becomes the conditional PEP; that is,

$$P(\mathbf{x} \to \hat{\mathbf{x}}|\underline{A}) \cong B(L) \prod_{i=1}^{L} \frac{\Gamma}{b_0|\mu|^2|x_{k_i} - \hat{x}_{k_i}|^2 + \Gamma} \exp\left(\frac{A_i^2 \theta |x_{k_i} - \hat{x}_{k_i}|^2}{b_0|\mu|^2|x_{k_i} - \hat{x}_{k_i}|^2 + \Gamma}\right). \tag{4.13}$$

Because of ideal interleaving, each A_i is independent. Thus, the PEP is

$$P(\mathbf{x} \to \hat{\mathbf{x}}) \cong B(L) \prod_{i=1}^{L} \int_{-\infty}^{\infty} \frac{\Gamma}{b_0|\mu|^2|x_{k_i} - \hat{x}_{k_i}|^2 + \Gamma} \exp\left(\frac{A_i^2 \theta |x_{k_i} - \hat{x}_{k_i}|^2}{b_0|\mu|^2|x_{k_i} - \hat{x}_{k_i}|^2 + \Gamma}\right) p(A_i) dA_i \tag{4.14}$$

where each $p(A_i)$ is given by (4.5). For light and average shadowed Rician cases (where d_0 is small), each of these intgerals can be obtained by a method given in [31, Eq. (53)], where it has been shown that

$$\int_{-\infty}^{\infty} g(t) \exp(-\gamma t^2) = \sqrt{\frac{\pi}{\gamma}} \left(g(0) + \frac{1}{4\gamma} g''(0)\right) + O(\gamma^{-5/2}), \ \gamma \to \infty. \tag{4.15}$$

Substituting (4.5) in (4.14), transforming $t_i = \log A_i - \mu_0$, taking $\gamma = 1/2d_0$,

and using (4.15), the approximate PEP can be expressed as

$$P(\mathbf{x} \to \hat{\mathbf{x}}) \cong B(L) \prod_{i=1}^{L} \frac{\Gamma}{b_0|\mu|^2|x_{k_i} - \hat{x}_{k_i}|^2 + \Gamma} \exp\left(-c_i\varrho^2\right)\left(1 + 2d_0c_i\varrho^2[c_i\varrho^2 - 1]\right) \tag{4.16}$$

where $\varrho = \exp(\mu_0)$ and

$$c_i = \frac{-\theta|x_{k_i} - \hat{x}_{k_i}|^2}{b_0|\mu|^2|x_{k_i} - \hat{x}_{k_i}|^2 + \Gamma}. \tag{4.17}$$

This expression (4.16) can be readily used to compute the approximate P_b via the standard transfer function technique (see (3.46)).

Next we specialize this expression for the several detection methods.

4.3.1 Ideal TC-MPSK

Here, by definition, we have an ideal estimate of the channel gain; that is, $\hat{\alpha}_k = \alpha_k$. Thus $b_1 = b_0$, $\mu = 1$, $\beta = 1$, and $\theta = -0.5$. Substituting these values in (4.16) leads to the expression

$$P(\mathbf{x} \to \hat{\mathbf{x}}) \cong B(L) \prod_{i=1}^{L} \frac{1 + 2d_0c_i\varrho^2[c_i\varrho^2 - 1]}{1 + \frac{b_0}{2}|x_{k_i} - \hat{x}_{k_i}|^2\gamma_s} \exp\left(-c_i\varrho^2\right) \tag{4.18}$$

where

$$c_i = \frac{\frac{1}{4}|x_{k_i} - \hat{x}_{k_i}|^2\gamma_s}{1 + \frac{b_0}{2}|x_{k_i} - \hat{x}_{k_i}|^2\gamma_s}. \tag{4.19}$$

To roughly assess the accuracy of (4.18), we compare it with the Chernoff bound for this case. Using [12, Eq. (20)] and [31, Eq. (9)], it can be readily shown that

$$P(\mathbf{x} \to \hat{\mathbf{x}}) \leq \frac{1}{2} \prod_{i=1}^{L} \frac{1}{\sqrt{\pi}} \frac{1}{1 + \frac{b_0}{2}|x_{k_i} - \hat{x}_{k_i}|^2\gamma_s} \psi_i \tag{4.20}$$

where

$$\psi_i = \int_{-\infty}^{\infty} \exp\left(-v^2 - \frac{\frac{1}{4}|x_{k_i} - \hat{x}_{k_i}|^2\gamma_s}{1 + \frac{b_0}{2}|x_{k_i} - \hat{x}_{k_i}|^2\gamma_s} \exp\left(2\sqrt{2d_0}v + 2\mu_0\right)\right) dv \qquad (4.21)$$

Although this integration can be solved using quadrature algorithms, in the following, we derive an approximate expression which is accurate and insightful to the factors affecting the PEP [53]. As dicussed in [41], a factor of one half is included in (4.20).

4.3.2 Chernoff Bound

For the shadowed Rician fading model, each ρ_k the amplitude of α_k defined in Eq. (4.1) is described by the probability density function (PDF) [43]

$$p(\rho_k) = \frac{\rho_k}{b_0\sqrt{2\pi d_0}} \int_0^{\infty} \frac{1}{z} \exp - \left(\frac{(\log z - \mu_0)^2}{2d_0} + \frac{\rho_k^2 + z^2}{b_0}\right) I_0\left(\frac{\rho_k z}{b_0}\right) dz \qquad (4.22)$$

for $0 \leq \rho_k < \infty$. Here, $z = e^v$; v is Gaussian with mean μ_0 and variance d_0, b_0 is the variance of the multipath component (Rayleigh distributed), $\log(\cdot)$ is the natural logarithm, and $I_0(\cdot)$ is the zero-order modified Bessel function. Depending on the degree of shadowing three cases have been identified, as indicated in Table (4.1).

The PDF in Eq. (4.22) is difficult to handle mathematically. Hence, to approximate this integral, by substituting $\log z - \mu_0 = t$, it can be converted to Laplace type:

$$\begin{aligned} p(\rho_k) &= \frac{\rho_k}{b_0\sqrt{2\pi d_0}} \int_{-\infty}^{\infty} \exp - \left(\frac{\rho_k^2 + e^{2(\mu_0+t)}}{2b_0}\right) I_0\left(\frac{\rho_k e^{(\mu_0+t)}}{b_0}\right) \exp - \left(\frac{t^2}{2d_0}\right) dt \qquad (4.23) \\ &\triangleq \int_{-\infty}^{\infty} g(t) \exp - \left(\gamma t^2\right) dt \end{aligned}$$

where $\gamma = 1/(2d_0)$ and $g(t)$ denotes the rest of the integrand in Eq. (4.24). Since γ is quite large for both light and average cases, this integral can be approximated in

terms of $g(0)$, $g''(0)$ and γ. Hence, using the second order Laplace's approximation in Eq. (4.15) for this integral, we have

$$p(\rho_k) = \frac{\rho_k}{b_0}\left[c_0\Psi_0(\rho_k) - c_1\rho_k\Psi_1(\rho_k) + c_2\rho_k^2\Psi_0(\rho_k) + c_2\rho_k^2\Psi_2(\rho_k)\right] + O(\gamma^{-5/2}) \quad (4.24)$$

where

$$\Psi_n(\rho_k) \triangleq \exp - \left(\frac{\rho_k^2 + e^{2\mu_0}}{2b_0}\right) I_n\left(\frac{\rho_k e^{\mu_0}}{b_0}\right) \quad n = 0, 1, 2, \quad (4.25)$$

in which $c_0 = 1 + 0.5d_0(\varrho_1^2 - 2\varrho_1)$, $c_1 = 0.5d_0\varrho(2\varrho_1 - 1)$, $c_2 = 0.25d_0\varrho^2$, $\varrho = \exp(\mu_0)/b_0$, $\varrho_1 = \exp(2\mu_0)/b_0$, and $I_n(\cdot)$ denotes the n-th order modified Bessel function. As defined in Section 3.3, the PEP $P(\mathbf{x} \to \hat{\mathbf{x}})$ is the probability of choosing the coded sequence $\hat{\mathbf{x}} = (\hat{x}_1, \hat{x}_2, \ldots, \hat{x}_N)$ when $\mathbf{x} = (x_1, x_2, \ldots, x_N)$ was transmitted [12], assuming $\mathbf{x}$ and $\hat{\mathbf{x}}$ the only choices. Conditional on the set of fading amplitudes $\boldsymbol{\rho} = (\rho_1, \rho_2, \ldots, \rho_n)$, the PEP is bounded as follows:

$$P(\mathbf{x} \to \hat{\mathbf{x}}|\boldsymbol{\rho}) \leq \prod_{k\epsilon\eta} \exp - \left(\frac{\overline{E}_s}{4N_0}\rho_k^2|x_k - \hat{x}_k|^2\right) \quad (4.26)$$

where η is the set of indexes k for which $x_k \neq \hat{x}_k$ [12, Eq. (20)]. Averaging the conditional error bound over each $p(\rho_k)$ in (4.24) yields

$$P(\mathbf{x} \to \hat{\mathbf{x}}) \leq \prod_{k\epsilon\eta} \frac{\theta_k}{1 + b_0\frac{\overline{E}_s}{2N_0}|x_k - \hat{x}_k|^2} \exp - \left(\frac{e^{2\mu_0}\frac{\overline{E}_s}{4N_0}|x_k - \hat{x}_k|^2}{1 + b_0\frac{\overline{E}_s}{2N_0}|x_k - \hat{x}_k|^2}\right) \quad (4.27)$$

where

$$\theta_k \triangleq c_0 - \frac{b_0 d_0 \varrho^2(\varrho_1 - 1)}{1 + b_0\frac{\overline{E}_s}{2N_0}|x_k - \hat{x}_k|^2} + \frac{0.5d_0\varrho^4}{(1 + b_0\frac{\overline{E}_s}{2N_0}|x_k - \hat{x}_k|^2)^2}. \quad (4.28)$$

In deriving eqn. (4.27), we have made use of certain identities involving Bessel functions, and these can be found in [54]. Note that for large signal-to-noise ratios

the second and third terms of θ_k tend to zero. This error bound can be readily used with the transfer function of a trellis encoder to find the bit error probability, and adds insight to the effect of the channel and code parameters that affect the overall performance. To wit, eqn. (4.27) indicates that for the shadowed Rician channel, as for a Rician channel, TCM schemes should be designed to maximize (1) the length of the shortest error event path, and (2) the product of branch distances along that path.

4.3.3 TC-MDPSK

Here, for any signalling period, the preceding signal provides the channel estimate; that is, $\hat{\alpha}_k = \alpha_{k-1} + n_{k-1}$ (see (2.6), (2.8), and (3.6)). The term v_{k-1} is now absorbed in the channel gain term. Hence, the channel estimate has a variance of $b_1 = b_0 + \sigma^2$ and it follows that

$$|\mu|^2 = \frac{b_0 \rho^2(T_s)}{b_0 + 0.5\gamma_s^{-1}} = \frac{b_0 \delta}{b_0 + 0.5\gamma_s^{-1}} \tag{4.29}$$

where $\rho(\cdot)$ is the normalized autocorrelation function for a 3-rd order Butterworth spectrum given by (4.4). An examination of (4.29) reveals two facts. First, for very slow fading (i.e., $\rho(T_s) \approx 1$), at large signal-to-noise ratios μ approaches unity. Hence, the quality of the channel estimates is ideal. Second, for fast fading ($\rho(T_s) < 1$), no matter how large the signal-to-noise ratio, μ remains less than unity. This implies a fixed bit error probability as $\gamma_s \to \infty$, which is usually termed as an "error floor."

Substituting $|\mu|^2$ in (4.16) results in the expression

$$P(\mathbf{x} \to \hat{\mathbf{x}}) \cong B(L) \prod_{i=1}^{L} \frac{(b_0(1-\delta)\gamma_s + 1 + (4b_0\gamma_s)^{-1})(1 + 2d_0 c_i \varrho^2 [c_i \varrho^2 - 1])}{\frac{b_0}{4}\delta |x_{k_i} - \hat{x}_{k_i}|^2 \gamma_s + b_0(1-\delta)\gamma_s + 1 + (4b_0\gamma_s)^{-1}} \exp(-c_i \varrho^2) \tag{4.30}$$

where

$$c_i = \frac{-0.25\theta|x_{k_i} - \hat{x}_{k_i}|^2\gamma_s(1 + 0.5(b_0\gamma_s)^{-1})}{\frac{b_0}{4}\delta|x_{k_i} - \hat{x}_{k_i}|^2\gamma_s + b_0(1-\delta)\gamma_s + 1 + (4b_0\gamma_s)^{-1}}. \tag{4.31}$$

As noted in [51], the accuracy of (4.30) will decrease with the increasing Doppler spread. The is due to the fact that the increased Doppler decreases the value of μ, as shown in (4.29). For the three shadowing cases, the value of b_0 decreases from light to heavy; as a result, the performance of differentially detected TCM degrades, and so does the accuracy of (4.30). Note also that comparing the PEP for TC-MPSK (4.18) and that of TC-MDPSK (4.30) reveals that the latter is inferior by 3 dB.

4.3.4 TC-PT-MPSK

As an alternative to differential detection, the α_k's may be measured by transmitting a pilot tone [16] along side the data. If a reference tone is transmitted along with the data signal (both within the coherence bandwidth of the fading process), and if this tone can be filtered ideally, the resulting system performance will be almost equal to that of ideal coherent detection. Here, we assume these conditions, and a further discussion regarding the validity of these assumptions can be found in [55].

If $\hat{\alpha}_k$ is the pilot-tone based estimate of α_k, then it can be shown that (Section 3.3.5)

$$var(\hat{\alpha}_k) = b_1 = b_0 + 0.5\,(B_pT_s)\left(\frac{1+r}{r}\right)\gamma_s^{-1}, \tag{4.32}$$

$$|\mu|^2 = \frac{b_0}{b_0 + 0.5\,(B_pT_s)\left(\frac{1+r}{r}\right)\gamma_s^{-1}}$$

where γ_s now accounts for the total symbol energy spent on both the data and the pilot-tone. We note here that as $\overline{E}_s/N_0$ increases the value of $|\mu|^2$ approaches

unity. Thus, at large signal-to-noise ratios, the pilot tone technique is essentially equivalent to ideal coherent detection.

By substituting these in (4.16), we have

$$P(\mathbf{x}\to\hat{\mathbf{x}}) \cong B(L)\prod_{i=1}^{L}\frac{[\frac{B_pT_s(1+r)}{r}+1+r]+\frac{B_pT_s(1+r)^2}{2b_0r}\gamma_s^{-1}}{\frac{b_0}{2}|x_{k_i}-\hat{x}_{k_i}|^2\gamma_s+[\frac{B_pT_s(1+r)}{r}+1+r]+\frac{B_pT_s(1+r)^2}{2b_0r}\gamma_s^{-1}} \times \exp\left(-c_i\varrho^2\right)\left(1+2d_0c_i\varrho^2[c_i\varrho^2-1]\right) \tag{4.33}$$

where

$$c_i=\frac{-0.5\theta|x_{k_i}-\hat{x}_{k_i}|^2\gamma_s(1+\frac{B_pT_s(1+r)^2}{2b_0r}\gamma_s^{-1})}{\frac{b_0}{2}|x_{k_i}-\hat{x}_{k_i}|^2\gamma_s+[\frac{B_pT_s(1+r)}{r}+1+r]+\frac{B_pT_s(1+r)^2}{2b_0r}\gamma_s^{-1}}. \tag{4.34}$$

4.3.5 TC-PS-MPSK

In this system, periodically embedded pilot symbols are filtered to estimate the true channel gain. Following Section 3.3.6 and considering a frame of size N, we find that

$$P(\mathbf{x}\to\hat{\mathbf{x}}) \cong B(L)\prod_{i=1}^{L}\frac{[B_pT_sN+\frac{N}{N-1}]+\frac{B_pT_sN^2}{2b_0(N-1)}\gamma_s^{-1}}{\frac{b_0}{2}|x_{k_i}-\hat{x}_{k_i}|^2\gamma_s+[B_pT_sN+\frac{N}{N-1}]+\frac{B_pT_sN^2}{2b_0(N-1)}\gamma_s^{-1}} \times \exp\left(-c_i\varrho^2\right)\left(1+2d_0c_i\varrho^2[c_i\varrho^2-1]\right) \tag{4.35}$$

where

$$c_i=\frac{-0.5\theta|x_{k_i}-\hat{x}_{k_i}|^2\gamma_s(1+\frac{B_pT_sN^2}{2b_0(N-1)}\gamma_s^{-1})}{\frac{b_0}{2}|x_{k_i}-\hat{x}_{k_i}|^2\gamma_s+[B_pT_sN+\frac{N}{N-1}]+\frac{B_pT_sN^2}{2b_0(N-1)}\gamma_s^{-1}}. \tag{4.36}$$

4.4 The PEP for Slow Lognormal Shadowing

In the preceeding discussion, we assumed that all three components of the channel gain (4.1) have an equal fading bandwidth. In the following, we assume that

the lognormal component varies slowly in comparison to the multipath component. Consequently, the lognormal variate A_k in (4.1) will remain constant during short error events. In other words, the interleaving depth is sufficient to break up correlations due to multipath components but not those due to the shadowing component.

As derived for the case of fast fading, the PEP here too is

$$P(\mathbf{x} \to \hat{\mathbf{x}}) \cong \int_{-\infty}^{\infty} \left[B(L) \prod_{i=1}^{L} \frac{\Gamma}{b_0|\mu|^2|x_{k_i} - \hat{x}_{k_i}|^2 + \Gamma} \exp\left(\frac{A^2\theta|x_{k_i} - \hat{x}_{k_i}|^2}{b_0|\mu|^2|x_{k_i} - \hat{x}_{k_i}|^2 + \Gamma} \right) \right] p(A)dA \tag{4.37}$$

where $p(A)$ is given by (4.5). This can be evaluated in the same manner as in the case of fast fading. Consequently, we maintain that for the light and average shadowing models the PEP is given by

$$P(\mathbf{x} \to \hat{\mathbf{x}}) \cong B(L) \left(\prod_{i=1}^{L} \frac{\Gamma \exp(-c_i\varrho^2)}{b_0|\mu|^2|x_{k_i} - \hat{x}_{k_i}|^2 + \Gamma} \right) \left(1 + 2d_0c_0\varrho^2[c_0\varrho^2 - 1]\right) \tag{4.38}$$

where ϱ and c_i are as defined earlier, and

$$c_0 = \sum_{i=1}^{L} \frac{-\theta|x_{k_i} - \hat{x}_{k_i}|^2}{b_0|\mu|^2|x_{k_i} - \hat{x}_{k_i}|^2 + \Gamma}. \tag{4.39}$$

Unfortunately, this expression cannot be used with the transfer function method because c_0 consists of additive terms, a manifestation of our slow fading assumption. As in [31], we compute c_0 only for the shortest error event, and incorporate this value of c_0 into $B(L)$. Thus, for this case

$$B(L) = B_1(L) = \frac{1}{\sqrt{2\pi(2L+1)}} \left(1 + 2d_0c_0\varrho^2[c_0\varrho^2 - 1]\right)_{L_{min}} \tag{4.40}$$

As before, we next specialize this expression for the three detection methods.

4.4.1 Ideal TC-MPSK

As discussed earlier, we have an ideal estimate of the channel gain; that is, $\hat{\alpha}_k = \alpha_k$. Thus $b_1 = b_0$, $\mu = 1$, $\beta = 1$, and $\theta = -0.5$. Substituting these values in (4.38) leads to the expression

$$P(\mathbf{x} \to \hat{\mathbf{x}}) \cong B_1(L) \prod_{i=1}^{L} \frac{\exp(-c_i \varrho^2)}{1 + \frac{b_0}{2}|x_{k_i} - \hat{x}_{k_i}|^2 \gamma_s}. \tag{4.41}$$

Furthermore, the constant c_0 is given by

$$c_0 \approx \frac{0.5 L_{min}}{b_0}, \quad \gamma_s \to \infty, \tag{4.42}$$

which is independent of the distance structure of the shortest error event. Thus, $B_1(L)$ depends only on the length of the shortest error event.

4.4.2 TC-MDPSK

By following the discussion in Section 4.3.3, we have the PEP for a slow lognormal fading case:

$$P(\mathbf{x} \to \hat{\mathbf{x}}) \cong B_1(L) \prod_{i=1}^{L} \frac{(b_0(1-\delta)\gamma_s + 1 + (4b_0\gamma_s)^{-1}) \exp(-c_i \varrho^2)}{\frac{b_0}{4}\delta|x_{k_i} - \hat{x}_{k_i}|^2 \gamma_s + b_0(1-\delta)\gamma_s + 1 + (4b_0\gamma_s)^{-1}}. \tag{4.43}$$

4.4.3 TC-PT-MPSK

Substituting the correlation coefficient and variance (4.32) of the pilot-tone based estimate in (4.38), we have

$$P(\mathbf{x} \to \hat{\mathbf{x}}) \cong B_1(L) \prod_{i=1}^{L} \frac{\left(\left[\frac{B_p T_s (1+r)}{r} + 1 + r\right] + \frac{B_p T_s (1+r)^2}{2b_0 r}\gamma_s^{-1}\right) \exp(-c_i \varrho^2)}{\frac{b_0}{2}|x_{k_i} - \hat{x}_{k_i}|^2 \gamma_s + \left[\frac{B_p T_s (1+r)}{r} + 1 + r\right] + \frac{B_p T_s (1+r)^2}{2b_0 r}\gamma_s^{-1}}. \tag{4.44}$$

4.4.4 TC-PS-MPSK

As before, we have

$$P(\mathbf{x} \to \hat{\mathbf{x}}) \cong B_1(L) \prod_{i=1}^{L} \frac{\left([B_p T_s N + \frac{N}{N-1}] + \frac{B_p T_s N^2}{2b_0(N-1)}\gamma_s^{-1}\right) \exp\left(-c_i \varrho^2\right)}{\frac{b_0}{2}|x_{k_i} - \hat{x}_{k_i}|^2 \gamma_s + [B_p T_s N + \frac{N}{N-1}] + \frac{B_p T_s N^2}{2b_0(N-1)}\gamma_s^{-1}}. \quad (4.45)$$

4.5 Phase Jitter Analysis

Since the first-order statistics can be used to reveal the sensitivity of P_b to phase jitter, in [35, 47] the authors computed the standard deviation of the absolute and differential phases of the true channel gain. In contrast, this section derives analytical expressions for their PDF's for a fast fading, shadowed Rician channel. Specifically, denoting the k-th channel gain as $V_k e^{j\phi_k}$, we determine the PDF's of ϕ_k and $(\phi_k - \phi_{k-1})$.

4.5.1 Absolute Phase

Taking the channel gain α_k in (4.1), we drop the subscript k for notational convenience, and convert α into form $Ve^{j\phi}$. Thus, after some elementary manipulations, the conditional joint PDF of the envelope V and the phase ϕ can be obtained as:

$$p(V, \phi|A) = \frac{V}{2\pi b_0} \exp - \left(\frac{A^2 - 2AV\cos\phi + V^2}{2b_0}\right) \quad (4.46)$$

where $0 \leq V < \infty$ and $0 \leq \phi \leq 2\pi$. To find the joint PDF of (V, ϕ), (4.46) must be averaged over the PDF of A. Thus, from (4.46) and (4.5) we have

$$p(V, \phi) = \frac{V}{2\pi b_0} \frac{1}{\sqrt{2\pi d_0}} \int_{-\infty}^{\infty} \exp - \left(\frac{\varrho^2 e^{2t} - 2\varrho e^t V\cos\phi + V^2}{2b_0}\right) \exp - \left(\frac{t^2}{2d_0}\right) dt \quad (4.47)$$

where $\varrho = \exp\mu_0$, as defined earlier. Since for light and average shadowing cases d_0 is quite small, an approximate expression for this integral can be obtained as

before. Using only the first term of the expansion given in (4.15), we have

$$p(V,\phi) = \frac{V}{2\pi b_0}\exp - \left(\frac{\varrho^2 - 2\varrho V\cos\phi + V^2}{2b_0}\right) + O(d_0^{3/2}). \tag{4.48}$$

Integrating this over the variable V results in

$$p(\phi) \cong \frac{\varrho\cos\phi}{\sqrt{2\pi b_0}}\exp - \left(\frac{\varrho^2\sin^2\phi}{2b_0}\right). \tag{4.49}$$

Clearly, for small values ($\cos\phi \approx 1$, $\sin\phi \approx \phi$), ϕ is Gaussian with zero mean and variance b_0/ϱ^2. For a light fading channel, this turns out be a standard deviation of 20.3 degrees, which agrees quite well with the computed value 22.7 degrees [47]. As observed in [52], the phase process of a Rician fading process is approximately Gaussian with zero mean and variance $1/(2K)$. It thus follows that the equivalent K factor of a shadowed channel is $\varrho^2/2b_0$.

Similarly, concerning the envelope process, note that integrating (4.48) over the phase ϕ yields

$$p(V) \approx \frac{V}{b_0}\exp - \left(\frac{\varrho^2 + V^2}{2b_0}\right) I_0\left(\frac{\varrho V}{b_0}\right) \tag{4.50}$$

where $I_0(\cdot)$ is the zero-order modified Bessel function. Since this expression is the PDF of a Rician fading amplitude (see [12]), it is possible to define a K factor, as in a Rician channel. Here $K = \varrho^2/2b_0$, as also obtained above. For light and average fading models this turns out to be 6 and 5 dB, respectively. A similar observation is made in [31, 48].

In light of the foregoing, we conclude that, on a first-order basis, the light and average shadowing channels are Rician. However, if the second-order terms are included, this equivalence breaks down.

Bandwidth	Light	Average
0.025	2.3	2.7
0.05	4.4	5.1
0.1	8.1	9.3
0.2	14.3	16.0

Table 4.2: Differential Phase Jitter

4.5.2 Differential Phase

Since differential phase statistics depend on the correlation between two temporally adjacent channel gains, and since two correlated lognormal variates are also involved, this case is a lot more complicated than that of absolute phase. Note however that interleaving does not affect this correlation (differential detection exploits the intrinsic channel memory) and that interleaving is sufficient to make $(\phi_k - \phi_{k-1})$ terms independent of each other, as we have assumed at the beginning.

In view of this difficulty, we can only provide an approximate PDF that must be computed numerically. In Appendix C, it is shown that the differential phase φ is distributed approximately as

$$p(\varphi) = \int_0^{2\pi} p(\phi_1, \phi_1 + \varphi) d\phi_1 \quad \text{for} \quad -\pi \leq \varphi \leq \pi, \tag{4.51}$$

Computed values of the standard deviation of the differential phase are shown in Table 2, and they agree quite well with the values given in [35].

4.6 Results

This section presents a comparison between Monte-Carlo simulation results and the approximations we developed in the previous sections.

4.6.1 Computer Simulation

In this study, we use a rate 2/3, eight-state binary convolutional encoder (see Fig. 4.2) to confirm the accuracy of the approximations developed thus far. The reference [41] provides more details regarding the derivation of modified state transition diagram, augmented branch labels, and the modified encoder transfer function for this code.

The rate 2/3 8-state convolutional encoder with 8-PSK signal set was used to encode a random data stream (the code is taken from [41]). The receiver was implemented using a Viterbi algorithm, with the decoding metric given in (4.7). In the Viterbi decoder, a decision depth of 18 symbols was used, that is, 6 times the code memory [47]. Although our theoretical results were derived under the assumption of ideal interleaving, the simulation was carried out using a finite interleaving depth. For a fading bandwidth of 0.05, the interleaving depth was set to 10 symbols. This choice gives an effective bandwidth of 0.5, at which the correlation between any two adjacent, deinterleaved symbols becomes negligible. This effect can be verified from Eq. (4.4), where a zero of $\rho(T_s)$ is found near 1 when $f_0 = 0.5$.

In the case of pilot-tone based detection, about 30% of the transmitted power was allocated to the pilot-tone, which is optimum [16, 51] for the fading bandwidth considered herein.

When simulating the slow fading lognormal component, the bandwidth of the low-pass filter of that component (see Fig. 4.1) was set to 0.001. After interleaving, the effective lognormal fade rate would still be 0.01, which is slow enough that the lognormal component remains roughly constant for several adjacent symbol intervals (as assumed in Section 4.4).

To reduce the uncertainty of each simulation point, as in [56], each point was simulated at least twice: first with a given number of error events, second with the twice that number. This was repeated until the two results were within 10%

of each other. For $P_b > 10^{-4}$ the starting number of error events was 200, while for $P_b \leq 10^{-4}$ the number was 100. For these two ranges of P_b, the accuracy of the estimates varies from 20% to 30% with a confidence level of 95%.

For light and average cases, and for coherent, differential and pilot-tone based detection methods, we present P_b versus $\overline{E}_b/N_0$ performance in Figs. 4.3-4.8. For both coherent and pilot-tone methods, the bounds are quite tight when $P_b \leq 10^{-3}$. As noticeable from these figures, the error bounds fare better in the average shadowed channel than in the light shadowed channel. The reason is that the variance of multipath component b_0 is smaller for the former. As can be seen from [51, Eq. (27)], smaller b_0 improves the saddlepoint approximation presented therein.

For differential detection, however, the error bounds are looser, as can be seen in Figs. 4.4, 4.7. Here the error bounds will improve with decreasing Doppler. The results presented are for a 5% Doppler rate, which can be considered as a worst-case for the 800 MHz frequency band. Another reason for not considering Doppler rates above that figure is that pulse distortion and intersymbol interference effects introduced by fading can no longer be neglected.

The slow lognormal fading case is treated in Figs. 4.9-4.11. Once again, there is close agreement between error bounds and simulation results.

4.7 Summary

In this chapter new approximations for the PEP of TCM schemes operating on the shadowed Rician fading channel have been derived, which can be readily used with the transfer function method to obtain an upper bound on the bit error probability. The application of the resulting bounds has been exemplified for a moderately complex eight-state TCM scheme transmitted through this channel. For bit error rates less than 1×10^{-3}, the derived error bounds for coherent and pilot-tone detections are within a fraction of a dB of the simulation results. For differential

detection the difference is larger, though, assuming a worst-case Doppler fading bandwidth of 0.05. It is felt that the results will be useful in evaluating the performance of TCM schemes over shadowed channels, and that the analysis enhances the understanding of this channel model.

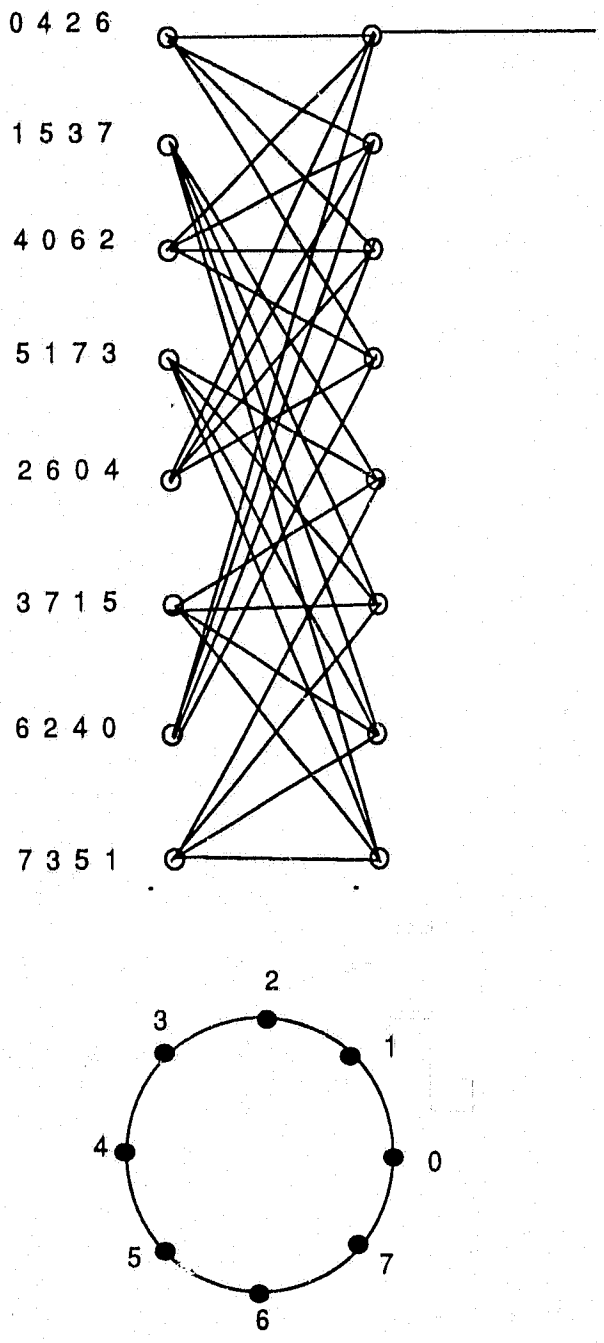

Figure 4.2: Trellis diagram for an 8-state, 8PSK TCM Scheme.

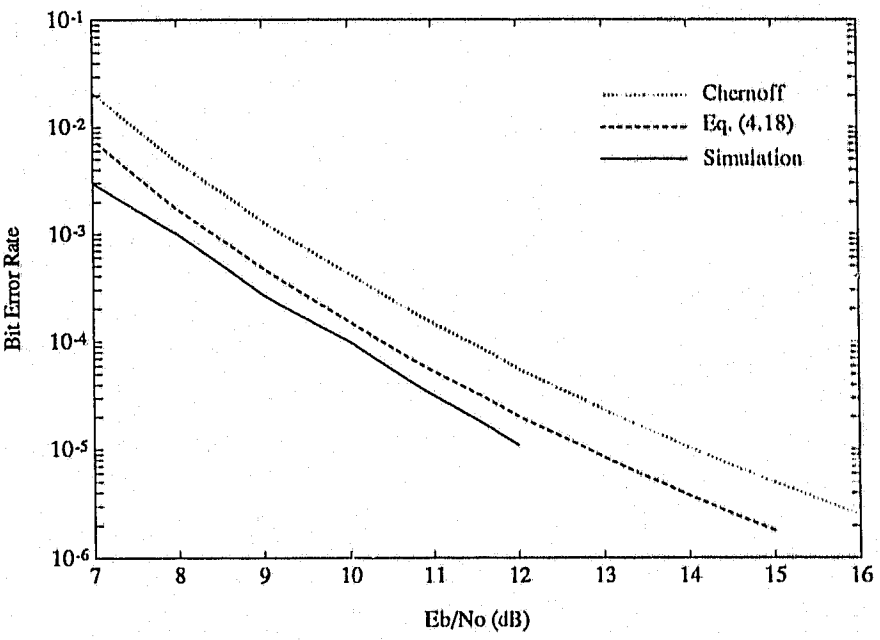

Figure 4.3: P_b versus $\overline{E}_b/N_0$. TC-8PSK, light shadowed Rician fading.

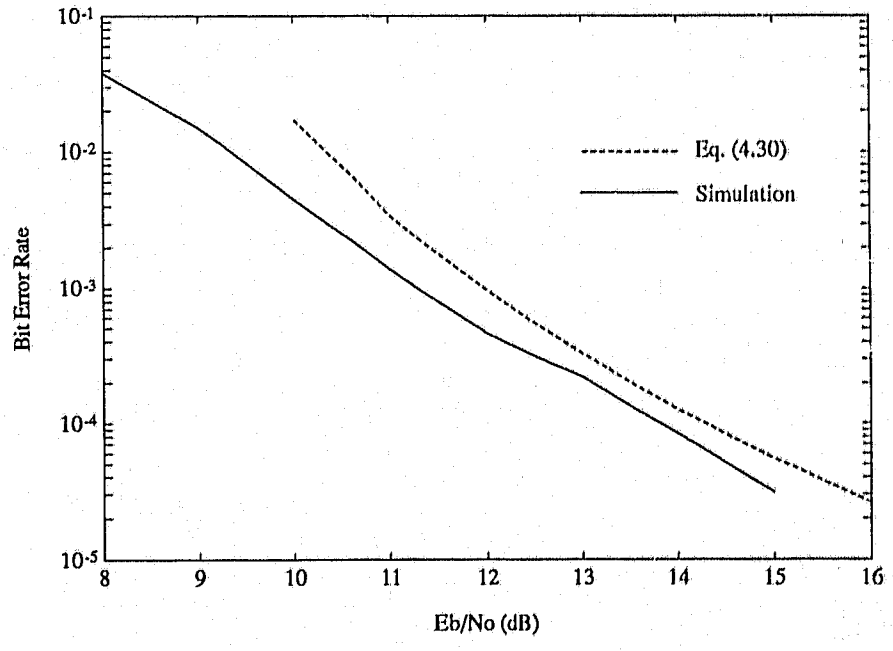

Figure 4.4: P_b versus $\overline{E}_b/N_0$. TC-8DPSK, light shadowed Rician fading, $f_D T_s = 0.05$.

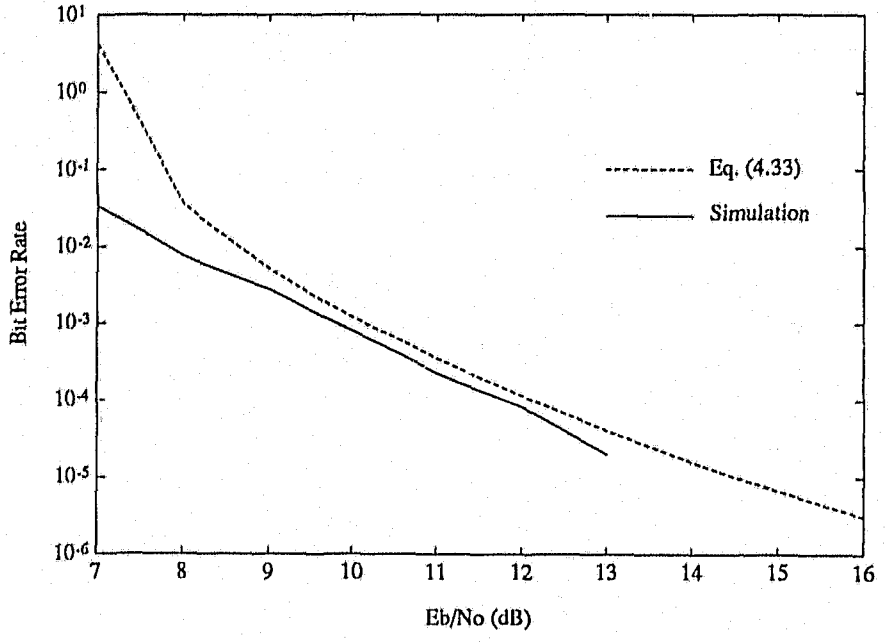

Figure 4.5: P_b versus $\overline{E}_b/N_0$. TC-PT-8PSK, light shadowed Rician fading, $f_D T_s = 0.05$.

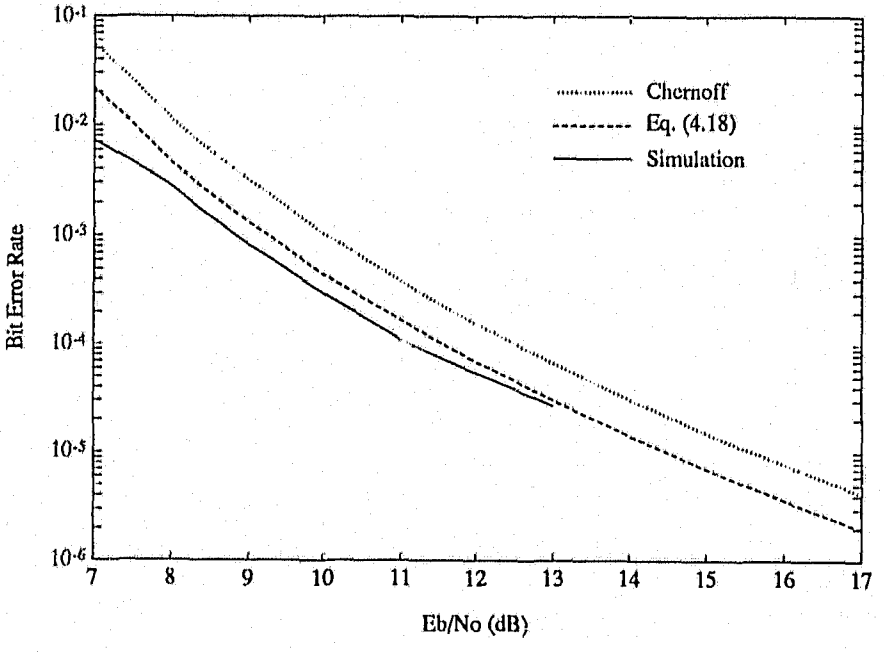

Figure 4.6: P_b versus $\overline{E}_b/N_0$. TC-8PSK, average shadowed Rician fading.

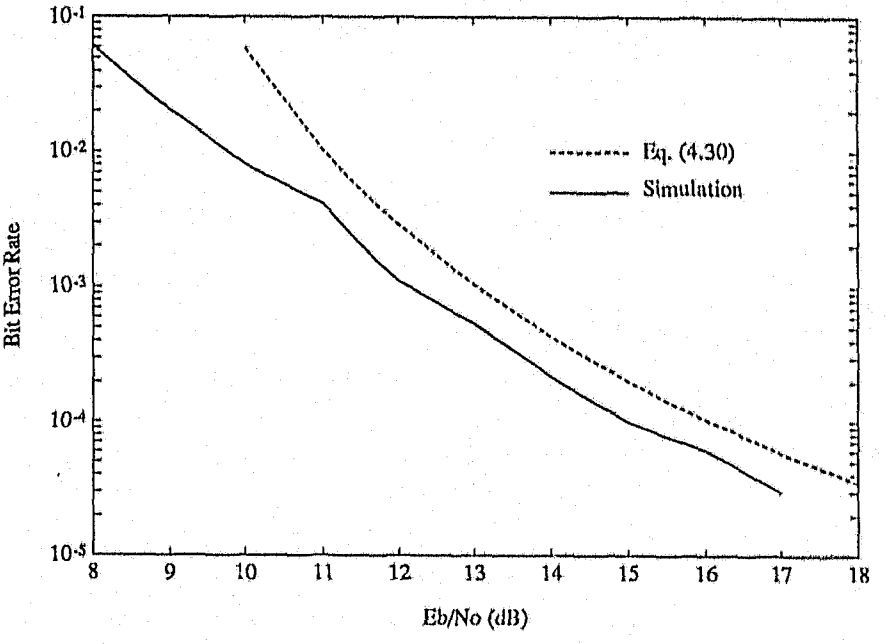

Figure 4.7: P_b versus $\overline{E}_b/N_0$. TC-8DPSK, average shadowed Rician fading, $f_D T_s = 0.05$.

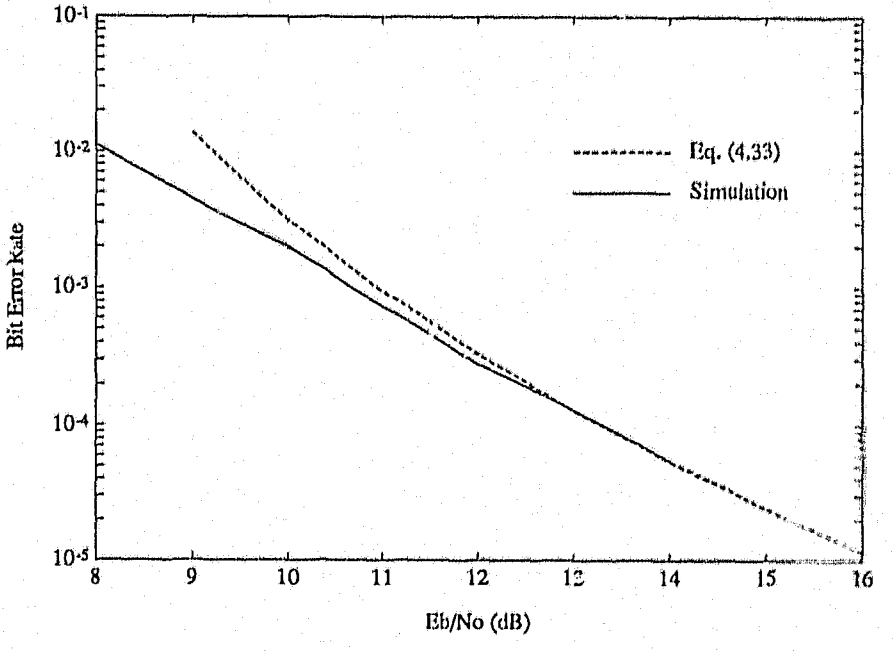

Figure 4.8: P_b versus $\overline{E}_b/N_0$. TC-PT-8PSK, average shadowed Rician fading, $f_D T_s = 0.05$.

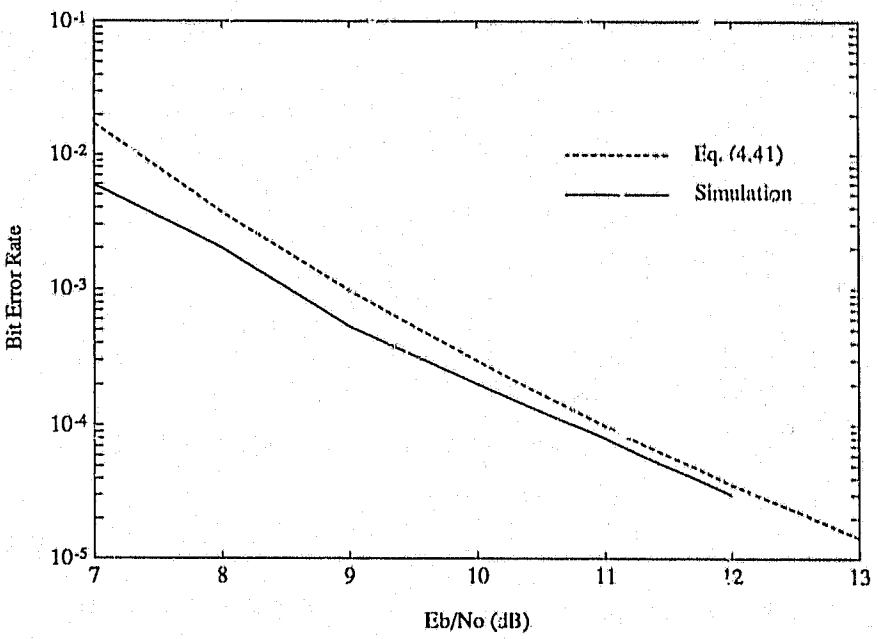

Figure 4.9: P_b versus $\overline{E}_b/N_0$. TC-8PSK, light shadowed Rician slow fading.

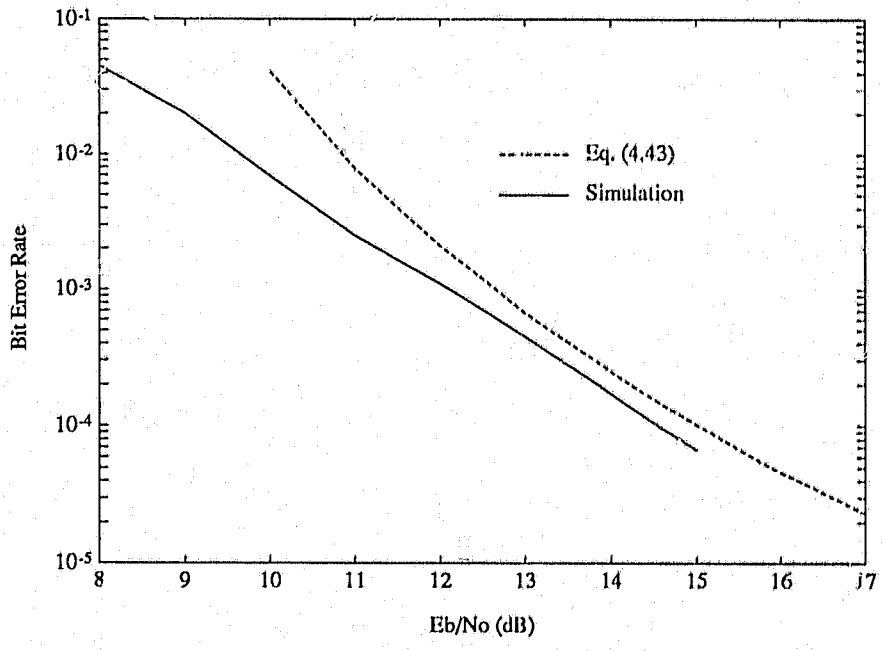

Figure 4.10: P_b versus $\overline{E}_b/N_0$. TC-8DPSK, light shadowed Rician slow fading, $f_D T_s = 0.05$.

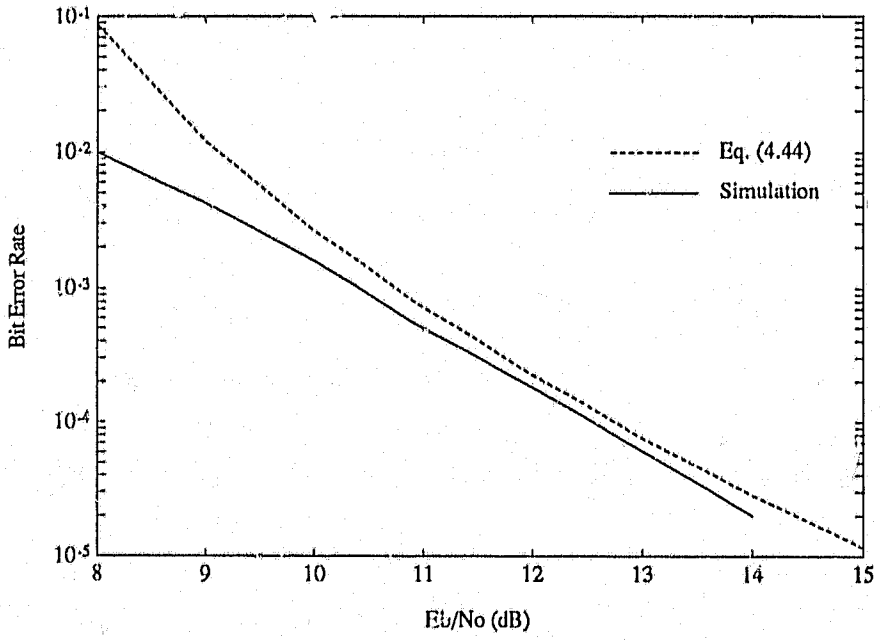

Figure 4.11: P_b versus $\overline{E}_b/N_0$. TC-PT-8PSK, light shadowed Rician, slow fading, $f_D T_s = 0.05$.

Chapter 5

Performance of TCM in Nonindependent Rician Fading

5.1 Introduction

In Chapters 3 and 4, the focus has been mainly on ideally interleaved channels, which results in independent fading. In this chapter an analysis of the performance of TCM schemes over *nonindependent* Rician fading channels is presented. As before, error bounds on the PEP based on the pilot-tone model are derived. In addition, for Rayleigh fading channels with an exponential auto-covariance function, bounds resembling those for memoryless channels are derived. Being substantially more accurate than Chernoff bounds, our bounds allow for accurate estimation of system performance when the assumption of ideal interleaving is relaxed.

The use of TCM (or most other coding techniques) generally requires interleaving in these systems to break up burst errors caused by amplitude fades. The duration of the fades, which can also be viewed as the channel memory, depends on the Doppler spread associated with fading process. Given an interleaver of size $N_d \times N_s$ (block interleaving), it was shown in Section 2.5 that as a result of interleaving/deinterleaving, the fading process is made to vary N_d times faster, from the receiver's perspective, than in a noninterleaved case; i.e., the effective channel memory is reduced by a factor of $1/N_d$. Accordingly, a channel is said to be *ideally interleaved* if $N_d \to \infty$ and *non-ideally interleaved* if N_d is finite.

In light of the foregoing, it is clear that the channel memory is reduced, but not eliminated with non-ideal interleaving. In this work, the effect of this residual memory on the error performance of TCM, measured in terms of the bit error probability P_b, is addressed. In particular, consideration is given to how large N_d should be in order that P_b approaches that of ideal interleaving. The key to the estimation of P_b is evaluation of the PEP, as we have seen in the previous chapters. Then, a union upper bound on P_b can be found using informationally weighted sum of PEP's for all possible error events. To compute the PEP of TCM schemes in fading channels, the probability that a quadratic decision variable (i.e., the difference between the two path metrics, assuming Viterbi decoding, of the two codewords) in complex normal variables is less than a certain threshold must be calculated. In general, this probability cannot be obtained in closed form, although the characteristic function of the decision variable is known in closed form.

An early and analogous example in this context is Pierce and Stein [57], who present an analysis of multiple-diversity performance (assuming maximal-ratio combining) for nonindependent fading among the signals. The PDF of the sum of the received powers is obtained in terms of the eigenvalues of the covariance matrix of signals from all the diversity branches. Because of the duality between diversity methods and coding, for instance, for binary convolutional codes the PEP can be obtained similarly. For this case, Gagnon and Haccoun [38, 58, 59] have derived several new upper bounds. Straightforward extension of the results in [38, 58] to the TCM case may not be fruitful in that the Chernoff derived therein is known to be weak when applied to TCM schemes [16].

For TCM on Rayleigh fading channels, the PEP can be expressed in terms of the eigenvalues of a weighted covariance matrix. In [16, 19] a method to compute the exact PEP for this case has been given; it involves evaluating residues. P_b is estimated by computing exact PEP's for a set of dominant error events. However, for Rician channels, computation of the exact PEP is possible only via numerical integration.

The performance analysis of convolutional coding schemes in non-ideally interleaved fading channels has been studied mostly through computer simulation in [42,60-63].

In this chapter, we present two new upper bounds on the PEP when non-ideal interleaving is employed in a Rician fading channel. The method requires computing eigenvalues, but avoids integration, and is significantly more accurate than a Chernoff bound for this case. As before, the bounds are derived assuming the pilot-tone concept, and hence can be modified to several useful cases including ideal coherent detection, coherent detection based on a pilot-tone and differential detection. P_b is estimated by suitably truncating a union bound, while for Rayleigh fading with an exponential auto-covariance function, the second bound can be simplified to a form resembling that of memoryless channels. Thus P_b can be bounded using the transfer function technique, based on the method of Zehavi and Wolf. Comparisons with simulation results show that the estimates of P_b are quite accurate when N_d is sufficiently large.

This chapter is organized as follows. Section 5.2 describes the system model used here and the characterisation of Rician fading channels. The bounds are derived in Section 5.3. Several examples are presented in Section 5.4. Finally, conclusions are provided in Section 5.5.

5.2 Performance Analysis

The system model under consideration is depicted in Figure 2.3 and explained in Section 2.3. The channel model and the received signal process are described in Section 2.4. In the following, we derive an upper bound on the PEP when non-ideal interleaving exists.

According to the pilot-tone concept, an estimate $\hat{\alpha}_k$ of the true channel gain α_k is obtained by processing samples of the pilot-tone which is transmitted along with the data. As in Section 3.3, we assume that $\hat{\alpha}_k$ is Gaussian with mean $\langle \hat{\alpha}_k \rangle$

and variance b_1. The normalized correlation coefficient between α_k and $\hat{\alpha}_k$ is μ.

For the case of implementation and analysis, we take the Viterbi decoder metric to be Euclidean, that is,

$$m(y_k, x_k) = -|y_k - \hat{\alpha}_k x_k|^2. \tag{5.1}$$

We remark that decoding with this decoding metric is not necessarily optimum for non-ideally interleaved channels. The optimum decoder metric would presumably take into account the residual correlations [29, Chap. 11].

The PEP $P(\mathbf{x} \rightarrow \hat{\mathbf{x}})$ is the probability of choosing the coded sequence $\hat{\mathbf{x}} = (\hat{x}_1, \hat{x}_2, \ldots, \hat{x}_N)$ when $\mathbf{x} = (x_1, x_2, \ldots, x_N)$ was transmitted, given only two choices. Let $\eta \triangleq \{k : x_k \neq \hat{x}_k\}$ and let L denote the number of elements in η. Later in this chapter, when we derive a simplified upper bound on the PEP, we will assume that the L elements of η are contiguous, that is, $\eta = \{k_0, k_0 + 1, \ldots, k_0 + L - 1\}$ for some k_0. Unlike binary convolutional codes, this assumption is true for most pairs of codewords in a TCM scheme and allows for a simple error bound. Since in an exponentially correlated fading channel, the correlations between any two channel gain terms increase as the time separation between two decreases, this assumption leads to a slightly pessimistic error bound.

The PEP, as in Chapter 3, can be expressed as

$$P(\mathbf{x} \rightarrow \hat{\mathbf{x}}) = \Pr\{\Xi \geq 0\} \tag{5.2}$$

where

$$\Xi = \sum_{k \in \eta} y_k \hat{\alpha}_k^* (\hat{x}_k - x_k)^* + y_k^* \hat{\alpha}_k (\hat{x}_k - x_k). \tag{5.3}$$

Let V_k denote the 2×1 column matrix

$$V_k = (\hat{\alpha}_k \;\; y_k)^T. \tag{5.4}$$

The decision variable Ξ can then be compactly represented as

$$\Xi = \sum_{k \in \eta} V_k^\dagger F_k V_k = \mathbf{V}^\dagger \mathbf{F} \mathbf{V} \tag{5.5}$$

where the dagger denotes conjugate transpose, and $\mathbf{V}$, $\mathbf{F}$ are given by

$$\mathbf{V} = \begin{pmatrix} V_1 \\ \vdots \\ V_L \end{pmatrix}, \quad \mathbf{F} = \begin{pmatrix} F_1 & \cdots & 0 \\ \vdots & \ddots & \vdots \\ 0 & \cdots & F_L \end{pmatrix} \tag{5.6}$$

with

$$F_k = \begin{pmatrix} 0 & (\hat{x}_k - x_k)^* \\ (\hat{x}_k - x_k) & 0 \end{pmatrix}. \tag{5.7}$$

From (2.8), (2.10) and (5.4), it follows that each V_i is Gaussian with the mean $\langle V \rangle = (A, Ax_k)^T$ and the 2×2 covariance matrix

$$R_k = \begin{pmatrix} b_1 & \mu\sqrt{b_0 b_1}x_k \\ \mu^*\sqrt{b_0 b_1}x_k^* & b_0 + \sigma^2 \end{pmatrix}. \tag{5.8}$$

We also need the covariance matrix $\mathbf{R}$ of the random vector $\mathbf{V}$, and $\mathbf{R}$ is defined as the $2L \times 2L$ matrix

$$\mathbf{R} = \frac{1}{2}\langle [\mathbf{V} - \langle \mathbf{V} \rangle]^* [\mathbf{V} - \langle \mathbf{V} \rangle]^T \rangle. \tag{5.9}$$

For ideally interleaved channels, this matrix will be tri-diagonal, consisting only of R_k terms as defined by (5.8). In order to see how $\mathbf{R}$ is obtained when non-ideal interleaving is employed, consider the case of ideal coherent detection where prior measurements provide perfect channel estimation for each symbol interval. Thus, $\hat{\alpha}_k = \alpha_k$, $b_1 = b_0$, and $\mu = 1$. Assuming, without loss of generality, that the all-zero symbol sequence is transmitted, R_k can be readily obtained. To find the remaining elements of $\mathbf{R}$, we note that $V_i = (\alpha_i, y_i)^T$ and that the covariance between V_i and V_j $(i \neq j,\ i, j = 1, 2, \ldots, L)$ is

$$\frac{1}{2}\langle (V_i - \langle V_i \rangle)(V_j - \langle V_j \rangle)^T \rangle = b_0 \begin{pmatrix} \rho(|i-j|) & \rho(|i-j|) \\ \rho(|i-j|) & \rho(|i-j|) \end{pmatrix} \tag{5.10}$$

where $\rho(\bullet)$ is given by Eq. (2.13). A similar approach can be taken for differential detection and pilot tone aided detection (Section 3.3.7).

5.2.1 The PEP

To upper bound the PEP in (5.2), we introduce the following lemma, which is a slight modification of a lemma derived in [64, App. 2].

Lemma 1 *Let U be a random function, $w_U(x)$ its pdf, and $\phi_U(\omega) \triangleq \overline{\exp(j\omega U)}$ its characteristic function. Then*

$$Pr[U \geq 0] < \frac{1}{2\pi} \int_{-\infty}^{\infty} \frac{|\phi_U(\alpha - j\beta)|}{\sqrt{\alpha^2 + \beta^2}}\, d\alpha, \quad \beta_0 > \beta > 0, \tag{5.11}$$

where β_0 is the boundary of the convergence region of the integral $\int_{-\infty}^{\infty} w_U(x) \exp(\beta x) dx$.

Proof: From [64]

$$\begin{aligned} Pr[U \geq 0] &= \frac{1}{2\pi} \int_{-\infty}^{\infty} \frac{\phi_U(\alpha - j\beta)}{\beta - j\alpha}\, d\alpha, \quad \beta_0 > \beta > 0. \qquad (5.12) \\ &= \left| \frac{1}{2\pi} \int_{-\infty}^{\infty} \frac{\phi_U(\alpha - j\beta)}{\beta - j\alpha}\, d\alpha \right| \end{aligned}$$

Since $|\int g\, d\alpha| \leq \int |g|\, d\alpha$, the lemma follows immediately. When using this lemma, one needs to know the value of β_0, which, as will be seen next, depends on the largest positive eigenvalue of $\mathbf{R}^*\mathbf{F}$. For ideally interleaved channels β_0 can be found easily.

Now the characteristic function of Ξ (5.3) is given by

$$G_\Xi(\xi) = \prod_{k=1}^{2L} \frac{1}{1 - 2j\xi\phi_k} \exp\left[\frac{j\xi\phi_k |\langle \eta_k \rangle|^2}{1 - 2j\xi\phi_k}\right]. \tag{5.13}$$

where ϕ_k, $k = 1, 2, \ldots, 2L$ are the eigenvalues of $\mathbf{R}^*\mathbf{F}$. Note that $\mathbf{R}^*$ has positive eigenvalues, but due to the structure of $\mathbf{F}$ the matrix $\mathbf{R}^*\mathbf{F}$ has L positive eigenvalues and L negative ones. Thus, let $\phi_k < 0$ for $k = 1, 2, \ldots, L$ and $\phi_k > 0$ for $k = L+1, \ldots, 2L$. To obtain this form of the characteristic function, the set of

random variables V_k must be transformed to another set of $2L$ independent variables, where the transformation simultaneously diagonalizes both $\mathbf{R}$ and $\mathbf{F}$. The η_k's are the means of the transformed variables. Details of this transformation are given in Appendix A.

To apply (5.11) to bound the PEP in (5.2), one needs the range of β, which is related to the positive poles of $G_{\Xi}(\xi)$. Since β must be less than the minimum pole on the right hand plane, the range of β is

$$0 < \beta < \left[\frac{1}{2\phi_{max}}\right] \tag{5.14}$$

where ϕ_{max} denotes the largest positive eigenvalue, i.e., $\max(\phi_k |\ k = L+1, \ldots, 2L)$. Having established the range of β, we combine (5.2), (5.11) and (5.13) to obtain

$$P(\mathbf{x} \to \hat{\mathbf{x}}) < \frac{1}{2\pi} \int_{-\infty}^{\infty} \frac{1}{\sqrt{\alpha^2 + \beta^2}} \prod_{k=1}^{2L} \frac{\exp(v_k)}{\sqrt{(1-2\beta\phi_k)^2 + 4\phi_k^2\alpha^2}}\, d\alpha \tag{5.15}$$

where

$$v_k = \text{Real}\left(\frac{(\beta + j\alpha)\phi_k |\langle \eta_k \rangle|^2}{1 - 2\beta\phi_k - 2j\alpha\phi_k}\right). \tag{5.16}$$

It can be readily shown that

$$v_k \le \frac{\beta\phi_k |\langle \eta_k \rangle|^2}{1 - 2\beta\phi_k}. \tag{5.17}$$

Thus we have

$$P(\mathbf{x} \to \hat{\mathbf{x}}) < \frac{1}{2\pi} \int_{-\infty}^{\infty} \frac{1}{\sqrt{\alpha^2 + \beta^2}} \prod_{k=1}^{2L} \frac{\exp\left(\frac{\beta\phi_k |\langle \eta_k \rangle|^2}{1 - 2\beta\phi_k}\right)}{\sqrt{(1-2\beta\phi_k)^2 + 4\phi_k^2\alpha^2}}\, d\alpha. \tag{5.18}$$

In principle, we need to find the β which minimizes this upper bound, a quite difficult task. Instead, we may choose

$$\beta = \frac{1}{2}\left[\frac{1}{2\phi_{max}}\right] \tag{5.19}$$

and evaluate (5.18) numerically, which again is computationally intensive. Dividing each square root in the product by $4\phi_k^2$, (5.18) can be recast as

$$P(\mathbf{x} \rightarrow \hat{\mathbf{x}}) < \Lambda(\beta) \frac{\exp\left[\beta \langle V \rangle^{\dagger} (\mathbf{F}^{-1} - 2\beta \mathbf{R}^*)^{-1} \langle V \rangle\right]}{|\det(2\mathbf{R}^*\mathbf{F})|} \tag{5.20}$$

where

$$\Lambda(\beta) \triangleq \frac{1}{2\pi} \int_{-\infty}^{\infty} \prod_{k=0}^{2L} \frac{1}{\sqrt{(\alpha^2 + \beta_k^2)}}\, d\alpha \tag{5.21}$$

and where $\beta_0 = \beta$, $\beta_k = |(1/2\phi_k - \beta)|$ for $k = 1, 2, \ldots, 2L$. Rather than numerically integrating, this integral can be bounded by applying Schwarz's inequality (for real positive functions $x(t)$ and $y(t)$, $\int x(t)y(t)\,dt \leq (\int x^2(t)\,dt \int y^2(t)\,dt)^{1/2}$). Define

$$\psi_1(\alpha) \triangleq \prod_{k=0}^{L} \frac{1}{\sqrt{\alpha^2 + \beta_k^2}},\ \psi_2(\alpha) \triangleq \prod_{k=L+1}^{2L} \frac{1}{\sqrt{\alpha^2 + \beta_k^2}}. \tag{5.22}$$

Schwarz's inequality yields the following:

$$\Lambda(\beta) \leq \frac{1}{2\pi} \left(\int_{-\infty}^{\infty} \psi_1^2(\alpha)\, d\alpha \int_{-\infty}^{\infty} \psi_2^2(\alpha)\, d\alpha \right)^{1/2}. \tag{5.23}$$

Now each integral can be evaluated by considering the complex integral $\oint f(z)\,dz$ in a semi-circular shaped contour. The details of this technique can be found in many text books on complex analysis. Thus we have

$$\Lambda(\beta) < \frac{1}{2} \left(\sum_{k=0}^{L} \frac{1}{\beta_k} \prod_{\substack{i=0 \\ i \neq k}}^{L} \frac{1}{(\beta_i^2 - \beta_k^2)} \right)^{1/2} \left(\sum_{k=L+1}^{2L} \frac{1}{\beta_k} \prod_{\substack{i=L+1 \\ i \neq k}}^{2L} \frac{1}{(\beta_i^2 - \beta_k^2)} \right)^{1/2}. \tag{5.24}$$

In deriving this, it is tacitly assumed that the β_k's ($k = 1, 2, \ldots, 2L$) are distinct. This is indeed the case for non-ideal interleaving. However, depending on the structure of the error event, with ideal interleaving, there may exist repeated eigenvalues. In this case (5.24) must be modified accordingly.

Combining (5.20) and (5.24), we get

$$P(\mathbf{x} \to \hat{\mathbf{x}}) < \Lambda(\beta_0, \beta_1, \ldots, \beta_{2L}) \frac{\exp\left[\beta \langle V \rangle^\dagger (\mathbf{F}^{-1} - 2\beta \mathbf{R}^*)^{-1} \langle V \rangle\right]}{|\det(2\mathbf{R}^*\mathbf{F})|} \tag{5.25}$$

where $\Lambda(\beta_0, \beta_1, \ldots, \beta_{2L})$ is the upper bound on $\Lambda(\beta)$, as defined by (5.24). It will be shown later that this upper bound is extremely accurate, and remains so even when no interleaving is employed. Additional accuracy gained by searching for the β that minimizes this bound may not warrant the additional computational complexity, and for this reason the choice (5.19) will be adequate.

Note that this bound can be readily used with a union bound to get an upper bound of the bit error probability:

$$P_b \leq \frac{1}{n} \sum_{j=1}^{\infty} w(j) P_j(\mathbf{x} \to \hat{\mathbf{x}}) \tag{5.26}$$

where $w(j)$ is the number of bit errors associated with the j-th error event, and n is the number of information bits per encoding interval. Obviously, in order to limit computations, this summation must be terminated after a finite number of error events, assuming that the remainder is negligible. As observed in [38], for sufficiently large γ_s and $N_d f_D T_s$, the union bound is dominated by a small set of error events. However, for low values of γ_s and $N_d f_D T_s$, the union bound itself becomes loose [38].

5.2.2 Simplified Error Bound

Referring back to (5.18), given the choice $\beta = 1/4\phi_{max}$ note that $(1 - 2\beta\phi_k)^2 \geq 4\beta^2\phi_k^2$ for $k = 1, 2, \ldots, 2L$. Thus we get

$$P(\mathbf{x} \to \hat{\mathbf{x}}) < \Lambda_1(\beta) \frac{\exp\left[\beta \langle V \rangle^\dagger (\mathbf{F}^{-1} - 2\beta \mathbf{R}^*)^{-1} \langle V \rangle\right]}{|\det(2\mathbf{R}^*\mathbf{F})|} \tag{5.27}$$

where

$$\Lambda_1(\beta) = \frac{1}{2\pi}\int_{-\infty}^{\infty} \frac{1}{(\alpha^2+\beta^2)^{L+1/2}}\,d\alpha \le \frac{1}{\beta^{2L}}\sqrt{\frac{C_{L-1}^{2L-2}C_L^{2L}}{2^{4L}}} \tag{5.28}$$

where C_k^n is a binomial coefficient. Once again this bound on the integral has been obtained by applying Schwarz's inequality. Combining these two we get

$$P(\mathbf{x}\to\hat{\mathbf{x}}) < B(L)(4\phi_{max})^{2L}\frac{\exp\left[\beta\langle V\rangle^\dagger(\mathbf{F}^{-1}-2\beta\mathbf{R}^*)^{-1}\langle V\rangle\right]}{|\det(2\mathbf{R}^*\mathbf{F})|} \tag{5.29}$$

where

$$B(L) \triangleq \sqrt{\frac{C_{L-1}^{2L-2}C_L^{2L}}{2^{4L}}}. \tag{5.30}$$

While simpler than (5.25), this bound is substantially weaker in the case of limited interleaving with slow fading. The reason is that in deriving this bound the terms $1-2\beta\phi_k$ in the denominator of (5.18) have been neglected (cf. (5.21), (5.28)).

5.2.3 Rayleigh Fading Channels

We would like to further simplify (5.29) to a product form that can be used in conjunction with the transfer function technique. This may not be done in the case of Rician fading. For Rayleigh fading channels, however, the exponential term in (5.29) is zero, and this enables us to bound the other terms. For this purpose, we assume an exponential auto-covariance function (see Eq. (2.13)).

If the maximum eigenvalue ϕ_{max} can be bounded by a number that is independent of the structure of an error event, then (5.29) can be further simplified. This is possible for ideal interleaving, as the eigenvalues of $\mathbf{R}^*\mathbf{F}$ can be determined by considering each 2×2 matrix product $\mathbf{R}_k^*\mathbf{F}_k$. Let ϕ_{k-} and ϕ_{k+} denote these two eigenvalues. Assuming μ to be real and using Eqs. (5.7) and (5.8), it can be

readily proven that all positive ϕ_{k+} satisfy the inequality

$$\phi_{k+} < \frac{((1-\mu^2)b_0+\sigma^2)}{\mu\sqrt{b_0/b_1}}. \tag{5.31}$$

It is conjectured that this bound on the ϕ_{max} also holds for the case of non-ideal interleaving. In other words, it is conjectured that the largest positive eigenvalue of $\mathbf{R}^*\mathbf{F}$ does not increase above the value given in (5.31) when q changes from $q = 0$ to $q > 0$. This can be proven for error events of length two (see Appendix D). In fact, all entries that contain q will be off the main diagonal of $\mathbf{R}^*\mathbf{F}$, which suggests that for small q values the eigenvalues change very little. We have observed this numerically. Thus, from 5.19, the choice of β is

$$\beta = \frac{\mu\sqrt{b_0/b_1}}{4((1-\mu^2)b_0+\sigma^2)}. \tag{5.32}$$

Clearly, the bound (5.31), and hence (5.32), will be most accurate when the interleaving capacity is nearly ideal, otherwise (for slow fading and low or no interleaving capacity, $q \approx 1$) it will be substantially weaker. This behaviour will be considered later.

To further simplify (5.29), we also need the determinant of $\mathbf{R}$, given in Appendix B. Combining (5.27), (5.32) and (E.1.7), we get

$$P(\mathbf{x} \to \hat{\mathbf{x}}) < \tilde{B}(L) \prod_{k=1}^{L} \frac{1}{4\beta^2\Gamma|x_k - \hat{x}_k|^2} \tag{5.33}$$

where

$$\Gamma = (b_1 - b_0q^2)(b_0 + b_1 + \sigma^2 - 2\mu\sqrt{b_0b_1}) - (b_1^2 - 2\mu b_1\sqrt{b_0b_1} + \mu^2 b_0 b_1) \tag{5.34}$$

and

$$\tilde{B}(L) \triangleq B(L)\frac{\Gamma^2}{b_1^2((1-\mu^2)b_0+\sigma^2)^2 - (b_0q)^2(b_0+b_1-2\mu\sqrt{b_0b_1}+\sigma^2)^2}. \tag{5.35}$$

So the bound on the bit error probability is

$$P_b \leq \frac{\tilde{B}(L_{min})}{n} \sum_{j=1}^{\infty} w(j) \prod_{k=1}^{L} \frac{1}{4\beta^2 \Gamma |x_k - \hat{x}_k|^2}. \tag{5.36}$$

Next we specialise this bound to several cases.

Ideally Interleaved Rayleigh Channels

In this case $q = 0$ and (5.36) simplifies to

$$P_b \leq \frac{\tilde{B}(L_{min})}{n} \sum_{j=1}^{\infty} w(j) \prod_{k=1}^{L} \frac{4(1 + (1-\mu^2)\gamma_s)}{\mu^2 \gamma_s |x_k - \hat{x}_k|^2}. \tag{5.37}$$

This is the familiar Chernoff bound, with an additional multiplying factor. For codes with $L_{min} = 2$, this factor tightens the ordinary Chernoff bound by about 3.3 dB in terms of signal-to-noise ratio, γ_s. This result is similar to the one derived by Chan and Bateman [17].

Ideal TC-MPSK

In this case it is assumed that prior measurements provide perfect channel estimation for each symbol interval. Thus, $\hat{\alpha}_k = \alpha_k$, $b_1 = b_0$=0.5, and $\mu = 1$. Then β would be (5.32)

$$\beta = \frac{\overline{E}_s}{2N_0}. \tag{5.38}$$

Substituting these values in (5.34) and (5.35) results in the following:

$$P(\mathbf{x} \to \hat{\mathbf{x}}) < \tilde{B}(L) \prod_{k=1}^{L} \frac{1}{(1-q^2)\frac{\gamma_s}{4}|x_k - \hat{x}_k|^2} \tag{5.39}$$

which when substituted in (5.36) yields

$$P_b \leq \frac{\tilde{B}(L_{min})}{n} \sum_{j=1}^{\infty} w(j) \prod_{k=1}^{L} \frac{1}{(1-q^2)\frac{\gamma_s}{4}|x_k - \hat{x}_k|^2}. \tag{5.40}$$

In comparison to ideal interleaving, the signal-to-noise ratio degradation due to non-ideal interleaving will be

$$\Theta = 10 \log (1 - q^2). \tag{5.41}$$

For example, when the product $N_d f_D T_s$ increases from 0.01 to 0.2 the loss decreases from 9 dB to 0.3 dB. We may conclude that $N_d f_D T_s \approx 0.2$ is practically equivalent to ideal interleaving.

TC-MDPSK

In this case, for any signalling period, the preceding signal provides the channel estimate. Hence, $b_1 = b_0 + \sigma^2$ and, assuming an exponential auto-covariance function, it follows that

$$\mu^2 = \frac{b_0 \exp -(4\pi f_D T_s)}{b_0 + 0.5\gamma_s^{-1}} = \frac{\zeta^2}{1 + \gamma_s^{-1}}. \tag{5.42}$$

These values can be readily substituted in (5.32), (5.34), (5.35) and (5.36) to get the following upper bound on P_b:

$$P_b \leq \frac{B(L_{min})}{n} \sum_{j=1}^{\infty} w(j) \prod_{k=1}^{L} \frac{4((1+\gamma_s^{-1})^2 - \zeta^2)^2}{(2(1+\gamma_s^{-1} - q^2)(1+\gamma_s^{-1} - \zeta) - (1+\gamma_s^{-1} - \zeta)^2)\zeta^2 |x_k - \hat{x_k}|^2}. \tag{5.43}$$

For ideal interleaving, $q = 0$, and this reduces to [6, 9.119]. Also, since $\zeta < 1$, P_b will not decrease to zero when $\gamma_s \to \infty$, giving rise to an error floor.

TC-PT-MPSK

As an alternative to differential detection, the α_k's may be measured by transmitting a reference pilot tone along side the data signal. Assuming ideal filtering at the receiver, it can be shown (Section 3.3.5) that pilot-estimate of the true channel gain will be

$$\hat{\alpha}_k = \alpha_k + \varsigma_k \tag{5.44}$$

where ς_k is an additive noise term with a variance of $0.5(B_pT_s)(\frac{1+r}{r})\gamma_s^{-1}$, in which B_p is the bandwidth of the pilot tone filter, r is the power ratio between the pilot signal and the data signal, and γ_s is the signal-to-noise ratio (including the power consumed by the pilot signal). It was shown in Section 3.3.5 that

$$var(\hat{\alpha}_k) = b_1 = 0.5 + 0.5\,(B_pT_s)\left(\frac{1+r}{r}\right)\gamma_s^{-1}, \tag{5.45}$$

$$|\mu|^2 = \frac{1}{1 + (B_pT_s)\left(\frac{1+r}{r}\right)\gamma_s^{-1}}.$$

Substituting these values in (5.32), (5.34), (5.35) and (5.36) results in the following:

$$P_b \leq \frac{\tilde{B}(L_{min})}{n}\sum_{j=1}^{\infty} w(j)\prod_{k=1}^{L}\frac{4(\Delta+\sigma^2(1+\Delta))^2}{((1+\Delta-q^2)(\Delta+\sigma^2)-\Delta^2)|x_k-\hat{x}_k|^2} \tag{5.46}$$

where $\Delta \triangleq B_pT_s(\frac{1+r}{r})\gamma_s^{-1}$ and $\sigma^2 = (1+r)\gamma_s^{-1}$. We note that for ideal TC-MPSK $\Delta = 0$ and $r = 0$, and this simplifies to (5.40).

5.3 Results

For several pertinent cases, the performance of the trellis code shown in Fig. 2 has been analyzed by using the error bounds developed earlier. To assess the accuracy of the error bounds, computer simulations have also been conducted. For simulation results, the interleaving span, N_s, was chosen to be 18 symbols.

To compute P_b given in (5.26), following [19], a set of error events have been picked from the modified error state diagram of this trellis code, as defined by Zehavi and Wolf [65]. Here the set includes 14 dominant error events given in [19, Table 1] as well as 50 error events whose span is equal to 4. These error events were found by searching through the error state diagram given in [41]. The details of the transfer function of this code can be found in [41].

Consider an error event of length two between the two codewords $\mathbf{x} = (1, 1, \ldots)$ and $\hat{\mathbf{x}} = (e^{j2\pi/4}, e^{j4\pi/4}, \ldots)$. For a Rayleigh fading channel with normalized Doppler 0.01, Fig. (5.1) depicts the exact PEP and the upper bounds (5.25) and (5.29) as functions of the signal-to-noise ratio $\overline{E}_s/N_0$ and the interleaving depth N_d. The exact PEP is computed by using the residue method [19]. It is clear that the upper bound (5.25) is extremely accurate while the accuracy of (5.29) increases as N_d increases.

For Rician fading ($K = 5$ dB) with normalized Doppler 0.01, Fig. (5.2) shows the exact PEP and the upper bound (5.25) as functions of the signal-to-noise ratio $\overline{E}_s/N_0$ and the interleaving depth N_d. The exact PEP is computed by numerical integration of Eq. (5.13). It is seen that the upper bound (5.25) is very accurate for $P_b < 10^{-3}$. For instance, the difference between the two curves can be as small as 0.2 dB asymptotically. To put this in perspective, we note that the difference between the Chernoff upper bound and the exact result for this particular error event can be 3.6 dB [16]. It is also noted that the accuracy of the bound increases as (1) K decreases, (2) $\gamma_s \to \infty$ and (3) $N_d \to \infty$. This may be explained by noting that the bound ignores the phase function of the integrand in (5.13).

For the same error event, the upper bound is plotted as a function of the interleaving depth N_d in Fig. 5.3 for two auto-covariance functions: Bessel and exponential. For exponential model, when the interleaving depth is such that $N_d f_D T_s \approx 0.5$, beyond which any increase of interleaving capacity does not reduce the error probability. As a matter of fact, $N_d f_D T_s \approx 0.2$ appears to be sufficient in this case. For Bessel model, however, the error probability shows an oscillatory behaviour; consequently, the optimum interleaving depth for a given Doppler is now $N_d f_D T_s \approx \theta_i$ where $J_0(\theta_i) = 0$, $i = 1, 2, \ldots$ and $J_0(x)$ is the zero-order Bessel function. These conclusions hold for most error events, and thus the overall bit error probability would be affected in a similar manner.

For Rayleigh and Rician ($K = 5$ dB) fading with an exponential auto-covariance

function, the transfer function upper bounds, approximate P_b (see Eq. (5.26)), and simulation results are presented for the same trellis code in Figs. (5.4) and (5.5). Simulation results and the approximate P_b agree quite well even for the no-interleaving case. From Fig. (5.4), it can be seen that the transfer-function bound is quite accurate when interleaving depth and $\overline{E}_s/N_0$ are large. When no interleaving is employed, some of the simulation points are larger than the approximate P_b. This implies that more error events should be included in (5.26) or could be due to statistical error in the simulation. Also, an interleaving depth of 20 symbols, resulting in a total interleaver capacity of 360 8PSK symbols, achieves almost 6 dB energy gain over no interleaving.

The performance of pilot tone aided detection is shown in Figs. (5.6) and (5.7). Once again, the approximate P_b is quite accurate for $N_d = 20$, implying that this amounts to almost ideal interleaving.

Fig. (5.8) shows the case of differential detection. Unfortunately, for an exponential covariance model, the quality of the channel estimates degrades rapidly even for small Doppler rates (see (5.42)). This causes the bound (5.43) to be quite weak.

5.4 Summary

The error probability analysis of TCM in non-ideally interleaved Rayleigh channels has been analyzed by [19]. However, for general Rician channels, no comparable results exist in the literature. In this chapter, we have derived two general upper bounds for this case, which are significantly more accurate than a Chernoff bound. In addition, for Rayleigh fading channels with an exponential auto-covariance function, a bound resembling that for memoryless channels has been derived. since the bounds have been obtained assuming the pilot-tone concept, they can be modified to several useful cases. Comparing with simulation results shows that quite accurate estimates of P_b are obtainable with the use of these bounds.

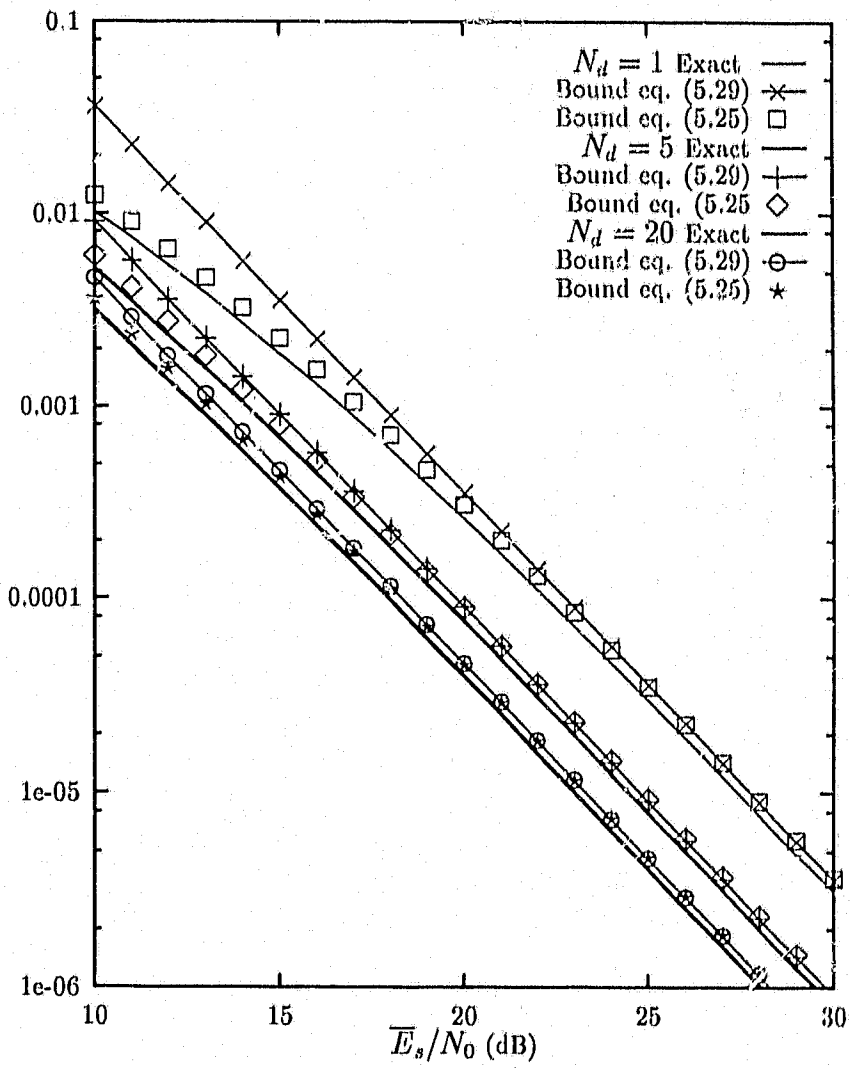

Figure 5.1: Exact PEP and the upper bound of an error event. TC-8PSK, Rayleigh fading, $f_D T_s = 0.01$ with exponential correlation.

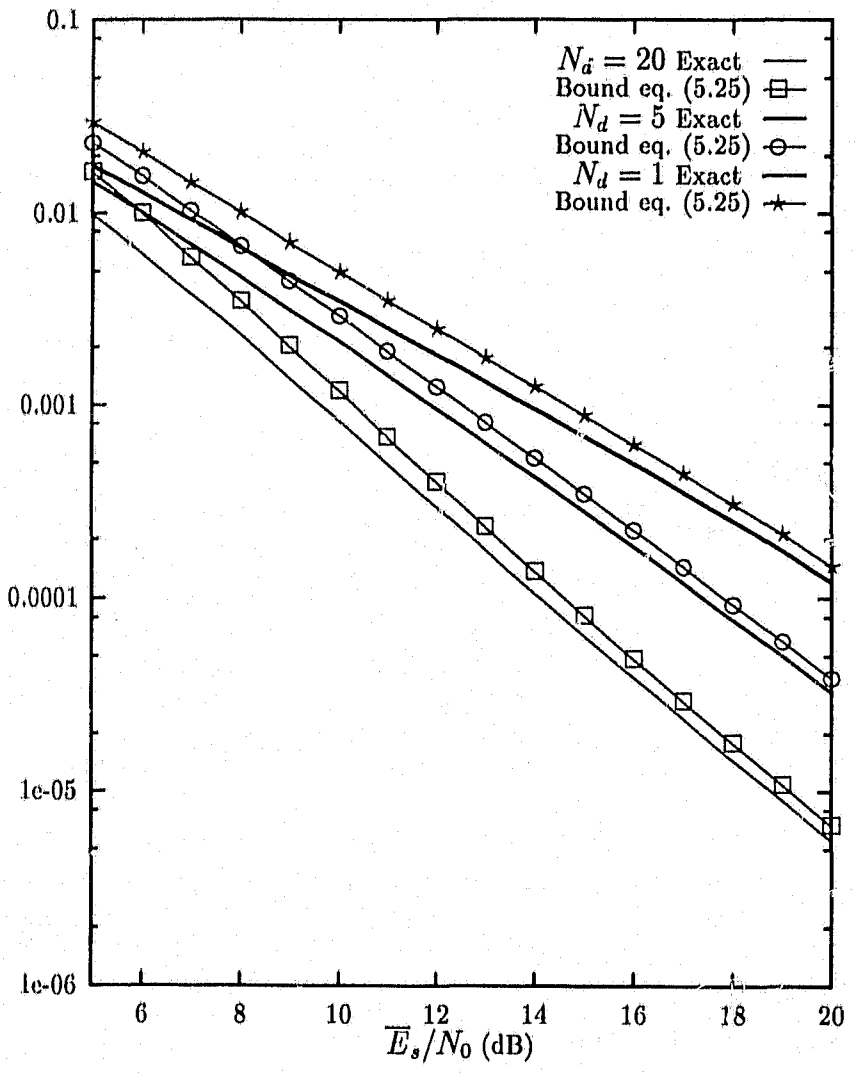

Figure 5.2: Exact PEP and the upper bound of an error event. TC-8PSK, Rician fading ($K = 5$ dB), $f_D T_s = 0.01$ with exponential correlation.

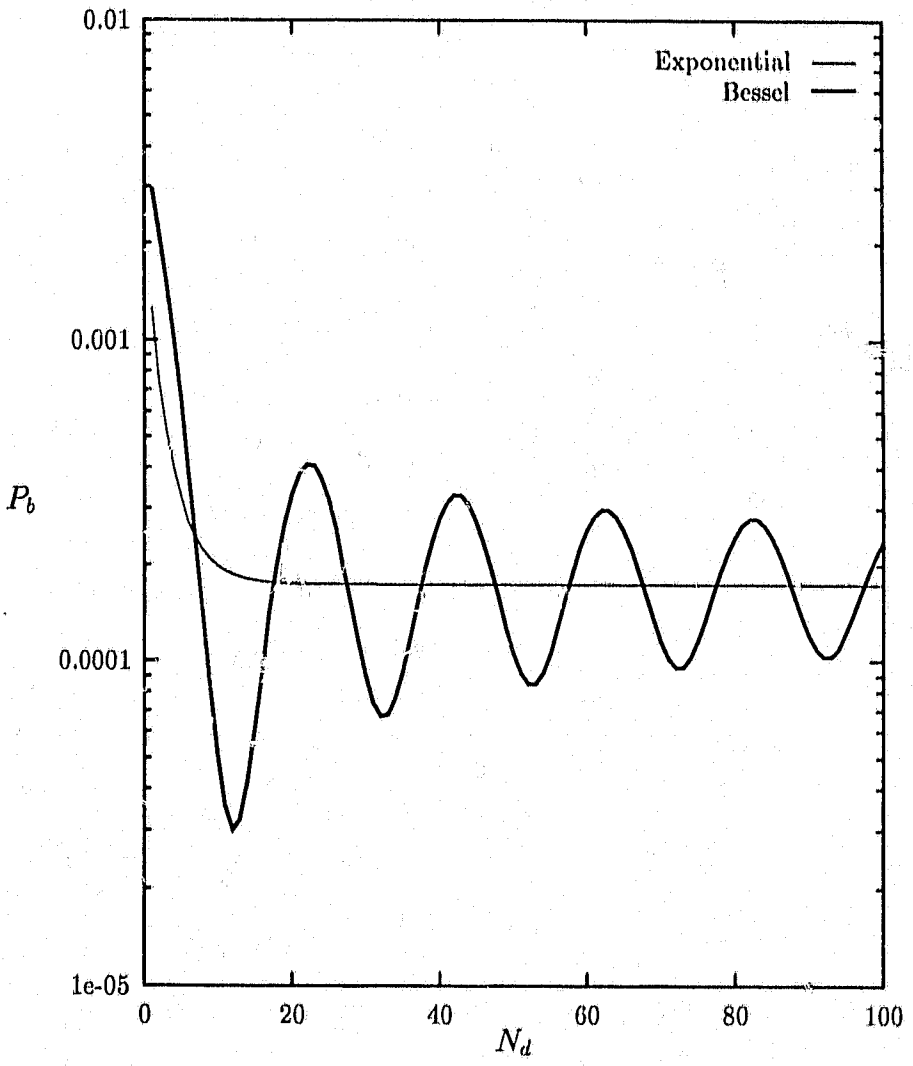

Figure 5.3: Upper bound on the PEP versus the interleaving depth. Rician fading ($K = 5$ dB). $\overline{E_b}/N_0$= 12.0 dB, $f_D T_s$=0.05.

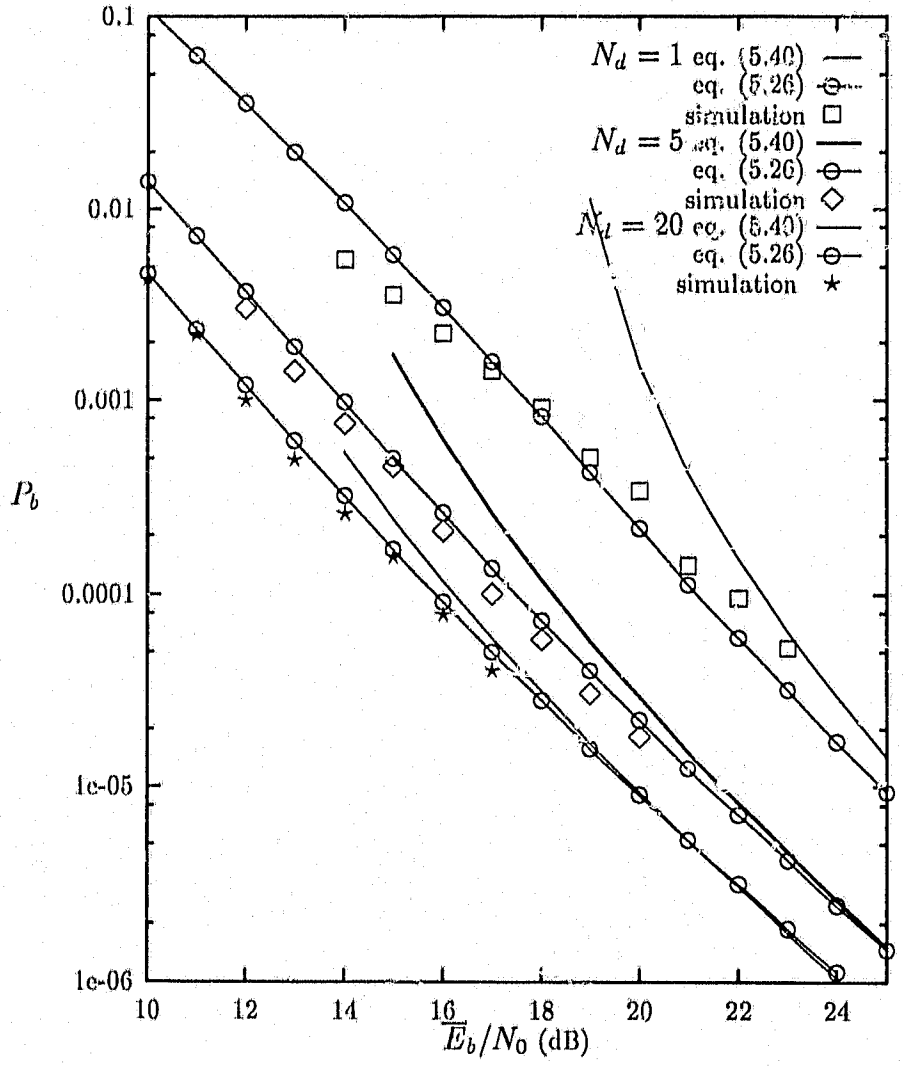

Figure 5.4: Simulation results, the approximate P_b and the transfer function bound (TFB). TC-8PSK, Rayleigh fading, $f_D T_s$=0.01 with exponential correlation.

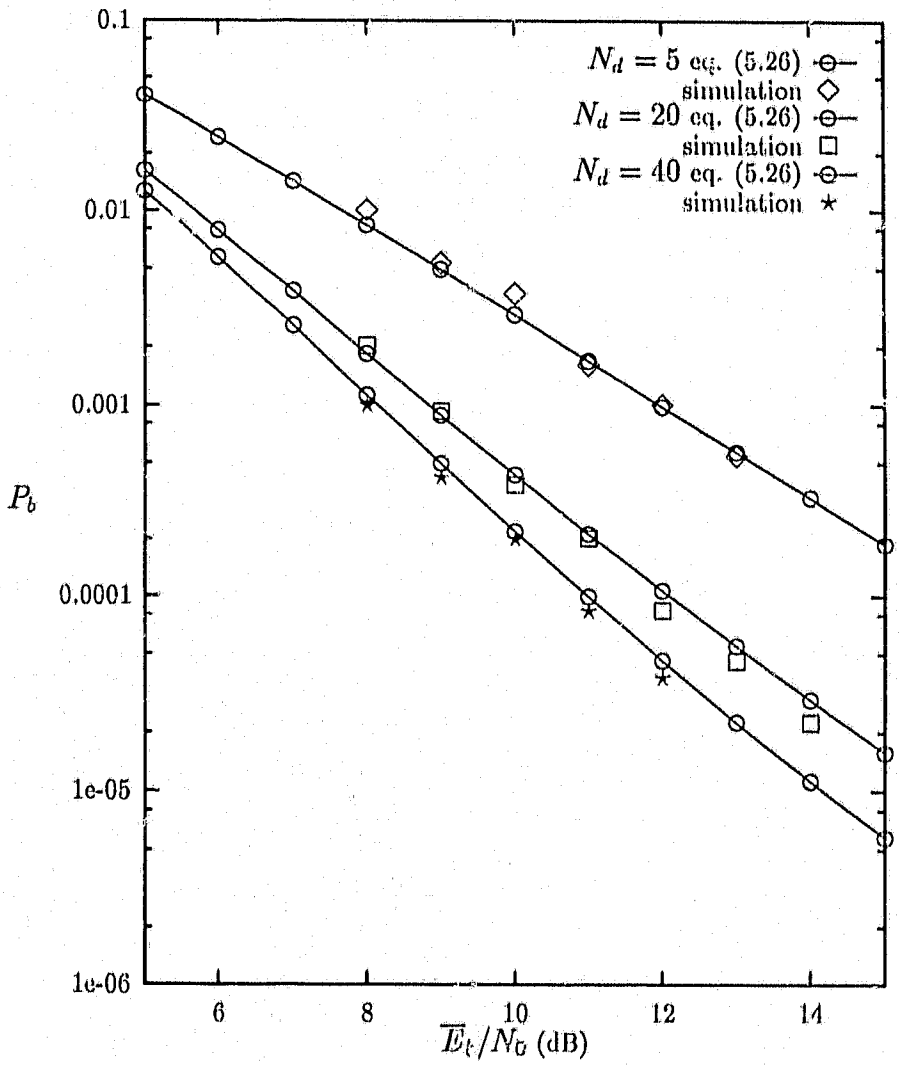

Figure 5.5: Simulation results and the approximate P_b. TC-8PSK Rician fading ($K = 5$ dB), $f_D T_s$=0.01 with exponential correlation.

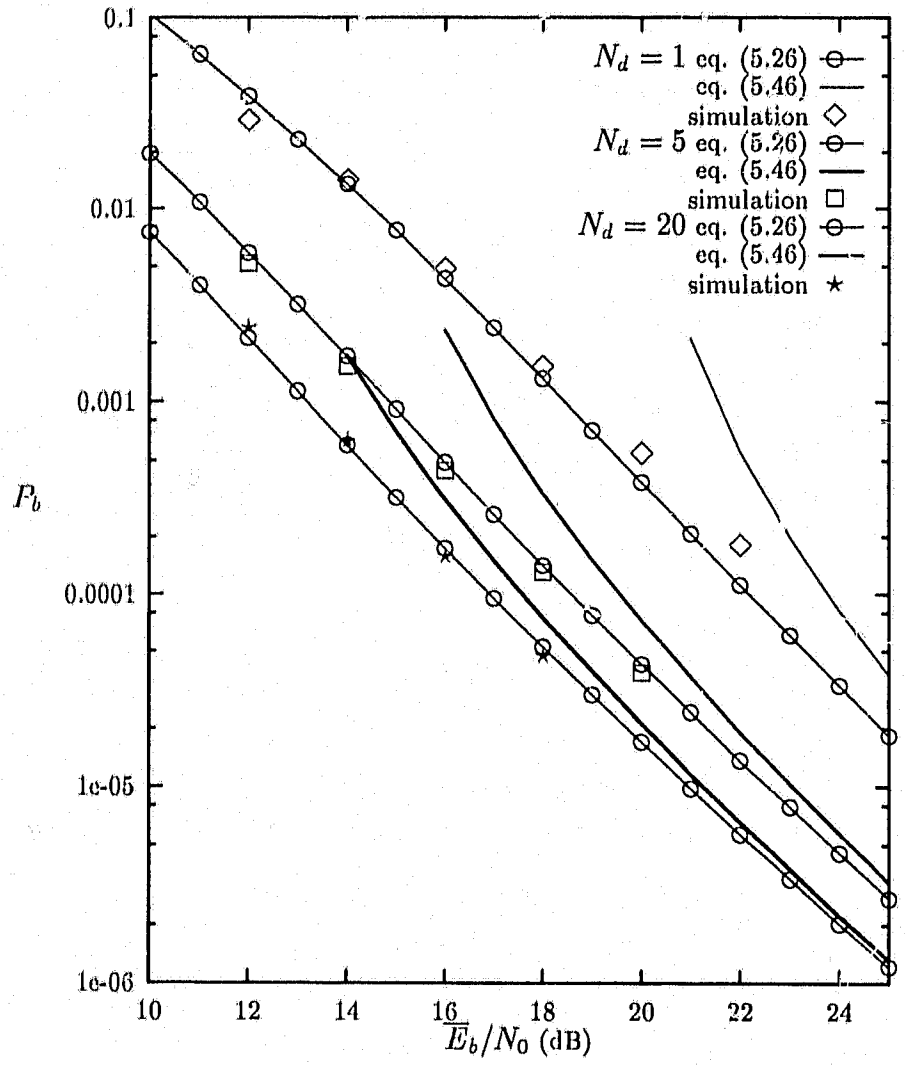

Figure 5.6: Simulation results, the approximate P_b and the TFB. TC-PT-8PSK, Rayleigh fading, $f_D T_s$=0.01 with exponential correlation.

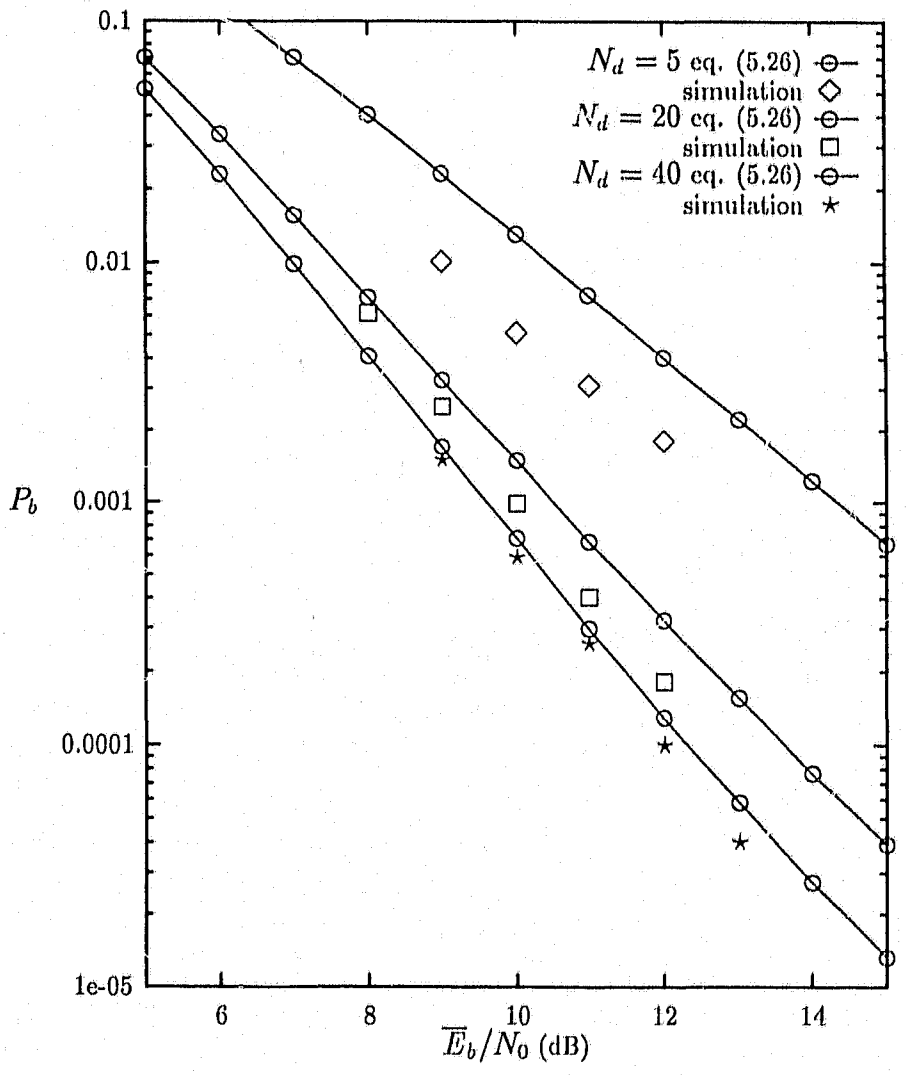

Figure 5.7: Simulation results and the approximate P_b. TC-PT-8PSK Rician fading ($K = 5$ dB), $f_D T_s$=0.01 with exponential correlation.

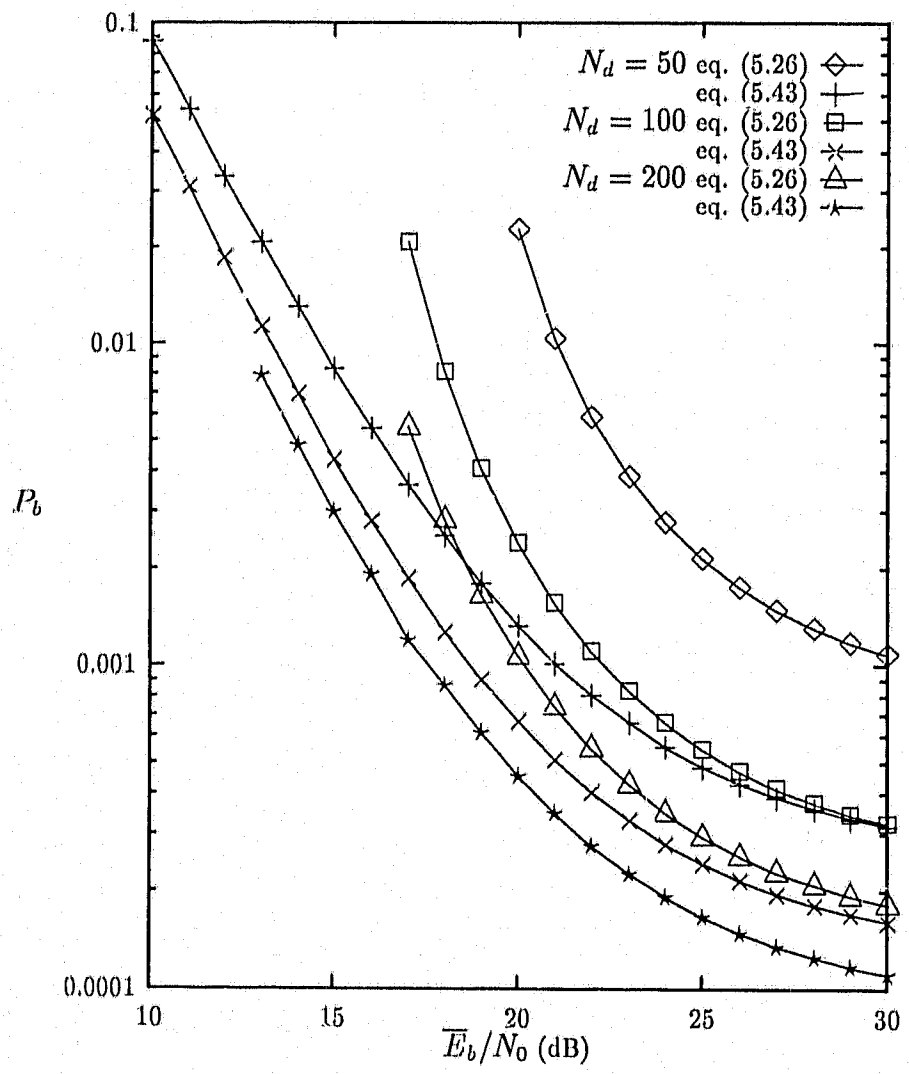

Figure 5.8: Simulation results and the approximate P_b. TC-8DPSK, Rayleigh fading, $f_D T_s$=0.001 with exponential correlation.

Chapter 6

Concatenated Coding and ARQ Systems in Rayleigh Fading

6.1 Introduction

TCM schemes can be employed in conjunction with concatenated coding or automatic-repeat-request (ARQ) systems. The performance of such hybrid schemes operating in fading channels is addressed in this chapter. For Rician fading channels, we can use the error bounds developed in Chapters 3 and 4 to estimate the performance of concatenated coding schemes. For Rayleigh fading channels, new approximate error expressions are developed when the decoding Viterbi algorithm is modified such that side information can be generated to erase symbols or request retransmission.

As determined by Shannon in his original work, arbitrarily small error rates can be achieved via the use of arbitrarily long codes. Shannon theory, however, does not offer constructive methods for finding such codes or practical algorithms for encoding and decoding them. Moreover, the complexity of encoding and decoding algorithms increases exponentially as the code length increases. To overcome these drawbacks, concatenated coding has been proposed [66]. Here two codes, known as the *inner* code and the *outer* code, are cascaded, thereby considerably reducing implementation complexity.

The concatenated coding scheme considered herein uses TCM codes for the

inner code and Reed-Solomon (RS) codes as the outer code. Because TCM can be readily decoded with a maximum likelihood algorithm (i.e., Viterbi decoding), the side information generated from this inner decoder can be used to determine whether the symbols passed onto the RS decoder are reliable.

Several features of RS codes make them suitable for use as outer codes. First, RS codes are maximum-distance separable, which implies the most efficient use of redundancy. Second, since RS codes are available over a wide range of block lengths, symbol sizes, and code rates, an optimum RS code may be found readily for any application. Third, efficient decoding algorithms that can accommodate both symbol errors and symbol erasures exist.

The idea of modifying the conventional Viterbi algorithm (VA) so as to generate reliability information has received attention recently. When decoding a received sequence, the conventional VA selects the path (codeword) that maximizes the log-likelihood function. The modified VA's given in [67-69] essentially amount to observing the metric difference between the best and the second best path in the trellis and erasing symbols if the difference is less than a certain threshold.

In the literature, several papers which use modified VA's have dealt with the problem of TCM in concatenated coding and ARQ systems. In [69], concatenated coding systems consisting of trellis inner codes and RS outer codes have been considered for AWGN channels; coding gains of 4-6 dB have been obtained for specific concatenations of TCM and RS codes. TCM-RS concatenated coding for fading channels has been investigated in [68], where the Chernoff bound approach is used to determine the performance of the inner code. In [70], the performance of TCM in conjunction with retransmission strategies for both AWGN and fading channels is addressed, but only the case of ideal channel state information is treated.

Since perfect coherent detection may be impossible to achieve in fading environments, incorporating a reference signal to the data signal in order to assist detection at the receiver becomes essential. Continuing the approach of previous chapters, here the pilot-tone model is used to derive the PEP expressions and era-

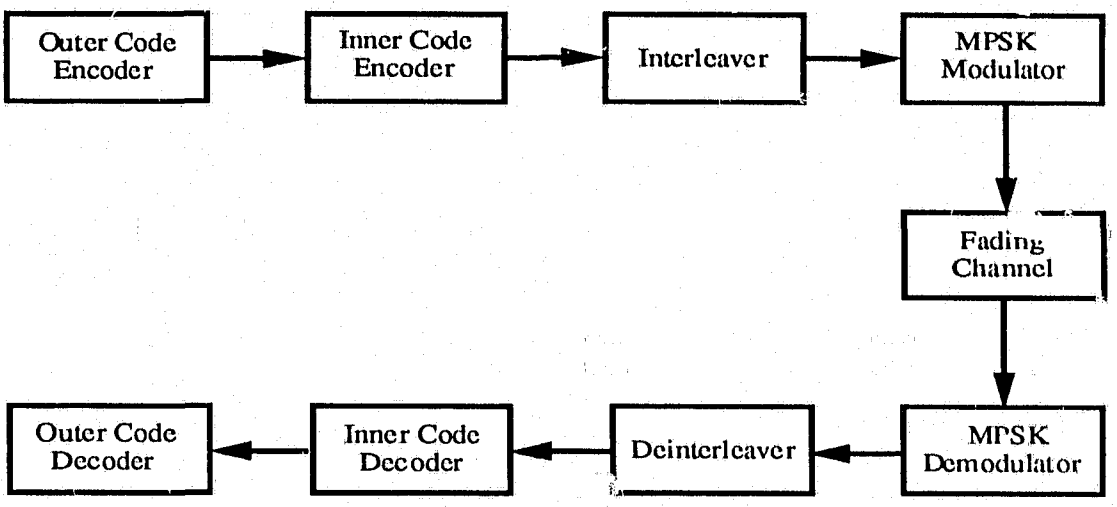

Figure 6.1: A Concatenated Coding System.

sure (or retransmission) probabilities when the modified VA is used for decoding, and when the inner channel is ideally interleaved. The case of limited interleaving for the inner channel is also analyzed. These results are used to study the effects of imperfect channel measurements, interleaving capacity, and the use of the modified VA on the performance of concatenated coding systems and ARQ systems.

This chapter is organized as follows. In Section 6.2 the concatenated coding system is described. The use of the conventional VA to decode the inner code is considered in Section 6.3. For Rayleigh fading channels, the use of a modified VA, capable of generating side information, is analyzed in Section 6.4 when ideal or partial interleaving capacity is used. In Section 6.5 the error expressions are used in concatenated coding systems and ARQ systems. Illustrative examples are given in Section 6.6, and the chapter concludes in Section 6.7.

6.2 System Description

The system under consideration is shown in Fig. 6.1. In this system, a trellis code with Viterbi decoding is used as the inner code along, and an (n_2, k_2) Reed-Solomon code with symbols from the Galois Field GF(2^l), where $n_2 = 2^l - 1$,

is used as the outer code. The trellis code is defined by k_1 encoder input bits per unit time and 2^{k_1+1}-ary PSK modulation. Binary input data is encoded by the outer encoder with $k_2 l$ information bits each being converted to an n_2-byte codeword. This codeword is symbol-interleaved and then further encoded by the trellis encoder. The fading channel is described in Chapter 2, and hence will not be detailed here. The received M-ary symbols are rearranged by the deinterleaver and decoded by the Viterbi decoder, and then passed onto the RS decoder. For the purposes of analysis, we assume that the outer channel is ideally interleaved; note that, however, this outer interleaver is not shown in Fig. 6.1. For the inner channel, however, we investigate the cases when the interleaving capacity used in the inner channel is finite or infinite. In the latter case, the fading channel is memoryless, while the former case is characterized by the normalized effective fading bandwidth, which, as explained in Section 2.5, equals the product $N_d f_D T_s$.

6.3 Conventional VA

When the conventional VA is used for decoding the inner code, the error expressions developed in Chapters 3 and 4 can be directly used to find the bit error rate at the output of the inner decoder.

If the bit error probability at the output of the inner decoder is P_b, then with ideal bit-interleaving the symbol error rate at the input of the outer decoder is

$$P_s = 1 - (1 - P_b)^l \tag{6.1}$$

where l is the number of bits in an RS symbol.

Since no erasure information is generated at the output of the Viterbi decoder, the RS decoder performs errors-only decoding. Let d_2 be the minimum Hamming distance of the (n_2, k_2) RS code. Then the maximum number of symbol errors that can be corrected (the error correcting capability) is given by

$$t_2 = \left\lfloor \frac{d_2 - 1}{2} \right\rfloor \tag{6.2}$$

where $\lfloor\ \rfloor$ designates the integer part. If the number of symbol errors in a codeword is greater that t_2, decoding fails. Assuming decoding symbol errors occur independently in RS decoding, the decoded block error probability is given by

$$P_{bl} \simeq \sum_{i=t_2+1}^{n_2} \binom{n_2}{i} P_s^i (1-P_s)^{n_2-i}. \tag{6.3}$$

Therefore, the decoded bit error probability is [69]

$$P_{bd} \approx \frac{d_2}{2n_2} P_{bl}. \tag{6.4}$$

In addition to the decoded bit error probability, another useful performance measure of a concatenated coding system is its coding gain defined by comparison to an uncoded system with the same overall information rate. It is clear from Section 6.2 that the overall information rate of the concatenated coding system is given by

$$\mathrm{R_{eff}} = \frac{k_1}{2}\frac{k_2}{n_2} \text{ bits/dimension.} \tag{6.5}$$

Consequently, an uncoded system with $(2^{2\mathrm{R_{eff}}})$-ary PSK modulation can be used as a reference to define the coding gain. For an AWGN channel, the bit error rate of this modulation can be expressed as [69]

$$P_b \simeq Q\left(\sqrt{\frac{\Delta_0^2 \mathrm{R_{eff}} E_b}{N_0}}\right) \tag{6.6}$$

where $Q(\bullet)$ is the area under the standardized Gaussian tail, and

$$\Delta_0^2 \triangleq 2 - 2\cos\left(2\pi/2^{2\mathrm{R_{eff}}}\right). \tag{6.7}$$

In a Rician fading channel, E_b is a random variable, and hence Eq. (6.6) must be averaged over this distribution. By modifying [6, Eq. (9.1)], we have

$$P(E_b) = \frac{(1+K)}{\overline{E}_b} \exp\left\{-K - E_b\frac{(1+K)}{\overline{E}_b}\right\} I_0\left(2\sqrt{E_b K\frac{(1+K)}{\overline{E}_b}}\right) \tag{6.8}$$

where K is the Rician constant, $\overline{E}_b$ is the average bit energy, and $I_0(\bullet)$ is the modified Bessel function of zero order. The required average can be obtained via a result derived in [71]; hence,

$$P_b \simeq Q(u,v) - \frac{1}{2}\left[1+\sqrt{\frac{d}{1+d}}\right]\exp\left(-\frac{u^2+w^2}{2}\right)I_0(uw) \tag{6.9}$$

where $Q(\bullet,\bullet)$ is the Marcum Q-function,

$$d = \frac{\Delta_0^2 \mathrm{R}_{\mathrm{eff}}}{2(1+K)}\frac{\overline{E}_b}{N_0}, \tag{6.10}$$

and

$$\begin{bmatrix} u \\ w \end{bmatrix} = \sqrt{\frac{K\left(1+2d \mp 2\sqrt{d(1+d)}\right)}{2(1+d)}}. \tag{6.11}$$

By comparing Eqs. (6.4) and (6.9) the concatenated coding gain may be estimated.

6.4 Modified VA

In this section, we consider a modified VA, which generates side information to be used by the outer decoder. For simplicity, we investigate only the Rayleigh channel. In the following, the pilot-tone model is used to derive expressions for the asymptotic PEP and erasure probability as a function of the threshold. In addition, a method to compute the optimum easure threshold is derived.

In order to derive the side (erasure) information the following algorithm can be utilized [67-69]. Consider the codeword $\mathbf{x} = (x_1, x_2, \ldots, x_N)$ and another codeword $\hat{\mathbf{x}} = (\hat{x}_1, \hat{x}_2, \ldots, \hat{x}_N)$. Let $\mathbf{y} = (y_1, y_2, \ldots, y_N)$ be the corresponding received vector. As discussed in Chapter 3, the inner decoder computes the path metrics $M_{\mathbf{x}}$ and $M_{\hat{\mathbf{x}}}$ for these two codewords. This computation, however, is done iteratively. At each step, the modified VA compares the metrics of all paths entering each state,

selects the path with the largest metric (called the survivor), and labels the survivor with $\mathcal{C}$ or $\mathcal{X}$. As a result, this modified VA requires that the survivor, its metric, and its label be stored for each state. Suppose that the inner trellis code has $\mathcal{S}$ states and encodes k_1 bits per unit time. Select an $\mathcal{R}$ such that $2^{k_1\mathcal{R}} \leq \mathcal{S} < 2^{k_1(\mathcal{R}+1)}$. At the beginning of the decoding ($i = 0, \ldots, \mathcal{R}$), all paths in the trellis are labelled as $\mathcal{C}$. At each next step i, ($i = \mathcal{R}+1, \mathcal{R}+2, \ldots$), for each state, the decoder selects the paths $\mathbf{x}_i$ and $\hat{\mathbf{x}}_i$ that have the largest and second largest metrics, $M_{\mathbf{x}_i}$ and $M_{\hat{\mathbf{x}}_i}$, respectively. Assume that the path $\mathbf{x}_{i-1}$ has label $\mathcal{C}$ at level $i-1$. If

$$M_{\mathbf{x}_i} - M_{\hat{\mathbf{x}}_i} > T \tag{6.12}$$

where T is an erasure threshold, then $\mathbf{x}_i$ survives with label $\mathcal{C}$; otherwise, path $\mathbf{x}_i$ survives with label $\mathcal{X}$. If the path $\mathbf{x}_{i-1}$ has label $\mathcal{X}$ at level $i-1$, then $\mathbf{x}_i$ always survives with label $\mathcal{X}$. This test is carried out for all the $\mathcal{S}$ states at each time step i. An erasure occurs at some level i if all survivors are labelled with $\mathcal{X}$, in which case, for the concatenated coding system, the inner decoder attaches erasure flags to symbols back to the time unit $i-D$ where D denotes the code decision length.

Let $\mathbf{x}$ be the transmitted code. Then, the PEP, the probability $\hat{\mathbf{x}}$ survives as a reliable path (i.e., with a label $\mathcal{C}$), is

$$P(\mathbf{x} \to \hat{\mathbf{x}}) = \Pr\left\{\sum_{k=1}^{N} |y_k - \beta\hat{\alpha}_k x_k|^2 - \sum_{k=1}^{N} |y_k - \beta\hat{\alpha}_k\hat{x}_k|^2 \gtrless T\right\}. \tag{6.13}$$

Define

$$\Xi = \sum_{k\in\eta} |y_k - \beta\hat{\alpha}_k\hat{x}_k|^2 - |y_k - \beta\hat{\alpha}_k x_k|^2 \tag{6.14}$$

where $\eta = \{k | x_k \neq \hat{x}_k, k = 1, \ldots, N\}$, and the definitions of $y_k, \beta, \hat{\alpha}_k$ can be found in Eq. (2.8) and Section (3.3). When the inner channel is ideally interleaved, the above sum consists of independent random variables, and the residue method given in [16] can be used to compute Eq. (6.13).

Ideally Interleaved Inner Channel

In this case, the characteristic function of Ξ follows from [16, Eq. (18)], where it is shown that

$$\phi_{\Xi}(s) = \left(\prod_{k \in \eta} \frac{1 + (1 - |\mu|^2)\gamma_s}{|\mu|^2 |x_k - \hat{x}_k|^2 \gamma_s} \right) \prod_{k \in \eta} \frac{-1}{(s - v_{1k})(s - v_{2k})} \tag{6.15}$$

where μ is correlation coefficient between α_k and $\hat{\alpha}_k$, $w_k = 1/2$,

$$\begin{bmatrix} v_{1k} \\ v_{2k} \end{bmatrix} = w_k \pm \sqrt{w_k^2 - d_k}, \tag{6.16}$$

and

$$d_k = -\frac{1 + (1 - |\mu|^2)\gamma_s}{|\mu|^2 |x_k - \hat{x}_k|^2 \gamma_s}. \tag{6.17}$$

In Eq. (6.15), the convergence region in the complex plane is given by $v_{2i} < \text{Real}(s) < v_{1k}$.

The exact PEP in Eq. (6.13) can be readily computed by the method given in [16], which involves summing up all residues at the right-plane poles of the Laplace transform of cumulative PDF of the random variable Ξ. That is,

$$P(\mathbf{x} \to \hat{\mathbf{x}}) = -\sum_{k \in \eta} \underset{s = v_{1k}}{\text{Residue}} \left[\frac{e^{-sT} \phi_{\Xi}(s)}{s} \right]. \tag{6.18}$$

Calculating this for each error event is time consuming. Alternatively, we derive an easy-to-compute, asymptotic expression for $P(\mathbf{x} \to \hat{\mathbf{x}})$. When $\mu \simeq 1$ and $\gamma_s \to \infty$, from Eqs. (6.16) and (6.17) we have

$$\begin{bmatrix} v_{1k} \\ v_{2k} \end{bmatrix} \simeq \begin{bmatrix} 1 \\ 0 \end{bmatrix}. \tag{6.19}$$

Substituting these values in Eqs. (6.15) and (6.18) results in

$$P(\mathbf{x} \to \hat{\mathbf{x}}) \simeq - \underset{s=1}{\text{Residue}} \left[\frac{(-1)^L e^{-sT}}{4^L s^{L+1} (s-1)^L} \left(\prod_{k \in \eta} \frac{1 + (1 - |\mu|^2)\gamma_s}{|\mu|^2 |x_k - \hat{x}_k|^2 \gamma_s / 4} \right) \right] \tag{6.20}$$

where L is the Hamming distance associated with this error event. By evaluating the L-th order residue at $s = 1$, we get

$$P(\mathbf{x} \to \hat{\mathbf{x}}) \simeq \psi(L, T) \left(\prod_{k \in \eta} \frac{1 + (1 - |\mu|^2)\gamma_s}{|\mu|^2 |x_k - \hat{x}_k|^2 \gamma_s / 4} \right) \tag{6.21}$$

where

$$\psi(L, T) \triangleq 4^{-L} e^{-T} \sum_{r=0}^{L-1} \frac{(L + r)!}{r! L! (L - 1 - r)!} T^{L-1-r}. \tag{6.22}$$

Suppose the j-th error event is between the codewords $\mathbf{x}_j = (x_{j1}, x_{j2}, \ldots, x_{jN_j})$ and $\hat{\mathbf{x}}_j = (\hat{x}_{j1}, \hat{x}_{j2}, \ldots, \hat{x}_{jN_j})$. Using the union bound technique and the above expression for the PEP, the bit error probability at the output of the inner decoder could be bounded by

$$P_b \leq \frac{1}{k_1} \sum_{j=1}^{\infty} m_j \psi(L_j, T) \left(\prod_{k \in \eta_j} \frac{1 + (1 - |\mu|^2)\gamma_s}{|\mu|^2 |x_{jk} - \hat{x}_{jk}|^2 \gamma_s / 4} \right) \tag{6.23}$$

where m_j is the number of information bit errors associated with the j-th error event, L_j is the Hamming distance of the j-th error event, and η_j is defined as $\{k | x_{jk} \neq \hat{x}_{jk},\ k = 1, \ldots, N_j\}$. This bound can be readily specialized to the following: for ideal coherent detection $\mu = 1$, for differential detection μ is given by Eq. (3.33), and for pilot-aided detection μ is given by Eq. (3.37).

Partially Interleaved Inner Channel

When interleaving is not ideal, Eq. (6.15) no longer holds since the distinct terms in Ξ (6.14) are correlated. Therefore, the characteristic function of Ξ can be expressed as

$$\phi_{\Xi}(s) = \prod_{i=1}^{2L} \frac{1}{1 + s\phi_i} \tag{6.24}$$

where the ϕ_i's are the eigenvalues of $2\mathbf{R}^*\mathbf{F}$ defined in Eqs. (3.12) and (3.14). In general, the ϕ_i's are non-zero unless the fading is very slow (i.e., $N_d f_D T_s \approx 0$). Of these eigenvalues, half are positive and half negative. Let $\phi_i < 0$ for $i = 1, \ldots, L$. Then the PEP is given by

$$P(\mathbf{x} \to \hat{\mathbf{x}}) = -\sum_{i=1}^{L} \operatorname*{Residue}_{s=-1/\phi_i} \frac{1}{s} \prod_{i=1}^{2L} \frac{e^{-sT/(2L)}}{1 + s\phi_i}. \tag{6.25}$$

To estimate P_b, the PEP's should be computed for enough error events and should be included in a union bound (c.f. (6.23)).

6.4.1 Erasure Probability

Ideally Interleaved Inner Channel

As before, denote by $\mathbf{x}$ the transmitted codeword. Let the decoder select $\hat{\mathbf{x}}$ as the correct one. An erasure event can be divided into two parts. First, the decoder makes the correct choice (i.e., $\hat{\mathbf{x}} = \mathbf{x}$) and, yet, sets up an erasure flag. Second, the decoder makes an error (i.e., $\hat{\mathbf{x}} \neq \mathbf{x}$) and sets up an erasure flag. Thus, the erasure event probability can be obtained as [70]

$$P(\text{erasure}) = P(\text{erasure}|\hat{\mathbf{x}} = \mathbf{x})P(\hat{\mathbf{x}} = \mathbf{x}) + P(\text{erasure}|\hat{\mathbf{x}} \neq \mathbf{x})P(\hat{\mathbf{x}} \neq \mathbf{x}). \tag{6.26}$$

Based on the erasure generating rule in (6.12), the event $(\text{erasure}|\hat{\mathbf{x}} = \mathbf{x})$ occurs when there exists another codeword $\tilde{\mathbf{x}} = (\tilde{x}_1, \tilde{x}_2, \ldots, \tilde{x}_N)$ which, when compared with $\hat{\mathbf{x}}$, causes the erasure. This probability is equal to

$$P(\text{erasure}|\mathbf{x} = \hat{\mathbf{x}}) = \Pr\left\{\sum_{k=1}^{N} |y_k - \beta\hat{\alpha}_k\tilde{x}_k|^2 - \sum_{k=1}^{N} |y_k - \beta\hat{\alpha}_k\hat{x}_k|^2 < T\right\}, \tag{6.27}$$

which can be evaluated as outlined earlier (e.g., Eq. (6.18)), but now the poles at the origin and in the left plane must be considered:

$$P(\text{erasure}|\mathbf{x} = \hat{\mathbf{x}}) = \operatorname*{Residue}_{s=0} \left[\frac{e^{sT}\phi_\Xi(s)}{s}\right] + \sum_{k\in\eta} \operatorname*{Residue}_{s=v_{2k}} \left[\frac{e^{sT}\phi_\Xi(s)}{s}\right]. \tag{6.28}$$

This can be approximated as outlined in Eq. (6.20). By evaluating the residue at $s = 0$, we have

$$P(\text{erasure}|\mathbf{x} = \hat{\mathbf{x}}) \simeq 4^{-L} \sum_{r=0}^{L} \frac{(L+r-1)!}{r!(L-1)!(L-r)!} T^{L-r} \left(\prod_{k \in \eta} \frac{1 + (1 - |\mu|^2)\gamma_s}{|\mu|^2 |x_k - \hat{x}_k|^2 \gamma_s / 4} \right). \tag{6.29}$$

The remaining terms in Eq. (6.26) can be bounded as follows. The correct decoding probability $P(\hat{\mathbf{x}} = \mathbf{x}) \leq 1$, and $P(\text{erasure}|\hat{\mathbf{x}} \neq \mathbf{x}) \leq 1$. The pairwise error probability $P(\hat{\mathbf{x}} \neq \mathbf{x})$ is obtained by setting $T = 0$ in (6.21). Therefore, Eq. (6.26) can be recast as

$$P(\text{erasure}) \leq \psi_1(L, T) \left(\prod_{k \in \eta} \frac{1 + (1 - |\mu|^2)\gamma_s}{|\mu|^2 |x_k - \hat{x}_k|^2 \gamma_s / 4} \right) \tag{6.30}$$

where

$$\psi_1(L, T) \triangleq 4^{-L} \left[\frac{(2L-1)!}{(L-1)!(L-1)!} + \sum_{r=0}^{L} \frac{(L+r-1)!}{r!(L-1)!(L-r)!} T^{L-r} \right]. \tag{6.31}$$

Using union bound arguments, the first event erasure probability at the output of the inner decoder is

$$P_{ef} \leq \sum_{j=1}^{\infty} \psi_1(L_j, T) \left(\prod_{k \in \eta_j} \frac{1 + (1 - |\mu|^2)\gamma_s}{|\mu|^2 |x_{jk} - \hat{x}_{jk}|^2 \gamma_s / 4} \right). \tag{6.32}$$

As noted earlier, the first erasure event causes the inner decoder to attach flags to the symbols delivered to the RS decoder. Approximately, the symbol erasure probability at the input to the outer decoder is (for $D \ll i$)

$$P_e \approx \frac{i - D}{i} P_{ef} \approx P_{ef}. \tag{6.33}$$

Partially Interleaved Inner Channel

Following the discussion in Section 6.25, the erasure probability in Eq. (6.28), in the case of a partially interleaved inner channel, can be evaluated as

$$P(\mathbf{x} \rightarrow \hat{\mathbf{x}}) = 1 + \sum_{i=L}^{2L} \underset{s=-1/\phi_i}{\text{Residue}} \frac{1}{s} \prod_{i=1}^{2L} \frac{e^{-sT/(2L)}}{1 + s\phi_i}. \tag{6.34}$$

This could be used in (6.32) to find P_e.

6.4.2 Optimum Threshold

Let P_s and P_e be the symbol error probability and symbol erasure probability at the input of the outer decoder. We would like to find the erasure threshold T that minimizes the probability of not decoding correctly at the output of the outer decoder. Unfortunately, T is related to P_E the probability of not decoding correctly in a very complicated manner. Therefore, we use a method given by [72], where a Chernoff bound on the P_E is minimized instead.

Consider n_e symbol erasures and n_s symbol errors in a received codeword of the (n_2, k_2) RS code. Then, probability of incorrect decoding is

$$P_E = P(2n_s + n_e > n_2 - k_2), \tag{6.35}$$

or equivalently

$$P_E = P(\sum_{i=1}^{n_2} W_i > n_2 - k_2) \tag{6.36}$$

where $W_i = 2$ with probability P_s, $W_i = 1$ with probability P_e, and $W_i = 0$ otherwise. The Chernoff bound on P_E is given by

$$P_E \leq \min_{\lambda > 1} \lambda^{-(n_2 - k_2)} \prod_{i=1}^{n_2} E\left[\lambda^{W_i}\right] \tag{6.37}$$

which, by assuming independent symbol erasures and errors, can be readily obtained as

$$P_E \leq \min_{\lambda>1} \lambda^{-(n_2-k_2)}[\lambda^2 P_s + \lambda P_e + (1 - P_s - P_e)]^{n_2}. \tag{6.38}$$

By differentiating the right hand side of this expression with respect to λ, we find that the upper bound is minimized when

$$\lambda = \frac{-k_2 P_e + \sqrt{k_2^2 P_e^2 + 4(n_2^2 - k_2^2)P_s(1 - P_e - Ps)}}{2(n_2 + k_2)P_s}, \tag{6.39}$$

provided that

$$1 - k_2/n_2 > P_e + 2P_s. \tag{6.40}$$

6.4.3 Erasures and Errors

In this case the inner decoder output symbols can contain both erasures and errors. The maximum number of erasures that can be allowed within a codeword is given by

$$T_{es} \leq d_2 - 1. \tag{6.41}$$

Let i and j designate, respectively, the number of symbol erasures and the number of symbol errors in a codeword of the (n_2, k_2) RS code. If $i > T_{es}$, the outer decoder will erase the entire codeword. Otherwise, the decoder is capable of correcting the received codeword if $i \leq T_{es}$ and $j \leq t(i)$ where

$$t(i) = \left\lfloor \frac{d_2 - i - 1}{2} \right\rfloor. \tag{6.42}$$

The probability of block error can be upper bounded by [69]

$$P_{bo} \leq \sum_{i=0}^{T_{es}} \binom{n_2}{i} P_e^i \sum_{j=d_2-i-t(i)}^{n_2-i} \binom{n_2 - i}{j} P_s^j (1 - P_s - P_e)^{n_2-i-j}, \tag{6.43}$$

which is related to the decoded bit error probability as [68]

$$P_{bd} = 1 - (1 - P_{bo})^{\frac{1}{n_2}}. \tag{6.44}$$

6.5 ARQ Systems

In [70], the authors analyze the performance of trellis coded hybrid automatic-repeat-request (TCM-HARQ) protocols in AWGN and fading channels. They make use of side information provided by the Viterbi decoder to generate retransmission requests. Here, we extend the results of [70] to include differential and pilot tone modulation.

TCM-HARQ protocols, as defined in [70], work as follows. At the transmitter, the TCM encoder output is transmitted as N-symbol packets. Each received packet is decoded with a Viterbi decoder; the test given in (6.12) is used to generate retransmission requests. That is, if the received packet satisfies (6.12), it is accepted and delivered to the data sink. Otherwise, the packet is rejected and a retransmission is requested. This process continues until a reliable packet is decoded.

Theoretically, this protocol might need an infinite number of retransmissions before a packet is accepted. Therefore, the probability $P(E)$ that an accepted packet contains errors is given by [73]

$$P(E) = \frac{P_{err}}{1 - P_r} \tag{6.45}$$

where P_r is the probability of retransmission of any packet and P_{err} is the probability that an accepted packet on any transmission contains errors. Clearly, P_{err} is given by (6.21) and by informationally weighting each error event, we obtain (6.23), which is the bit error probability of any given packet. Therefore, the average bit error probability, taking into account the possibility of retransmissions, is

$$P_b \leq \frac{1}{k_1}\left(\frac{1}{1 - P_r}\right)\sum_{j=1}^{\infty} m_j \psi(L_j, T)\left(\prod_{k \in \eta_j} \frac{1 + (1 - |\mu|^2)\gamma_s}{|\mu|^2 |x_{jk} - \hat{x}_{jk}|^2 \gamma_s / 4}\right). \tag{6.46}$$

The retransmission requests are generated in accordance with (6.12). Conse-

quently, the retransmission probability is

$$P_r \leq \sum_{j=1}^{\infty} \psi_1(L_j, T) \left(\prod_{k \in \eta_j} \frac{1 + (1 - |\mu|^2)\gamma_s}{|\mu|^2 |x_{jk} - \hat{x}_{jk}|^2 \gamma_s / 4} \right). \tag{6.47}$$

Then the throughput is

$$\eta = \left(\frac{k_1}{k_1 + 1} \right) (1 - P_r). \tag{6.48}$$

These above expressions are valid only for the case of ideal interleaving. Otherwise, the expressions given in Eqs. (6.25) and (6.34) must be used.

6.6 Results

To illustrate the results derived in this chapter, the eight-state TCM in Figure 4.2 combined with 8-PSK modulation is considered.

First, to establish the accuracy of the approximations developed thus far, consider the error event of length two between the two codewords $\mathbf{x} = (1, 1, \ldots)$ and $\hat{\mathbf{x}} = (e^{j\pi/2}, e^{j\pi}, 1, \ldots,)$. For the Rayleigh fading channel, Fig. 6.2 depicts the exact PEP and the approximation (6.21) as functions of the signal-to-noise ratio and the threshold T. The exact PEP is computed by evaluating Eq. (6.18). Similarly, for erasure probabilities, Eqs. (6.28) and (6.29) have been compared in Fig. (6.3). As might be expected, the accuracy of the approximations increases as the signal-to-noise ratio ratio increases and T decreases.

In the following, to compute the union bound on the bit error probability and the erasure or retransmission probability (see (6.23) and (6.32)), all error events whose length is less than or equal to five have been included. These were found by searching through the error state diagram given in [41]. Also, Figures (6.4) to (6.14) deal with ideally interleaved channels. In Figures (6.15) to (6.17), the performance when the interleaving capacity is finite is considered.

The bit error performance of a TCM-RS concatenated system is shown in Fig. (6.4), where three detection methods and an uncoded system have been considered. At 1% Doppler, pilot-aided detection is poorer than ideal coherent detection by about 1 dB in terms of the total signal power.

The variation of the Chernoff bound developed in Section (6.4.2) with the threshold T is plotted in Fig. (6.5) while keeping $\overline{E}_b/N_0$ constant. The optimum value of T increases with increasing $\overline{E}_b/N_0$.

Figure (6.6) shows the bite error probability for error and erasure decoding as a function of T and $\overline{E}_b/N_0$ (see (6.43)). Paradoxically, increasing $\overline{E}_b/N_0$ *increases* the bit error rate until it peaks and then declines. The initial behaviour is due to the fact that decreasing error and erasure probabilities can increase the upper bound given by (6.43), since $(1 - P_s - P_e)$ will increase in this case.

Figures (6.7) to (6.10) depict the throughput of the TCM-HARQ scheme in a Rayleigh fading channel where ideal coherent detection, differential detection, or pilot-aided detection is employed. For differential detection, μ is obtained assuming land mobile fading spectrum with 1% Doppler rate. For pilot-aided detection, the ratio of energy spent between the pilot and the data signals is $\sqrt{0.02}$. The individual curves are labelled with the threshold T (see (6.26)). Increased T causes a reduction in throughput due to the increased retransmissions.

For the same four cases, Figures (6.11) to (6.14) show the average bit error probability as a function of the threshold. Increased reliability is achieved by increasing T, at the cost of reduced throughput.

The bit error rate of the TCM-RS concatenated scheme as a function of the normalized fading bandwidth is shown in Fig. 6.15. The oscillatory behaviour is due to the Bessel auto-correlation function.

The effect of normalized fading bandwidth on the bit error probability and throughput of the ARQ scheme is shown in Figures 6.16 and 6.17. It can be seen that for small values of $N_d f_D T_s$, the throughput drops sharply and this drop

increases as more retransmissions take place.

6.7 Summary

The objective in this chapter has been to examine the performance of concatenated coding systems and ARQ systems operating on fading channels. To this end, new error expressions have been derived when the decoding is done by a modified VA. These show the asymptotic error behaviour at high signal-to-noise ratios and allow useful evaluation of the coding gain and throughput.

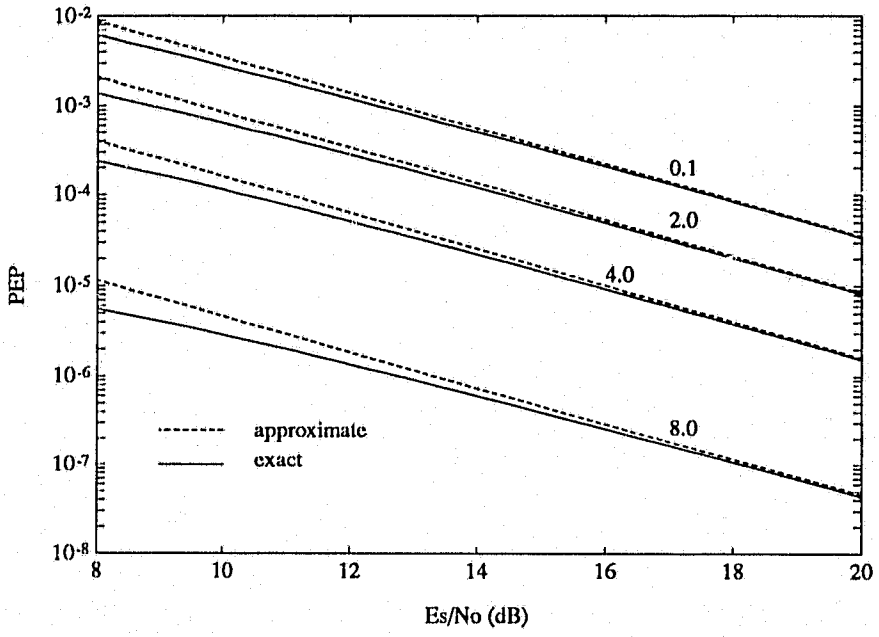

Figure 6.2: Comparison of exact and approximate PEP (coherent detection).

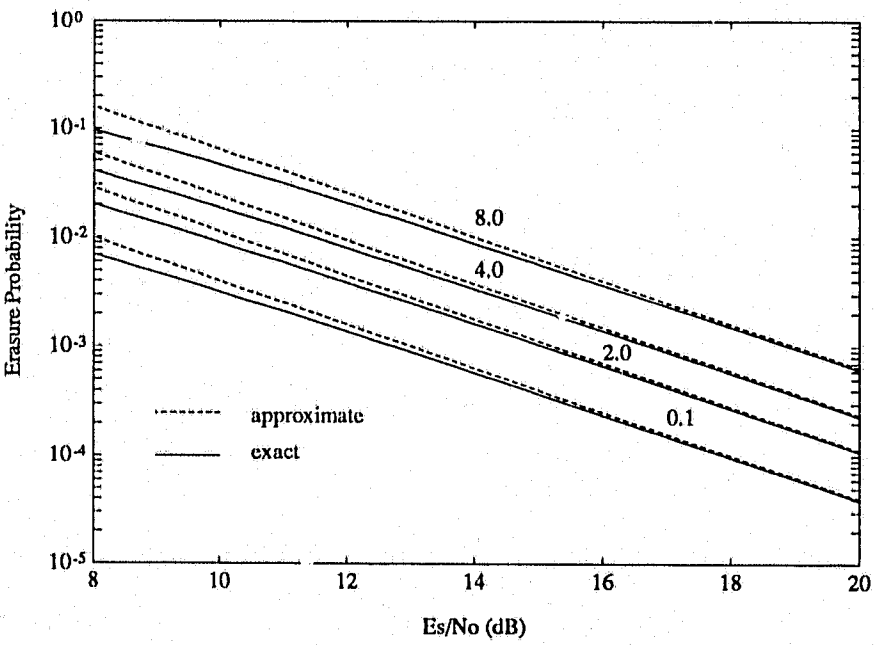

Figure 6.3: Exact and approximate Erasure Probability (coherent detection).

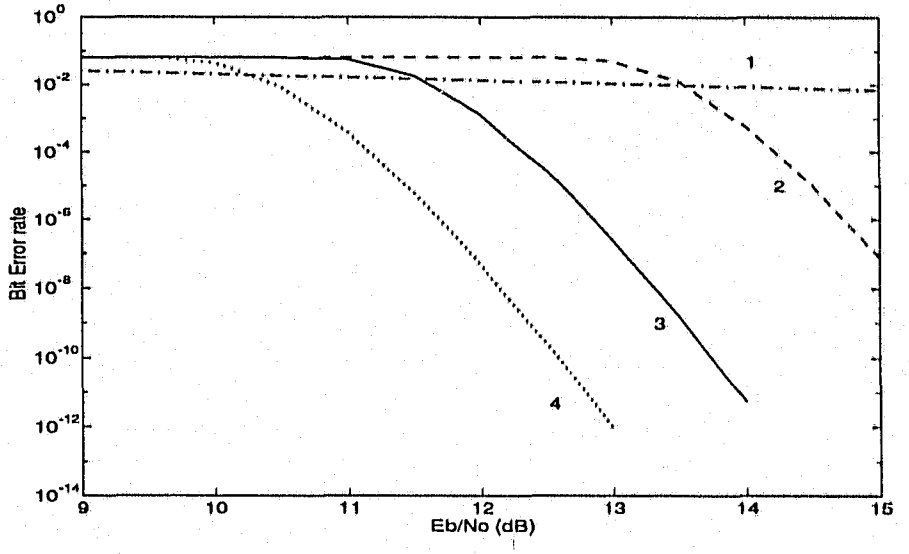

Figure 6.4: Bit error performance of the concatenated system with the 8-state TCM inner code and the (255,223) RS outer code on Rayleigh fading. 1: uncoded, 2: differential, 3: pilot-tone, 4: ideal coherent.

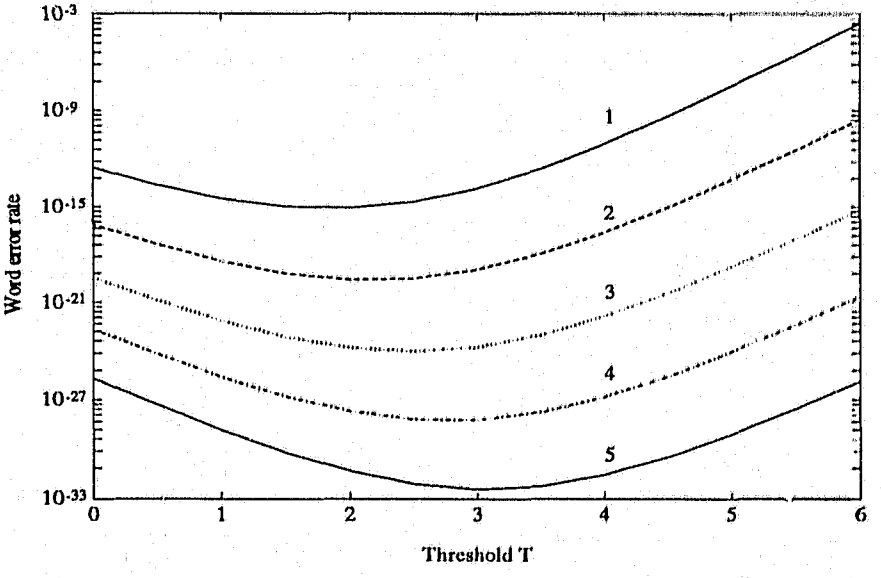

Figure 6.5: Chernoff bound on the word error rate as a function of the threshold T (coherent detection). 1: $E_b/N_0 = 10$ dB, 2: $E_b/N_0 = 10.5$ dB, 3: $E_b/N_0 = 11$ dB, 4: $E_b/N_0 = 11.5$ dB, 5: $E_b/N_0 = 12$ dB.

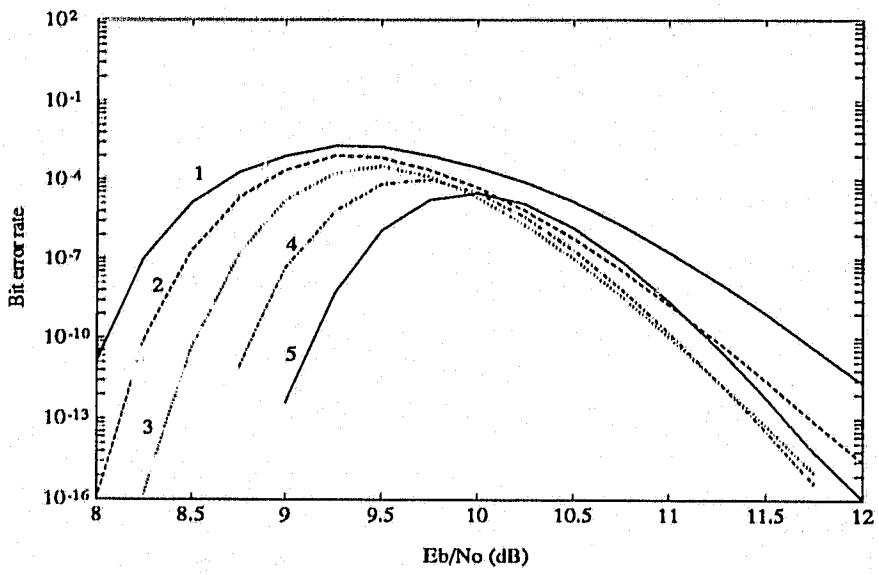

Figure 6.6: Bit error performance for errors and erasures decoding (coherent detection), $T_{es} = 32$. 1: $T = 1.0$, 2: $T = 2.0$, 3: $T = 3.0$, 4: $T = 4.0$, 5: $T = 5.0$.

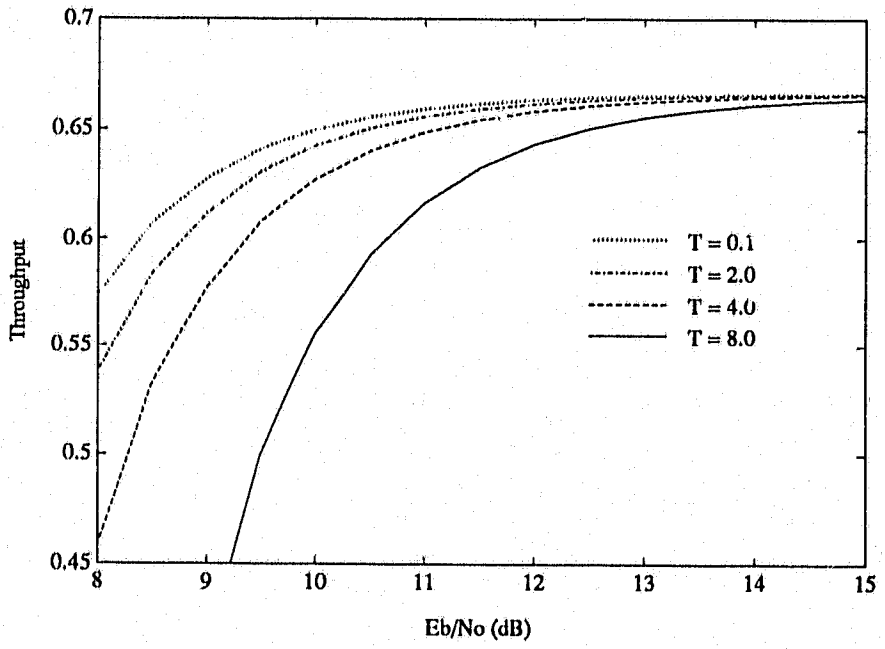

Figure 6.7: Throughput performance (coherent detection).

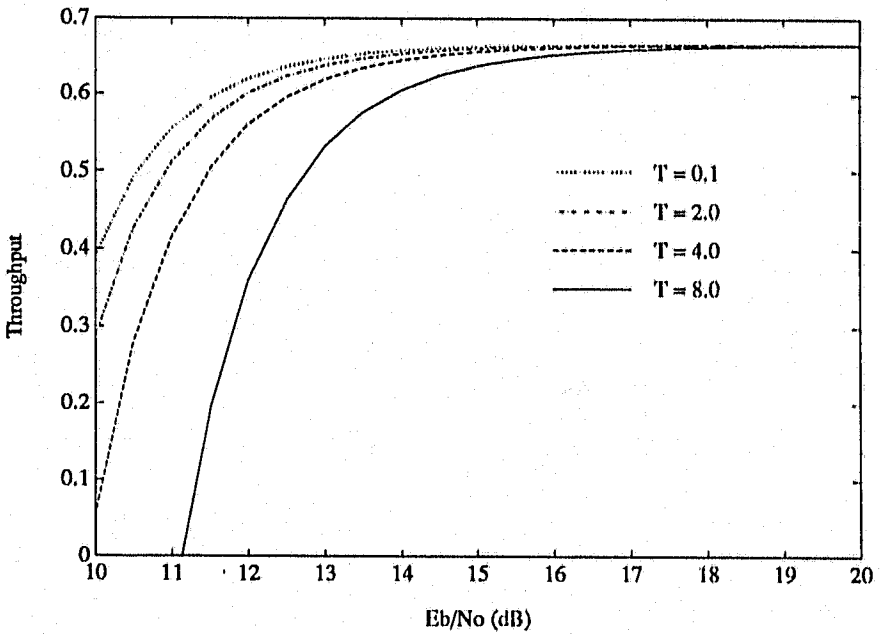

Figure 6.8: Throughput performance (differential detection).

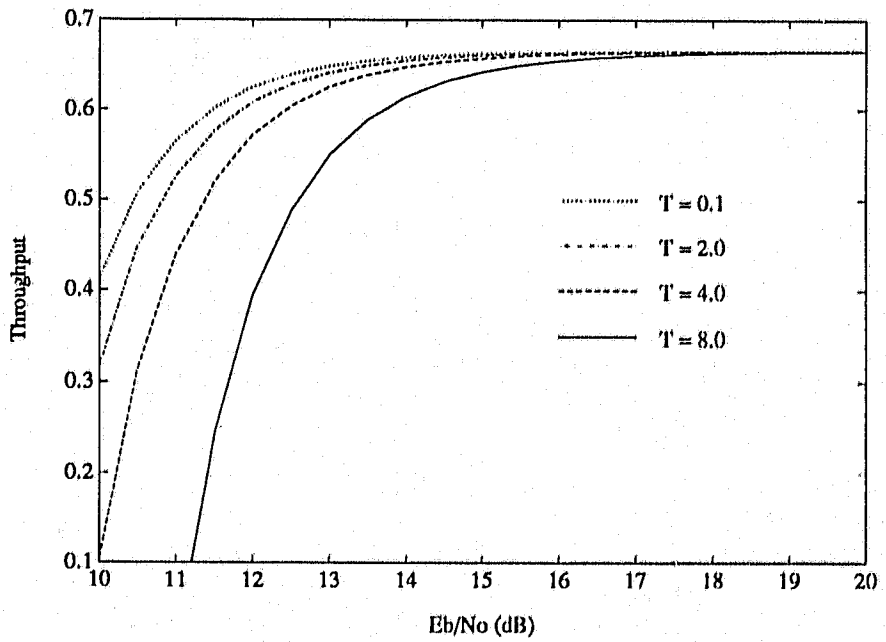

Figure 6.9: Throughput performance (slow fading, differential detection).

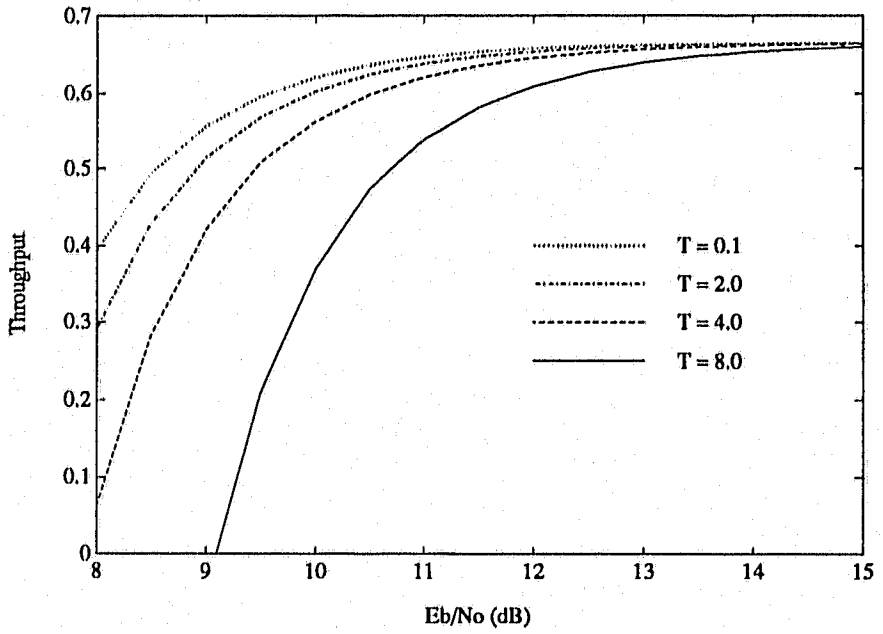

Figure 6.10: Throughput performance (pilot tone detection).

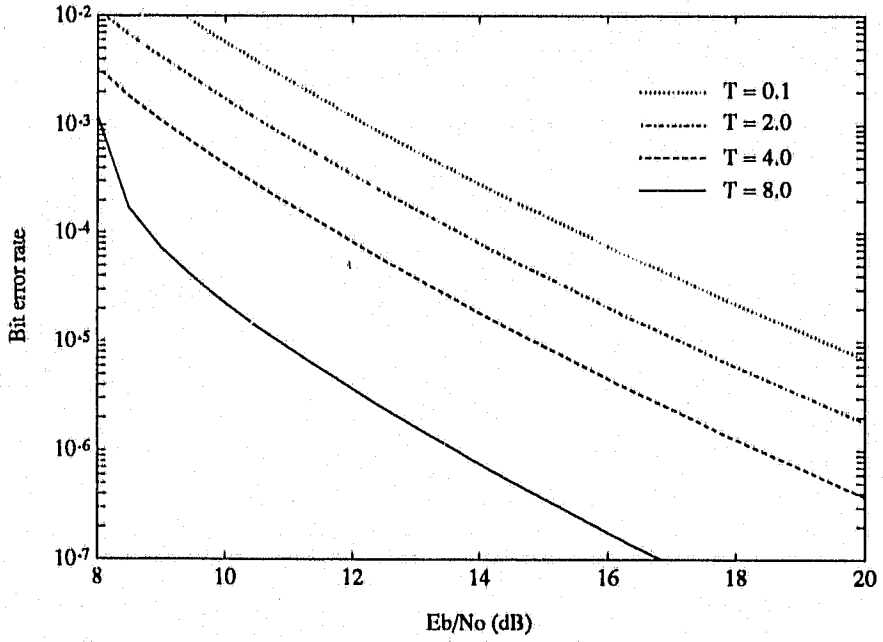

Figure 6.11: Bit error performance (coherent detection).

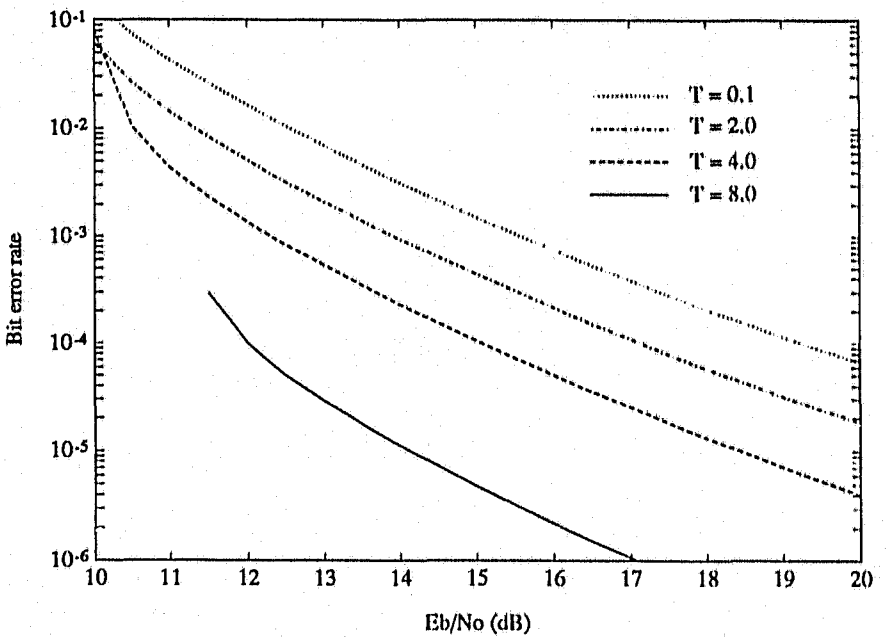

Figure 6.12: Bit error performance (differential detection).

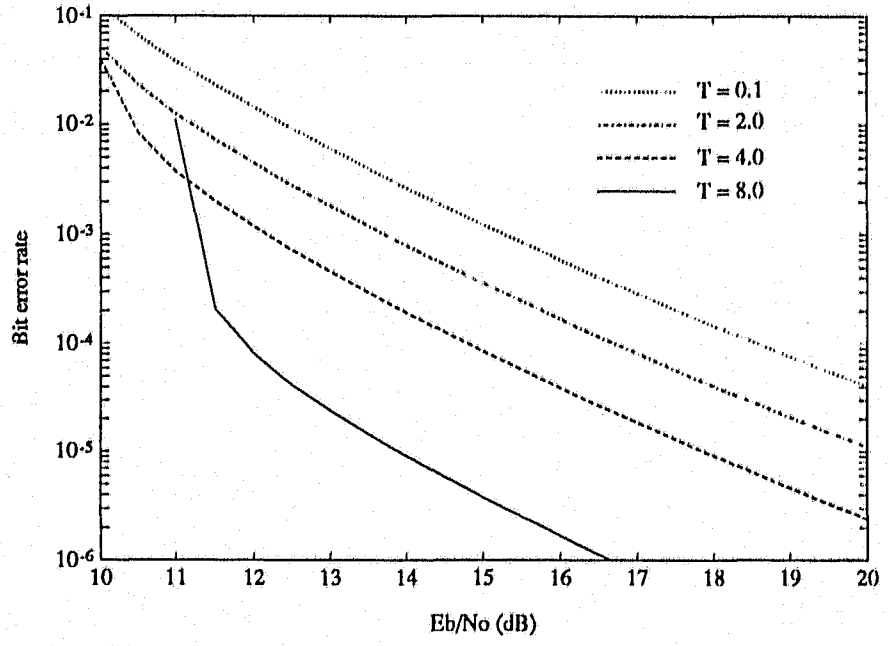

Figure 6.13: Bit error performance (slow fading, differential detection).

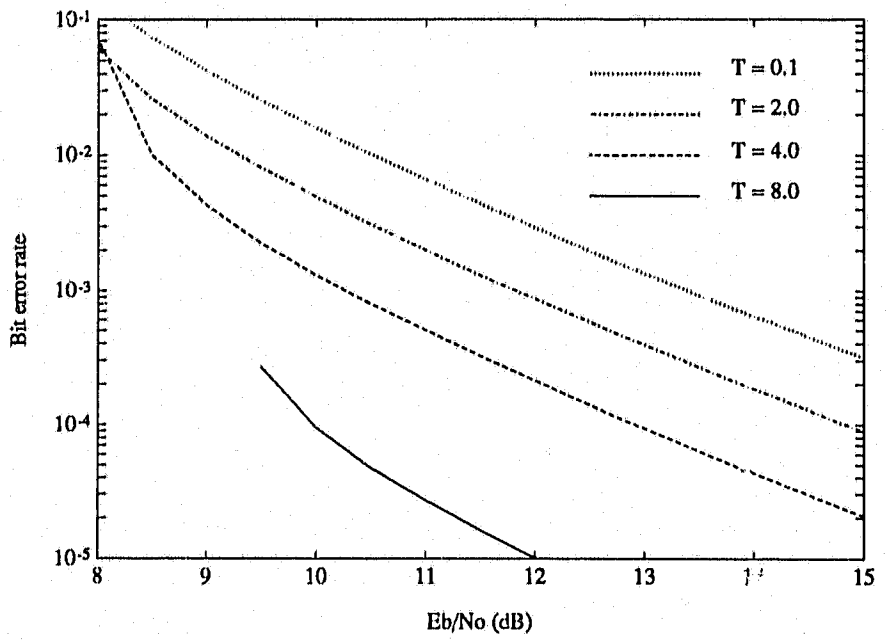

Figure 6.14: Bit error performance (pilot-tone detection).

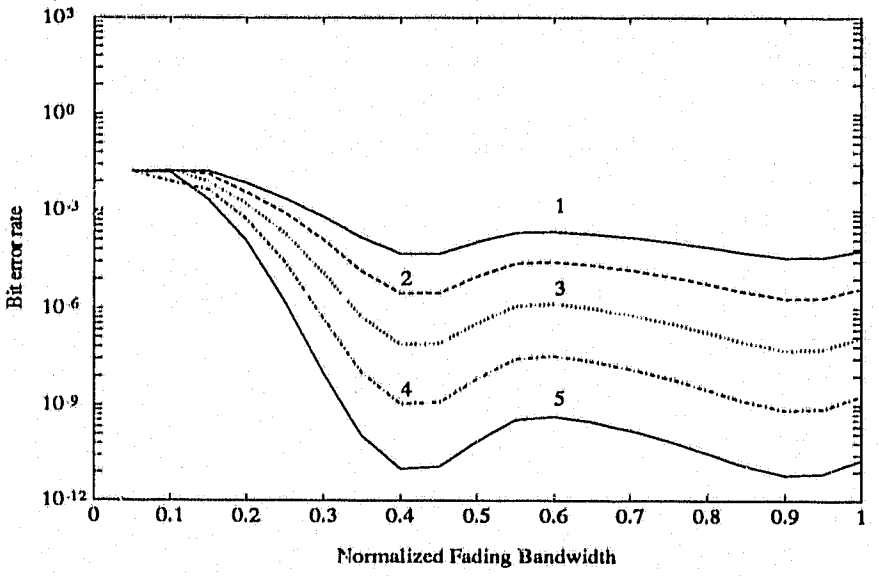

Figure 6.15: Bit error rate of the concatenated system (coherent detection). 1: $E_b/N_0 = 10$ dB, 2: $E_b/N_0 = 10.5$ dB, 3: $E_b/N_0 = 11$ dB, 4: $E_b/N_0 = 11.5$ dB, 5: $E_b/N_0 = 12$ dB.

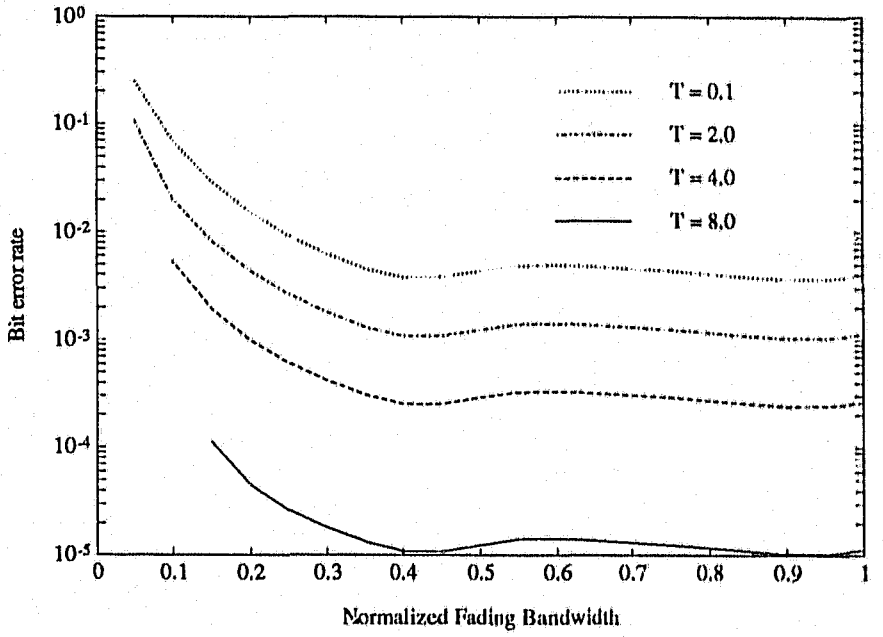

Figure 6.16: Bit error performance (coherent detection). $E_b/N_0 = 10$ dB.

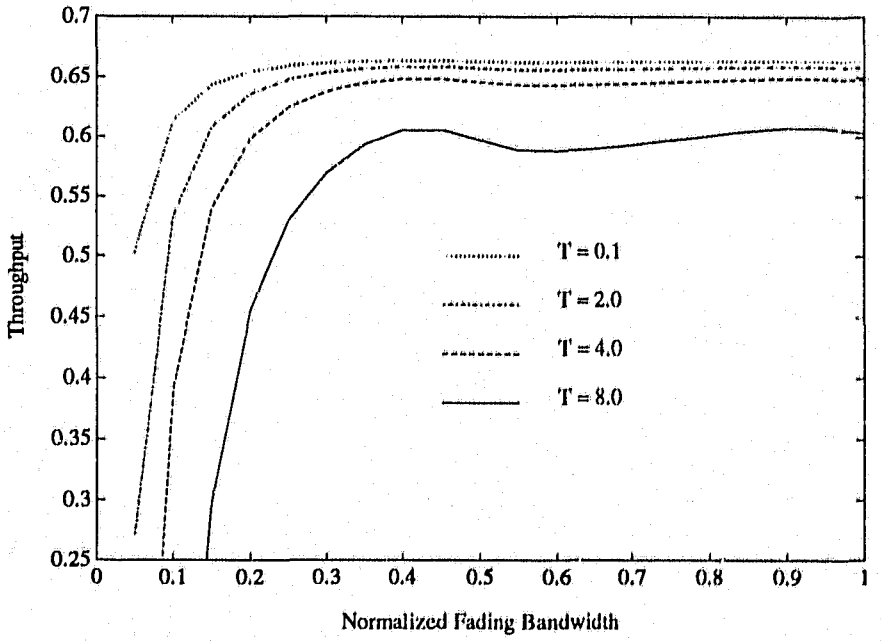

Figure 6.17: Throughput performance (coherent detection). $E_b/N_0 = 10$ dB.

Chapter 7

Convolutional Codes for Rayleigh Fading Channels

7.1 Introduction

In previous chapters, the performance of TCM in fading channels has been analyzed. In this chapter, the performance of convolutional codes with pilot-aided detection in the Rayleigh fading environment is analyzed. An upper bound on the bit error probability, the optimum power split ratio between the data and pilot signals, and the channel cut-off rate are derived.

Conventional convolutional codes are used with binary PSK, as opposed to M-ary PSK used with TCM, and have received a great deal of attention in the literature. Consequently, we limit our analysis to the performance of convolutional codes with PTAM (pilot tone assisted modulation) or PSAM (pilot symbol assisted modulation) in Rayleigh fading channels.

7.2 System Model

In the proposed system (Fig. 7.1), coded binary PSK symbols are interleaved, and transmitted along with a pilot tone or pilot symbols. A pilot tone extraction filter or an optimum interpolator using pilot symbols can be used to estimate the channel gain for each coded symbol. The channel gain estimates are then used to

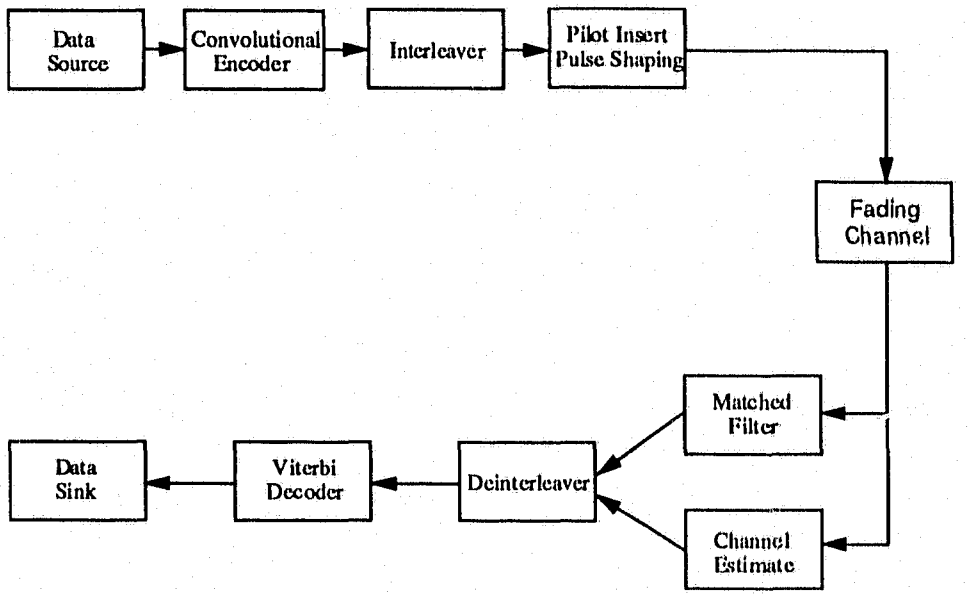

Figure 7.1: Coded BPSK with a pilot tone or pilot symbols.

form the metric that is used in the Viterbi decoder, following deinterleaving. In what follows, we assume perfect receiver timing, fading to be constant over a bit and, consequently, no intersymbol interference. We also assume ideal interleaving/deinterleaving.

The transmitted data signal can be represented by a complex envelope

$$s(t) = A \sum_{k=-\infty}^{\infty} b_k p(t - kT_s) \tag{7.1}$$

where $p(t)$ is a unit energy pulse, A is the amplitude of the data signal, T_s is the symbol duration, and b_k is the baseband equivalent of the convolutional encoder output, assuming values ± 1 (i.e., "0" to 1 and "1" to "-1"). The received data signal is detected with a matched filter whose impulse response is $p^*(-t)/\sqrt{N_0}$, where normalization by the additive noise power spectral density N_0 is made for notational convenience [16]. Then the filter output is given by

$$r_k = \frac{A\alpha_k}{\sqrt{N_0}} b_k + n_k = u_k b_k + n_k \tag{7.2}$$

where n_k is the additive white Gaussian noise with zero mean and unit variance, α_k is complex Gaussian with zero mean and variance σ^2, and $u_k = A\alpha_k/\sqrt{N_0}$.

Let v_k denote the estimate of u_k obtained via PTAM or PSAM methods. In the next section, a general expression for the PEP is derived, which is then specialized to pilot tone and pilot symbol methods.

7.3 Performance Analysis

With the channel estimates v_k, the Viterbi decoder uses the metric $|r_k - v_k b_k|^2$, which is the maximum likelihood metric if v_k is a perfect estimate of α_k. When evaluating the bit error probability of linear convolutional co'), it is customary to assume, without loss of generality, that all-zero codeword, $\mathbf{0} = \{111\cdots\}$, is transmitted. Thus, an error event occurs when the decoder chooses a non-zero codeword $\mathbf{x}_j \neq \mathbf{0}$. Let $\{x_{j1}, x_{j2}, x_{j3}, \cdots\}$ denote the baseband representation of $\mathbf{x}_j$ where $\{x_{jk} = \mp 1\}$ $(k = 1, 2, 3, \cdots)$. Thus, an error event happens if $\sum |r_k - v_k|^2 \geq \sum |r_k - v_k x_{jk}|^2$. Clearly, only the components $x_{jk} \neq 1$ contribute to this decision rule. Upon simplification of this decision rule, the decision variable is

$$U = \text{Real}\left(\sum_{w_j} r_k v_k^*\right) \tag{7.3}$$

where w_j is the Hamming distance between $\mathbf{0}$ and $\mathbf{x}_j$, and Real$(\bullet)$ is the real part. In the above, r_k and v_k are a pair of correlated complex Gaussian random variables, with all w_j pairs mutually statistically independent and identically distributed. Denote $\langle |r_k|^2 \rangle = \mu_1$, $\langle |v_k|^2 \rangle = \mu_2$, and $\langle r_k v_k^* \rangle = \rho\sqrt{\mu_1 \mu_2}$. To find an upper bound on the error event probability, we need the characteristic function of U given by [36, 4B.5]

$$\phi_U(s) = \left[\frac{v_1 v_2}{(s - v1)(s - v2)}\right]^{w_j} \quad v_1 < s < v_2 \tag{7.4}$$

where

$$\begin{bmatrix} v_1 \\ v_2 \end{bmatrix} = -w \pm \sqrt{w^2 + v_1 v_2} \tag{7.5}$$

and where

$$w = \frac{\text{Real}(\rho)}{\sqrt{\mu_1 \mu_2}(1 - |\rho|^2)}, \quad v_1 v_2 = \frac{1}{\mu_1 \mu_2 (1 - |\rho|^2)}. \tag{7.6}$$

By differentiating Eq. (7.4) with respect to s, we find that the tightest Chernoff bound is given by

$$P_e(\mathbf{0} \to \mathbf{x}_j) \leq \frac{1}{2}\left[\frac{1}{1+\theta}\right]^{w_j} \tag{7.7}$$

where

$$\theta \triangleq \frac{\text{Real}^2(\rho)}{1 - |\rho|^2}. \tag{7.8}$$

Note that the upper bound in Eq. (7.7) is the usual Chernoff bound tightened by a factor of one-half [74, App. 4].

This upper bound can also be used to determine the capacity of the coding channel, which is obtained via random coding arguments. Namely, the cut-off rate, R_0, for a Rayleigh fading channel with pilot aided detection may be defined as [74, 4.27]

$$R_0 = 1 - \log_2\left[1 + \frac{1}{1+\theta}\right] \quad \text{bits/symbol.} \tag{7.9}$$

R_0 can be considered as the practically achievable data rate per channel symbol, and is obtained as a function of the system parameters. Hence, this allows for a quick appraisal of system performance irrespective of the specific convolutional code.

7.3.1 Coded PTAM

As in Chapter 3, the received pilot signal is detected with a matched filter with frequency response

$$H(f) = \begin{cases} \frac{A}{B\sqrt{N_0}} & -W_p/2 \le f \le W_p/2 \\ 0 \text{ otherwise} \end{cases} . \tag{7.10}$$

Once again, normalization by the factor $\frac{A}{B\sqrt{N_0}}$ is made for notational convenience. For undistorted measurement of the fading process, the bandwidth of the pilot extraction filter should at least be $2f_D$ where f_D is the maximum Doppler spread. Then the output of the pilot extraction filter is given by

$$v_k = \frac{A\alpha_k}{\sqrt{N_0}} + \eta_k \tag{7.11}$$

where η_k is a complex Gaussian with zero mean and a variance of $W_pA^2/B^2 = W_pT_s/r$. η_k is uncorrelated with the noise term n_k in Eq. (7.2). α_k is the Rayleigh fading term affecting the pilot which is assumed to be equal to α_k in Eq. (7.2).

The received signal energy to noise-spectral density ratio (SNR) can be defined, including both the data and pilot signals, as

$$\gamma_s = \frac{\overline{E}_s}{N_0} = \frac{\sigma^2A^2}{N_0} + \frac{\sigma^2B^2T_s}{N_0}. \tag{7.12}$$

By evaluating the variances of r_k and v_k and the correlation between them and substituting these in Eq. (7.8), we have

$$\theta = \frac{\gamma_s^2}{(1+r)\gamma_s + W_pT_s\frac{(1+r)^2}{r} + W_pT_s\gamma_s\frac{1+r}{r}}. \tag{7.13}$$

To obtain an upper bound on the bit error probability, Eq. (7.7) and union bounding methods can be used.

Minimizing the denominator of θ with respect to r, it follows that the optimum choice energy split ratio r between the data and pilot signals is

$$r_{opt}^2 = \frac{W_p T_s(1+\gamma_s)}{(W_p T_s + \gamma_s)} \approx W_p T_s. \tag{7.14}$$

Note that as γ_s increases, r_{opt} is solely dependent on $W_p T_s$. Thus, the power allocated to the pilot tone need not be dynamically changed with increasing SNR. This has also been observed in [16, 17].

7.3.2 Coded PSAM

In a pilot-symbol based system, coded binary PSK symbols are interleaved, and the transmitter inserts a known symbol at the beginning of each coded symbol frame of length $M-1$. As proposed in [39] , using K pilot samples, an optimum filter estimates channel gain for each coded symbol bit. The channel gain estimates are then used to form the metric to be used in the Viterbi detector following deinterleaving. As mentioned in [39], the choice of frame size M, number of pilot samples K and optimum filter coefficients is dictated by the anticipated worst case Doppler fading bandwidth and residual frequency offset.

For simplicity let both the data and pilot symbols be of the same amplitude. Then, the received SNR can be defined,

$$\gamma_s = \frac{\overline{E}_s}{N_0} = \frac{\sigma_g^2 A^2}{N_0} \frac{M}{M-1} \tag{7.15}$$

which follows from the fact that one frame consists of $M-1$ coded bits and one pilot bit. Then the variance of $u(k)$ is given by

$$\sigma_u^2 = \gamma_s \frac{M-1}{M}. \tag{7.16}$$

Since α_k is a wide sense stationary Gaussian process, in [39] a Wiener filter has been proposed to interpolate $u(k)$ for $k \neq iM$ given the noise corrupted pilot

symbol sequence $u(iM)+n(iM)$. Without loss of generality, we can write down the interpolation equations for the first frame as subsequent frames would be analyzed identically. So considering the first frame, for $k = 1, \cdots, M-1$ the Wiener filter estimates $u(k)$ in Eq. (7.2) using K pilot samples [39],

$$v(k) = \sum_{i=-\lfloor K/2 \rfloor}^{\lfloor K/2 \rfloor} h^*(k) r(iM) = \mathbf{h}^\dagger(k)\mathbf{r}(k). \tag{7.17}$$

where the dagger denotes conjugate transpose and $\mathbf{r}$ is the length K column vector consisting of the set of pilot samples $r(iM)$, $-\lfloor K/2 \rfloor \leq i \leq \lfloor K/2 \rfloor$. The position-dependent filter coefficients $h(k)$ are determined according to the normal equation [39]

$$\mathbf{R}\mathbf{h}(k) = \mathbf{w}(k) \text{ for } k = 1, \cdots, M-1 \tag{7.18}$$

where

$$\mathbf{R} = \frac{1}{2}E[\mathbf{r}\mathbf{r}^*] \text{ and } \mathbf{w}(k) = \frac{1}{2}E[u^*(k)\mathbf{r}]. \tag{7.19}$$

Now in this coded scheme, the error rate is dependent on how well $r(k)$ and $v(k)$ are correlated, and the normalized correlation coefficient is [39]

$$\rho(k) = \frac{\mathbf{w}^\dagger(k)\mathbf{R}^{-1}\mathbf{w}(k)}{\sqrt{(\sigma_u^2 + 1)\mathbf{w}^\dagger(k)\mathbf{R}^{-1}\mathbf{w}(k)}}. \tag{7.20}$$

Now both $\rho(k)$ and $\sigma_v^2(k)$, the variance of $v(k)$, are clearly position dependent. However, the variation of these across a frame is very low, for example about 0.02 % for the PSAM scheme considered later in this chapter. Hence, we ignore this variation and assume $\rho = \rho(1)$ and $\sigma = \sigma_v^2(k)$ to be the nominal values for all k. This assumption considerably simplifies the analysis, and the bit error rate can now be obtained via Eq. (7.7).

7.4 Results

Having determined the pairwise error probability, the next step is to use the union bound on the bit error probability. The average bit error probability $E(P_b)$ of a rate $R_0 = b/v$ linear convolutional code can be bounded as [36]

$$E[P_b] < \frac{1}{b}\frac{dT(D,N)}{dN}\bigg|_{N=1,D=\delta} \tag{7.21}$$

where $T(D,N)$ denotes the standard transfer function of the code, and δ varies according to the detection method. For the sake of comparison, it is given by

$$\delta = \begin{cases} 1/(1+\theta) & \text{PSAM or PTAM} \\ 1/(1+\gamma_s) & \text{Ideal coherent detection} \\ ((1-\mu^2)\gamma_s^2 + (1+2\gamma_s))/(1+\gamma_s)^2 & \text{Differential detection [75]} \end{cases} \tag{7.22}$$

where μ is the normalized correlation coefficient between adjacent fading variables, given by $\mu = J_0(2\pi f_D T_s)$ for land mobile channels. Finally, with the use of Eqs. (7.7), (7.20) and (7.21), the error rate performance of any linear convolutional coded binary PSAM or PTAM can be analyzed.

As the first example, consider an optimal convolutional code with rate $R_0 = \frac{1}{2}$ and the constraint length $K = 7$. Using the weight distribution of this convolution code [74] , the bit error upper bound is

$$P_b \leq \frac{1}{2}[36D^{10} + 211D^{12} + 1404D^{14} + 11633D^{16} + \cdots]\Big|_{D=\frac{1}{1+\theta}} \tag{7.23}$$

The BEP curves of pilot tone technique are depicted on Fig. 7.2 for three normalized, maximum Doppler rates, $f_D T_s$, of 1%, 2%, 5%. And, as indicated by (9), the power split ratio between the pilot and the data signals, r, is 0.14, 0.2, 0.32, respectively. By comparison, also shown are the BEP curves for ideal coherent detection and differential detection under ideal and fast fading conditions. In particular, for the pilot tone technique and ideal differential detection the correlation

coefficient μ is taken to be unity while for differential detection with fast fading, $\mu = J_0(2\pi f_D T_s)$. We see that the pilot tone scheme is at most 3dB worse than than ideal, unattainable coherent detection. It is also better than differential detection, even under very slow fading (i.e., $\mu \approx 1$). Moreover, differential detection causes error floors, which in this case are suppressed by the powerful code being used.

As the second example, for binary PSAM coded with a rate $R_0 = \frac{1}{2}$ $K = 3$ optimum convolution code, the bit error probability is computed. For this code, the transfer function $T(D, N)$ is given in [76]. We consider a PSAM scheme with the frame size M=7, the number of pilot samples K=11, and normalized Doppler fading bandwidths 5%, 1% and 0.1%. Using (7.20), (7.21) and (7.22), Fig. 7.5 has been plotted, with the coefficients optimised at each Doppler bandwidth. We see that, even at 5% Doppler fading bandwidth, coded PSAM requires only 3.5 dB more than coherent detected coded system while at 1% Doppler the loss is about 2 dB. The same amount of loss has been obtained in [39] for uncoded systems. Also, it is seen that coded PSAM has no error floor while coded DPSK has one. While the number of pilot samples K has been fixed at 11 for this example it can be as low as 5, as noted in [11, 39], if the anticipated worst case Doppler is small ($< 1\%$). This is the typical case in practice. By reducing the number of pilot samples, the required interleaving depth can also be reduced.

7.5 Summary

This chapter analyzed convolutional coding for binary PSK with a pilot-tone for phase correction over Rayleigh fading channels. As might be anticipated, the performance of this scheme lies between that of ideal and differential detection techniques. At moderate and high SNRs, the power allocated to the pilot is essentially fixed by the maximum Doppler shift.

Coded binary PSAM compares well with unattainable coherently detected coded BPSK requiring only 3.5 dB more at 5% Doppler fading bandwidth. Also,

PSAM outperforms coded differential detection and removes error floors completely. Finally, it provides a significant coding gain over uncoded coherent BPSK.

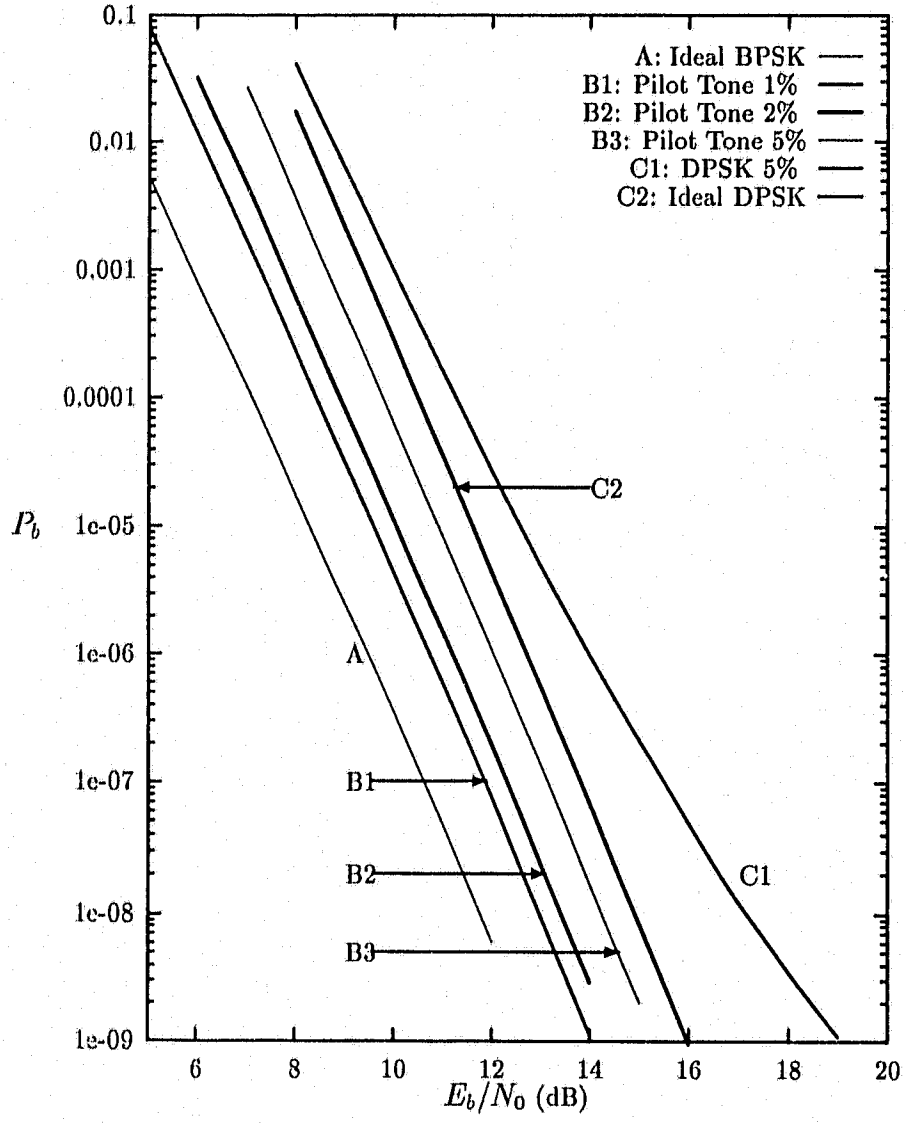

Figure 7.2: Bit error probability versus E_b/N_0 (R=1/2, K=7). Rayleigh fading channel with different modulation techniques.

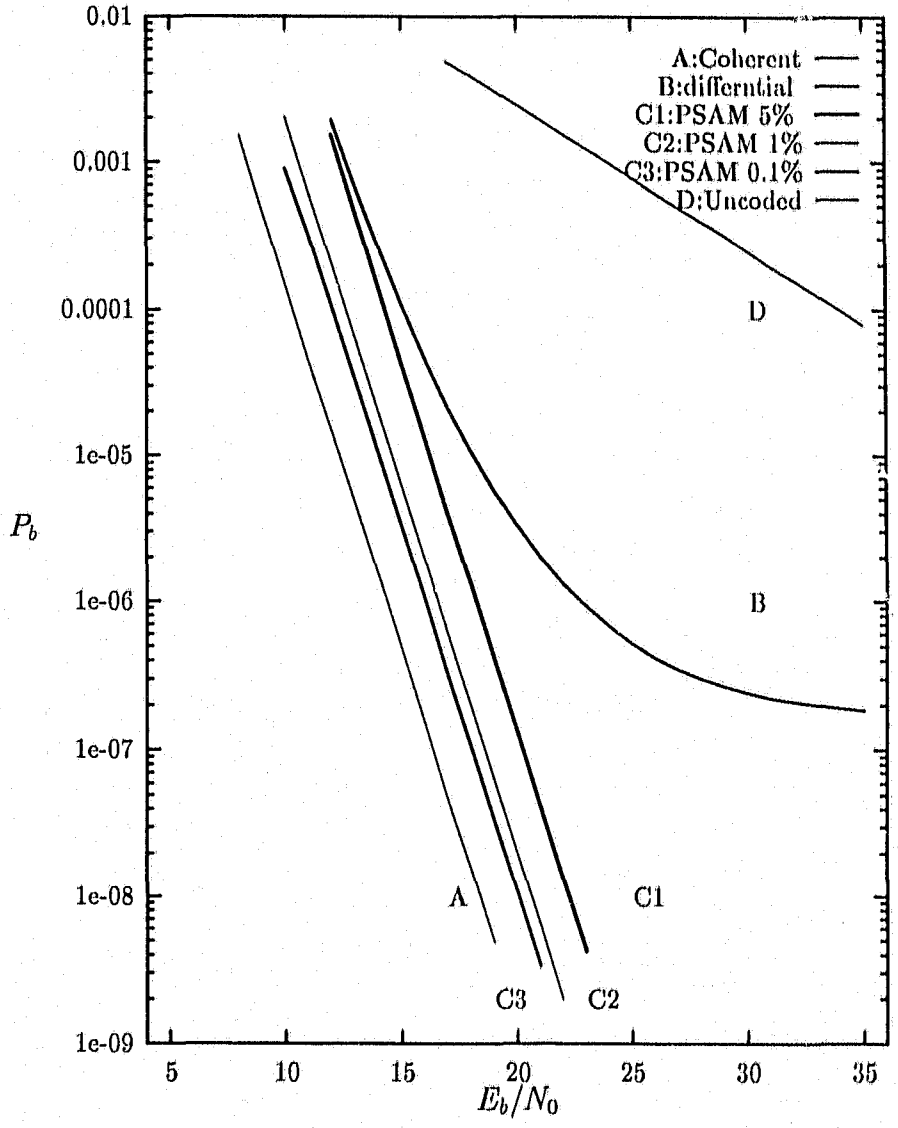

Figure 7.3: Bit error probability for a R=1/2 and K=3 convolution code with different modulation techniques in Rayleigh fading

Chapter 8

Summary of Results and Further Research

8.1 Summary of Results

Chapter 1 gave the motivation for this research and a brief review of relevant, previous work. The objectives and contributions of the present study were stated.

Chapter 2 presented brief explanations on the concept of TCM, the Rician model, the system model, and interleaving.

In Chapter 3, an approximate expression for the PEP of TCM in Rician fading was developed. The expression was simplified for ideally interleaved channels, yielding the PEP of the pilot-tone model. The resulting error bounds were tighter than the ones based on the ordinary Chernoff bound.

The approximate expressions developed in Chapter 3 were extended in Chapter 4 to the ideally interleaved, shadowed Rician fading channel. The analysis was based on the pilot-tone model, and the results were substantiated by means of computer simulation. In addition, first order statistics of absolute and differential phases (Appendix C) of a shadowed Rician process were derived.

In Chapter 5, the error performance of TCM over nonindependent Rician fading channels was considered. An upper bound for the PEP was developed. In addition, for Rayleigh fading channels with an exponential auto-covariance function, bounds resembling those for memoryless channels were derived.

The performance of concatenated coding systems and ARQ systems operating over the Rayleigh channel was derived in Chapter 6. The analysis took into account a modified VA as well as limited interleaving.

In Chapter 7, the performance of binary convolutional codes in Rayleigh fading was analyzed.

In summary, the performance of coded systems in fading channels was addressed in detail in this work. The analysis showed the interplay between the various system parameters in determining the overall error performance. The derived bounds allowed for accurate estimation of system performance when some of the usual assumptions were relaxed.

8.2 Further Research

Concerning the performance of coded systems in fading environments, three possible continuations of the results presented in this thesis are as follows.

1. The focus in this thesis has been on the frequency non-selective fading, but the use of TCM in frequency selective fading channels may also be a useful area of research.

2. Since conventional differential detection fares poorly in comparison to perfect coherent detection in fading channels, multiple-symbol differential detection in which two or more previous samples are used to estimate the channel gain has been reported in the literature. The performance of this technique in frequency selective fading channels and shadowed Rician fading channels should be investigated.

3. In this work, only PSK signalling has been considered. TCM with frequency-shift-keying (FSK) has received some attention in the literature. Since FSK is well-suited for fading channels, the performance of TCM with FSK in fading environments may be explored.

Bibliography

[1] W. C. Jakes (Ed.), *Microwave mobile Communications.* New York: John Wiley, 1974.

[2] W. C. Y. Lee, *Mobile Communications Engineering.* New York: McGraw-Hill, 1982.

[3] R. A. Kennedy, *Fading dispersive channels.* New York: Wiley, 1969.

[4] S. H. Jamali and T. Le-Ngoc, "Performance comparison of different decoding strategies for a bandwidth-efficient block-coded scheme on mobile radio channels," *IEEE Trans. Veh. Technol.*, vol. 41, pp. 505–515, Nov. 1992.

[5] G. Ungerboeck, "Channel coding with multilevel/phase signals," *IEEE Trans. Inform. Theory.*, vol. 28, pp. 55–67, Jan. 1982.

[6] M. K. Simon, E. Biglieri, P. J. McLane and D. Divsalar, *Introduction to Trellis-Coded Modulation with Applications.* New York: McMillan, 1991.

[7] F. Davarian, "Mobile digital communications via tone calibration," *IEEE Trans. Veh. Technol.*, vol. 36, pp. 55–62, May 1987.

[8] J. McGeehan and A. Bateman, "Phase-lock transparent tone-in-band (TTIB): A new spectrum configuration particularly suited to the transmission of data over SSB mobile radio networks," *IEEE Trans. Commun.*, vol. 32, pp. 81–87, Jan. 1984.

[9] M. K. Simon, "Dual pilot tone calibration technique (DTCT)," *IEEE Trans. Veh. Technol.*, vol. 35, pp. 63–70, May 1986.

[10] M. L. Moher and J. H. Lodge, "TCMP-a modulation and coding strategy for Rician fading channels," *IEEE J.Select.Areas. Commun.*, vol. 7, pp. 1347–1355, Dec. 1989.

[11] S. Sampei and T. Sunaga, "Rayleigh fading compensation method for 16-QAM in digital land mobile radio channels," in *Proc. 1989 IEEE Vehicular Tech. Conf.*, May 1989.

[12] D. Divsalar and M. K. Simon, "Trellis-coded modulation for 4800 to 9600 bps transmission over a fading satellite channel," *IEEE J.Select.Areas. Commun.*, vol. 5, pp. 162–175, Feb. 1987.

[13] S. G. Wilson and Y. S. Leung, "Trellis coded phase modulation on Rayleigh channels," in *Proc. 1987 Int.Conf.Commun*, pp. 21.3.1–21.3.5, June 1987.

[14] M. K. Simon and D. Divsalar, "The performance of trellis-coded multilevel DPSK on a fading mobile satellite channel," *IEEE Trans. Veh. Technol.*, vol. 37, pp. 78–91, May 1988.

[15] D. Divsalar and M. K. Simon, "Performance of trellis-coded MDPSK on fast fading channels," in *ICC'89 Conference Rec.*, (Boston, Mass.), pp. 9.1.1–9.1.7, June 1989.

[16] J. K. Cavers and P. Ho, "Analysis of the error performance of trellis coded modulations in Rayleigh fading channels," *IEEE Trans. Commun.*, vol. 40, pp. 74–83, Jan. 1992.

[17] K. Chan and A. Bateman, "The performance of reference-based M-ary PSK with trellis coded modulation in Rayleigh fading," *IEEE Trans. Veh. Technol.*, vol. 41, pp. 190–198, May 1992.

[18] K. Chan and A. Bateman, "Performance of MPSK with trellis-coded modulation in Rayleigh fading with an imperfect phase reference," *IEE Proc. -I*, vol. 139, pp. 329–335, June 1992.

[19] P. Ho and D. Fung, "Error performance of interleaved trellis-coded PSK modulations in correlated Rayleigh fading channels," *IEEE Trans. Commun.*, vol. 40, pp. 1800–1809, Dec. 1992.

[20] P. Ho and D. Fung, "Error probability of trellis-coded with correlated Rayleigh fading," in *Fifteenth Biennial Symp. Commun.*, (Queens Univ., Kingston, Canada), pp. 116–119, June 1990.

[21] D. Fung, "Error performance of PSK signals transmitted over correlated Rayleigh fading channels," Master's thesis, Simon Fraser Univ., British Columbia, Canada, July 1991.

[22] G. Ungerboeck, "Trellis-coded modulation with redundant signal sets part i," *IEEE Commun. Mag.*, vol. 25, pp. 5–11, Feb. 1987.

[23] G. Ungerboeck, "Trellis-coded modulation with redundant signal sets part ii: State of the art," *IEEE Commun. Mag.*, vol. 25, pp. 12–21, Feb. 1987.

[24] D. Divsalar and M. K. Simon, "The design of trellis coded MPSK for fading channels: performance criteria," *IEEE Trans. Commun.*, vol. 36, pp. 1004–1011, Sept. 1988.

[25] D. Divsalar and M. K. Simon, "The design of trellis coded MPSK for fading channels: Set partitioning for optimum code design," *IEEE Trans. Commun.*, vol. 36, pp. 1013–1021, Sept. 1988.

[26] M. K. Simon, D. Divsalar and T. Jedry, "Trellis coding techniques for mobile communications," in *MILCOM'88 Conference Rec.*, (San Diego), pp. 653–659, Oct. 1988.

[27] C. Schlegel and D. J. Costello, "Bandwidth efficient coding for fading channels: Code construction and performance analysis," *IEEE J.Select.Areas. Commun.*, vol. 7, pp. 1356–1369, Dec. 1989.

[28] S. H. Jamali and T. Le-Ngoc, "A new 4-state 8PSK TCM scheme for fast fading, shadowed mobile radio channels," *IEEE Trans. Veh. Technol.*, vol. 40, pp. 216–222, Feb. 1991.

[29] W. R. Bennet, M. Schwartz and S. Stein, *Communication Systems and Techniques.* New York: McGraw-Hill, 1966.

[30] G. Clark and J. B. Cain, *Error-Correction coding for Digital communications.* New York: Plenum, 1981.

[31] J. Huang and L. Campbell, "Trellis coded MDPSK in correlated and shadowed Rician fading channels," *IEEE Trans. Veh. Technol.*, vol. 40, pp. 786–797, Nov. 1991.

[32] C. W. Helstrom, "Computing the performance of optical receivers with avalanche diode detectors," *IEEE Trans. Commun.*, vol. 36, pp. 61–66, Jan. 1988.

[33] C. W. Helstrom, "Approximate evaluation of detection probabilities in radar and optical communications," *IEEE Trans. Aerosp.Electron. Syst.*, vol. 14, pp. 630–640, July 1978.

[34] K. Schumacher and J. J. O'Reilly, "Relationship between the saddle point approximation and the modified chernoff bound," *IEEE Trans. Commun.*, vol. 38, pp. 270–272, Mar. 1990.

[35] P. J. McLane *et al.*, "PSK and DPSK trellis codes for fast fading, shadowed mobile satellite communication channels," *IEEE Trans. Commun.*, vol. 36, pp. 1242–1246, Nov. 1988.

[36] J. G. Proakis, *Digital Communications.* New York: McGraw-Hill, 1983.

[37] N. Bleistein and R. A. Handelsman, *Asymptotic expansions of integrals.* New York: Dover, 1986.

[38] F. Gagnon and D. Haccoun, "Bounds on the error performance of coding for non-independent Rician fading channels," *IEEE Trans. Commun.*, vol. 40, pp. 351–360, Feb. 1992.

[39] J. K. Cavers, "An analysis of pilot symbol assisted modulation for Rayleigh fading channels," *IEEE Trans. Veh. Technol.*, vol. 40, pp. 686–693, Nov. 1991.

[40] E. Biglieri and P. J. McLane, "Uniform distance and error probability properties of TCM schemes," *IEEE Trans. Commun.*, vol. 39, pp. 41–52, Jan. 1991.

[41] R. G. McKay *et al.*, "Error bounds for trellis-coded MPSK on a fading mobile satellite channel," *IEEE Trans. Commun.*, vol. 39, pp. 1750–1761, Dec. 1991.

[42] J. W. Modestino and S. Y. Mui, "Convolutional code performance in the Rician fading channel," *IEEE Trans. Commun.*, vol. 24, pp. 592–606, June 1976.

[43] C. Loo, "A statistical model for a land mobile satellite link," *IEEE Trans. Veh. Technol.*, vol. 34, pp. 122–127, Aug. 1985.

[44] C. Loo *et al.*, "Measurements and modelling of land mobile satellite signal statics," in *1986 vehicular Technology Conference*, vol. 34, (Dallas, Texas), pp. 262–267, May 1986.

[45] C. Loo, "A statistical model for a land mobile satellite link," vol. 34, pp. 122–127, Aug. 1984. Links for the future (ICC' 84), Science, systems and services for communication, P.Dewilde and C.A. May, editors, IEEE/Elsevier Science Publishers, North Holland.

[46] C. Loo, "Measurements and models of a mobile satellite link with applications," in *Proc. GLOBECOM 85*, (Neworleans, LA.), pp. 1177–1180, Dec. 1985.

[47] P. J. McLane *et al.*, "PSK and DPSK trellis codes for fast fading, shadowed mobile satellite communication channels," in *Proc. 1987 Int. Conf. Commun.*, (Seattle,WA), pp. 726–731, June 1988.

[48] A. C. M. Lee, "Analysis of amplitude, phase and error distributions for shadowed mobile satellite communication channels," Master's thesis, Dep. Elec. Eng., Queen's Univ., Kingston, Ont., Canada, Aug. 1988.

[49] A. C. M. Lee and P. J. McLane, "Convolutionaly interleaved PSK and DPSK trellis code for shadowed, fast fading mobile satellite communication channels," *IEEE Trans. Veh. Technol.*, vol. 39, pp. 37–47, June 1990.

[50] C. Loo and N. Secord, "Computer models for fading channels with applications to digital transmission," *IEEE Trans. Veh. Technol.*, vol. 40, pp. 700–707, Nov. 1991.

[51] C. Tellambura, Q. Wang, and V. K. Bhargava, "A performance analysis of trellis-coded modulation schemes over Rician fading channels," *IEEE Trans. Veh. Technol.*, 1993. To appear.

[52] S. Y. Mui and J. W. Modestino, "Performance of DPSK with convolutional encoding on time-varying fading channels," *IEEE Trans. Commun.*, vol. 25, pp. 1075–1083, Oct. 1977.

[53] C. Tellambura and V. K. Bhargava, "Trellis coded modulation schemes for shadowed Rician fading channels," *Electronics Letters*, vol. 297, pp. 635–637, Apr. 1993.

[54] I. N. Sneddon, *Special functions in mathematical physics and chemistry*. London: Longman, 1980.

[55] J. K. Cavers, "Performance of tone calibration with frequency offset and imperfect pilot filter," *IEEE Trans. Veh. Technol.*, vol. 40, pp. 426–434, May 1991.

[56] R. Kerr, "Coherent detection of interleaved CPFSK on various shadowed mobile satellite channels," Master's thesis, Dep. Elec. Eng., Queen's Univ., Kingston, Ont., Canada, Aug. 1989.

[57] J. N. Pierce and S. Stein, "Multiple diversity with nonindependent fading," *Proc. IRE*, vol. 48, pp. 196–211, Oct. 1960.

[58] F. Gagnon and D. Haccoun, "On the performance of error control coding with diversity for mobile channels," *IEEE Trans. Veh. Technol.*, vol. 41, pp. 488–495, Nov. 1992.

[59] F. Gagnon and D. Haccoun, "On the performance of error control coding with diversity for mobile channels," *Proc. IEEE GlobeCom*, pp. 902.2.1–902.2.5, 1990.

[60] J. Dunham and K. Tzou, "Performance bounds for convolutional codes on Rician fading channels," in *Proc. IEEE Int. Conf. Commun.*, pp. 12.4.1–12.4.5, June 1981.

[61] J. Hagenauer, "Viterbi decoding of convolutional codes for fading and burst channels," in *Proc. 1980 Zurich Sem. Digital Commun.*, p. 62, 1980.

[62] J. Hagenauer and E. Lutz, "Forward error correction coding for fading compensation in mobile satellite channels," *IEEE J.Select.Areas. Commun.*, vol. 5, pp. 215–225, Feb. 1987.

[63] F. Gagnon, D. Haccoun and C. Leung, "An analysis of convolutional coding on land mobile channels," in *Vehic. Technol. Conf.*, (San Francisco, CA), pp. 666–670, may 1989.

[64] A. N. Trofimov, "Convolutional codes for channels with fading," *Prob. of Inform. Transmission*, vol. 27, pp. 155–165, Oct. 1991.

[65] E. Zehavi and J. K. Wolf, "On the performance of trellis codes," *IEEE Trans. Inform. Theory.*, vol. 33, pp. 196–202, Mar. 1987.

[66] G. Forney, *Concatenated Codes.* Cambridge, MA: M.I.T. Press, 1966.

[67] H. Yamamoto and K. Itoh, "Viterbi decoding algorithm for convolutional codes with repeat request," *IEEE Trans. Inform. Theory.*, vol. 26, pp. 540–547, Sept. 1980.

[68] B.Vucetic, "Concatenated coding schemes for fading channels," *IEEE Trans. Commun.*, vol. 41, pp. 50–61, Jan. 1993.

[69] R. Deng and D. Costello, "High rate concatenated coding systems using bandwidth efficient trellis inner codes," *IEEE Trans. Commun.*, vol. 37, pp. 420–427, May 1989.

[70] S. B. Wicker and L. K. Rasmussen, "A performance analysis for trellis coded hybrid-ARQ protocols," in *ICC'92*, vol. 2, (Chicago), pp. 323.7.1–323.7.5, June 1992.

[71] W. Lindsey, "Error probabilities for Rician fading multichannel reception of binary and n-ary signals," *IRE. Trans. Inform. Theory.*, vol. 10, pp. 339–350, Oct. 1964.

[72] C. Baum and M. Purseley, "Baysian methods for erasure insertion in frequency-hop communication systems with partial-band interference," *IEEE Trans. Commun.*, vol. 40, pp. 1231–1238, July 1992.

[73] D. J. Costello, S. Lin and M. Miller, "Automatic repeat-request error control schemes," *IEEE Comm. Magazine*, vol. 22, pp. 5–17, Dec. 1984.

[74] M. K. Simon. *et al.*, *Spread spectrum communications*, vol. 1. Rockville, Maryland: Computer Science Press, 1985.

[75] P. Y. Kam, "Bit error probabilities of MDPSK over the non-selective Rayleigh fading channel with diversity reception," *IEEE Trans. Commun.*, vol. 39, pp. 220–224, Feb. 1991.

[76] J. Odenwalder, *Optimal decoding of convolutional codes.* PhD thesis, UCLA, Los Angeles, CA, 1970.

[77] G. L. Turin, "The characteristic function of hermitian quadratic forms in complex normal variables," *Biometrica*, vol. 47, June 1960.

[78] S. O. Rice, "Efficient evaluation of integrals of analytic functions by the trapezoidal rule," *Bell Syst. Tech. J.*, vol. 52, pp. 707–722, 1973.

Appendix A

Characteristic Function of a Complex Quadratic

Throughout this thesis, the characteristic function of a complex Gaussian variables in a Hermitian form has been used. The form given in Eq. (3.17) is easily computable, although it disguises the eigenvalues of the weighted covariance matrix. It is often convenient to work with an equivalent form of the characteristic function that is expressed in terms of the eigenvalues of the weighted covariance matrix.

A.1 Characteristic Function

For the sake of completeness, we briefly outline the steps required to obtain the characteristic function of Ξ. As shown in [29, App. B] and [77], it is possible to diagonalize $\mathbf{R}$ and $\mathbf{F}$ simultaneously. Write

$$\mathbf{R} = \mathbf{U}\mathbf{\Lambda}\mathbf{U}^{\dagger} \tag{A.1.1}$$

where $\mathbf{U}$ is a unitary matrix consisting of the $2L$ eigenvectors of $\mathbf{R}$ and $\mathbf{\Lambda}$ is a diagonal matrix whose entries are the corresponding eigenvalues of $\mathbf{R}$. Since $\mathbf{R}$ is positive definite and hence has positive real eigenvalues, it is possible to factorize $\mathbf{\Lambda}$ as

$$\mathbf{\Lambda} = \mathbf{\Psi}^{*}\mathbf{\Psi}^{\mathrm{T}}, \tag{A.1.2}$$

where $\mathbf{\Psi}$ is a diagonal matrix whose entries are the square root of the eigenvalues of $\mathbf{R}$. Then the components of the random vector $\mathbf{V}$ can be made to be independent

by the transformation

$$\mathbf{w} = \mathbf{\Psi^{-1}U^{T}V}. \tag{A.1.3}$$

With this new random vector, the Hermitian form Ξ in Eq. (3.10) becomes $\mathbf{\Xi = w^{\dagger}Tw}$ where

$$\mathbf{T} = \mathbf{\Psi^{\dagger}U^{T}FU^{*}\Psi} = \mathbf{S\Phi S^{\dagger}}, \tag{A.1.4}$$

since $\mathbf{T}$ is also Hermitian and $\mathbf{\Phi}$ is the diagonal matrix of its eigenvalues ϕ_i $i = (1, \cdots, 2L)$. The transformation

$$\eta = \mathbf{S^{\dagger}w} \tag{A.1.5}$$

converts the quadratic form Ξ as $\Xi = \eta^{\dagger}\mathbf{\Phi}\eta$. The mean of the random vector η is given by

$$\langle\eta\rangle = \mathbf{S^{\dagger}\Psi^{-1}U^{T}}\langle\mathbf{V}\rangle. \tag{A.1.6}$$

Now the characteristic function of Ξ is given by [29, (B-3-4)]

$$G_{\Xi}(\nu) = \prod_{i=1}^{2L} \frac{1}{1 - 2j\nu\phi_i} \exp\left[\frac{j\nu\phi_i|\langle\eta_i\rangle|^2}{1 - 2j\nu\phi_i}\right]. \tag{A.1.7}$$

This form of the characteristic function is most suitable for our application at hand, and the associated moment generating function $M_{\Xi}(s)$ is obtained by making the substitution $s = j\nu$. From a computational point of view, this form requires to compute the eigenvalues and eigenvectors of the two Hermitian matrices ($\mathbf{R}$ and $\mathbf{T}$), which can be easily accomplished by the use of a common software package.

Appendix B

Contour Integration

It is of interest to mention the method we use to numerically evaluate the integral of Eq. (3.16). This method is proposed in [32] for computing certain probability distributions in optical communications. From our numerical experiments, we have found it to converge rapidly, easily yielding the desired accuracy.

B.1 Modified Contour

The basic idea is to replace the vertical contour of Eq. (3.16) by a sum of short contours in such a manner that the absolute value of the integrand drops off to zero as rapidly as possible. Such a contour is called the path of steepest descent [37].

From Eqs. (3.16) and (3.17), write the integrand as $\exp(\Psi(s))$ with

$$\Psi(s) = s\langle \mathbf{V} \rangle^{\dagger}(\mathbf{F}^{-1} - 2s\mathbf{R}^{*})^{-1}\langle \mathbf{V} \rangle - \log\ \det(\mathbf{I} - 2s\mathbf{R}^{*}\mathbf{F}) - \log(-s) \qquad \text{(B.1.1)}$$

Since $\Psi(s^{*}) = \Psi^{*}(s)$, and using the above definition, Eq. (3.16) becomes

$$P(\mathbf{x} \rightarrow \hat{\mathbf{x}}) = \ \mathrm{Re}\left[\int_{c_o}^{c_0+j\infty} \exp(\Psi(s))ds/\pi j\right] \qquad \text{(B.1.2)}$$

where c_0 is chosen once again such that $\Psi'(c_0) = 0$. Here the above contour passes through c_0 on the real axis and is parallel to the imaginary axis. As mentioned above, we can deform the above contour to construct the path of steepest descent

consisting of short, straight segments of equal length $|\Delta s| = \delta$. As shown by Rice [78]

$$\Delta s = s_{k+1} - s_k = -\delta \frac{|\Psi'(s_k)|}{\Psi'(s_k)}. \tag{B.1.3}$$

$s_0 = c_0$ and the first segment is vertical. Thus

$$s_1 = s_0 + j\delta. \tag{B.1.4}$$

The initial choice of δ is given as [32]

$$\delta = \frac{1}{2\sqrt{|\Psi''(s_0)|}}. \tag{B.1.5}$$

Now Eq. (B.1.2) becomes

$$P(\mathbf{x} \to \hat{\mathbf{x}}) = \pi^{-1} \operatorname{Re}\left[\sum_{k=0}^{\infty} \int_{s_k}^{s_{k+1}} \exp\left(\Psi(s)\right) ds/j\right]. \tag{B.1.6}$$

Starting with the value of the δ above, each term of this sum can be evaluated using a 5-point formula given in [32]. One can truncate this series at the k-th line segment when the contribution from the k-th term falls below the desired accuracy. Then this summation is repeated for $\delta/2$ and $\delta/4$. We have found this to yield sufficient accuracy.

Appendix C

PDF of the Differential Phase

In this appendix, we derive first order statistics of the differential phase of a shadowed Rician process.

C.1 Derivation

Without any loss of generality, let us write $\alpha_k = \alpha_1$ and $\alpha_{k-1} = \alpha_2$. From the channel gain in (4.1), it follows that the pairs ξ_1, ξ_2 and η_1, η_2 are identically and independently distributed. Thus, their joint PDF is

$$p(\xi_1, \xi_2, \eta_1, \eta_2) = \kappa \exp\left(-\frac{1}{2\sigma_1^2}\left(\xi_1^2 + \xi_2^2 - 2\rho_1\xi_1\xi_2 + \eta_1^2 + \eta_2^2 - 2\rho_1\eta_1\eta_2\right)\right) \quad \text{(C.1.1)}$$

where $\rho_1 = \rho(T_s)$, $\sigma_1^2 = b_0(1-\rho_1^2)$, $\kappa = 1/(4\pi^2 b_0^2(1-\rho_1^2))$.

Let us also introduce the following transformations: $r_1\cos\phi_1 = e^{\zeta_1+\mu_0}+\xi_1$, $r_1\sin\phi_1 = \eta_1$, $r_2\cos\phi_2 = e^{\zeta_2+\mu_0}+\xi_2$, $r_2\sin\phi_2 = \eta_2$. Now it is a simple matter to show that

$$p(r_1, \phi_1, r_2, \phi_2|\zeta_1, \zeta_2) = \kappa r_1 r_2 \exp\left(-\frac{1}{2\sigma_1^2}\Delta_0\right) \quad \text{(C.1.2)}$$

where

$$\Delta_0 = \varrho^2(e^{2\zeta_1} + e^{2\zeta_2} - 2\rho_1 e^{\zeta_1+\zeta_2}) - 2r_1\varrho\cos\phi_1(e^{\zeta_1} - \rho_1 e^{\zeta_2}) \quad \text{(C.1.3)}$$
$$-2r_2\varrho\cos\phi_2(e^{\zeta_2} - \rho_1 e^{\zeta_1}) - 2\rho_1\cos\varphi r_1 r_2 + r_1^2 + r_2^2$$

where $\varphi = \phi_1 - \phi_2$ is the differential phase in which we are interested. To derive (C.1.2), we have made use of the fact that A_k in (4.1) is a lognormal variable. Moreover, according to the shadowed Rician model, ζ_1 and ζ_2 are jointly distributed as

$$p(\zeta_1, \zeta_2) = \frac{1}{2\pi d_0 \sqrt{1-\rho_1^2}} \exp\left(-\frac{1}{2d_0(1-\rho_1^2)}\left(\zeta_1^2 + \zeta_2^2 - 2\rho_1\zeta_1\zeta_2\right)\right). \tag{C.1.4}$$

Once again, we note that the term $1/(2d_0(1-\rho_1^2))$ will be quite large for both light and average shadowed fading cases. Therefore, an approximate expansion for the average of (C.1.2) with respect to (C.1.4) can be obtained via Laplace's method in two dimensions. In [37, 8.2.] it is shown that an integral of the form

$$I(\lambda) = \int_{\mathcal{D}} \exp\{\lambda\phi(\mathbf{x})\} g_0(\mathbf{x}) d\mathbf{x}, \quad \mathbf{x} = (x_1, x_2), \tag{C.1.5}$$

can be approximated as

$$I(\lambda) \approx \frac{2\pi}{\lambda} \frac{g_0(\mathbf{x}_0)\exp\{\phi(\mathbf{x}_0)\}}{(\phi_{x_1x_1}(\mathbf{x}_0)\phi_{x_2x_2}(\mathbf{x}_0) - \phi^2_{x_1x_2}(\mathbf{x}_0))^{1/2}}, \quad \text{as } \lambda \to \infty, \tag{C.1.6}$$

where $\mathbf{x}_0$ is an interior critical point of $\phi(\mathbf{x})$.

The critical point of our function (C.1.4) is $(0,0)$; Thus, we conclude from (C.1.6) that

$$p(r_1, \phi_1, r_2, \phi_2) \approx \kappa r_1 r_2 \exp\left(-\frac{1}{2\sigma_1^2}\Delta_1\right) \tag{C.1.7}$$

where

$$\begin{aligned}\Delta_1 = {} & 2\varrho^2(1-\rho_1) - 2r_1\varrho\cos\phi_1(1-\rho_1) - 2r_2\varrho\cos\phi_2(1-\rho_1) \\ & -2\rho_1\cos\varphi r_1 r_2 + r_1^2 + r_2^2.\end{aligned}$$

We can convert this into the sum of a bivariate quadratic of r_1 and r_2 and an expression of ϕ_1 and ϕ_2, thereby enabling the integration of (C.1.7) over r_1 and r_2.

We then have

$$p(\phi_1,\phi_2) \approx \kappa_1 \left(\frac{b_0(1-\rho_1^2)\rho_1 \cos\varphi}{(1-\rho_1^2\cos^2\varphi)^{1.5}} + \frac{\varrho^2(1-\rho_1)^2}{(1-\rho_1^2\cos^2\varphi)^{2.5}}\Delta_2 \right) \exp\frac{-\varrho^2}{2b_0(1+\rho_1)}\Delta_3 \tag{C.1.9}$$

where $\kappa_1 = 1/(2\pi b_0)$,

$$\Delta_2 = \left(\rho_1\cos\varphi\cos^2\phi_1 + (1+\rho_1^2\cos^2\varphi)\cos\phi_1\cos\phi_2 + \rho_1\cos\varphi\cos^2\phi_2\right), \tag{C.1.10}$$

and

$$\Delta_3 = 2 - \frac{1-\rho_1}{(1-\rho_1^2\cos^2\varphi)}\left(\cos^2\phi_1 + 2\rho_1\cos\varphi\cos\phi_1\cos\phi_2 + \cos^2\phi_2\right). \tag{C.1.11}$$

Our aim is to find the PDF of $\varphi = \phi_1 - \phi_2$. As defined, φ can vary from -2π to 2π; however, it is desirable to confine φ from $-\pi$ to π. To do this, we use a method given in [1, 1.5.4]. Thus, finally we have

$$p(\varphi) = \int_0^{2\pi} p(\phi_1, \varphi+\phi_1)d\phi_1, \quad -\pi \le \varphi \le \pi. \tag{C.1.12}$$

Appendix D

Bounding the Eigenvalues

Here we would like to prove one case that supports the conjecture that the largest positive eigenvalue of $\mathbf{R}^*\mathbf{F}$ does not increase above the limit given by (5.31) as q changes from $q = 0$ to $q > 0$. We prove this only for error events of length two and ideal coherent detection.

D.1 Derivation

Consider an error event of length two between $\mathbf{x} = (1,1)$ and $\hat{\mathbf{x}} = (x_1, x_2)$. In this case the covariance matrix for an exponential correlation function Eq. (2.13) is

$$\mathbf{R} = \begin{pmatrix} b_0 & b_0 & b_0 q & b_0 q \\ b_0 & b_0 + \sigma^2 & b_0 q & b_0 q \\ b_0 q & b_0 q & b_0 & b_0 \\ b_0 q & b_0 q & b_0 & b_0 + \sigma^2 \end{pmatrix}. \tag{D.1.1}$$

To find the eigenvalues of $\mathbf{R}^*\mathbf{F}$ the determinant of the following matrix is equated to zero.

$$\mathbf{R}^*\mathbf{F} - \phi\mathbf{I} = \begin{pmatrix} \delta_1 b_0 - \phi & \delta_1^* b_0 & b_0 q \delta_2 & b_0 q \delta_2^* \\ \delta_1(b_0 + \sigma^2) & b_0\delta_1^* - \phi & b_0 q \delta_2 & b_0 q \delta_2^* \\ b_0 q \delta_1 & b_0 q \delta_1^* & b_0\delta_2 - \phi & b_0\delta_2^* \\ b_0 q \delta_1 & b_0 q \delta_2^* & \delta_2(b_0 + \sigma^2) & b_0\delta_2^* - \phi \end{pmatrix} \tag{D.1.2}$$

where $\delta_1 = x_1 - 1$ and $\delta_2 = x_2 - 1$. After some manipulation, it can be shown that

$$\det(\mathbf{R}^*\mathbf{F} - \phi\mathbf{I}) = D_1(\phi)D_2(\phi) - b_0^2 q^2(\phi - \sigma^2)^2 \tag{D.1.3}$$

where

$$D_1(\phi) \triangleq \phi^2 + b_0|\delta_1|^2\phi - b_0|\delta_1|^2\sigma^2, \tag{D.1.4}$$
$$D_2(\phi) \triangleq \phi^2 + b_0|\delta_2|^2\phi - b_0|\delta_2|^2\sigma^2.$$

Denote by ϕ_{1+} and ϕ_{2+} the two positive roots of $D_1(\phi) = 0$ and $D_2(\phi) = 0$. From (5.31), $\max(\phi_{1+}, \phi_{2+}) < \sigma^2$. Let ϕ_+ denote the maximum positive root of (D.1.3), which satisfies the condition

$$D_1(\phi_+)D_2(\phi_+) = b_0^2q^2(\phi_+ - \sigma^2)^2 \tag{D.1.5}$$

By considering the graphs of these two curves (left and right sides of the equality sign), it can be shown that the solution ϕ_+ satisfies (5.31).

Appendix E

Approximate Determinant

We wish to find the determinant of $\mathbf{R}$, denoted by D_L, as defined in (5.9). For this purpose, it is assumed that the positions of differing code symbols are adjacent (see page 85) in error events between codewords.

E.1 Derivation

For $L = 2$, we have the following matrix

$$\mathbf{R} = \begin{pmatrix} b_1 & \mu\sqrt{b_0 b_1} & b_0 q & b_0 q \\ \mu^*\sqrt{b_0 b_1} & b_0 + \sigma^2 & b_0 q & b_0 q \\ b_0 q & b_0 q & b_1 & \mu\sqrt{b_0 b_1} \\ b_0 q & b_0 q & \mu^*\sqrt{b_0 b_1} & b_0 + \sigma^2 \end{pmatrix} \tag{E.1.1}$$

whose determinant is found to be

$$D_2 = b_1^2((1-\mu^2)b_0 + \sigma^2) - b_0^2 q^2 (2\mu\sqrt{b_0 b_1} - b_0 - b_1 - \sigma^2)^2. \tag{E.1.2}$$

Considering $L = 3$, we have the following:

$$\mathbf{R} = \begin{pmatrix} b_1 & \mu\sqrt{b_0 b_1} & b_0 q & b_0 q & b_0 q^2 & b_0 q^2 \\ \mu^*\sqrt{b_0 b_1} & b_0 + \sigma^2 & b_0 q & b_0 q & b_0 q^2 & b_0 q^2 \\ b_0 q & b_0 q & b_1 & \mu\sqrt{b_0 b_1} & b_0 q & b_0 q \\ b_0 q & b_0 q & \mu^*\sqrt{b_0 b_1} & b_0 + \sigma^2 & b_0 q & b_0 q \\ b_0 q^2 & b_0 q^2 & b_0 q & b_0 q & b_1 & \mu\sqrt{b_0 b_1} \\ b_0 q^2 & b_0 q^2 & b_0 q & b_0 q & \mu^*\sqrt{b_0 b_1} & b_0 + \sigma^2 \end{pmatrix} \tag{E.1.3}$$

which can be transformed to the following:

$$\mathbf{R} = \begin{pmatrix} b_1 & \mu\sqrt{b_0 b_1} & b_0 q & b_0 q & b_0 q^2 & 0 \\ \mu^*\sqrt{b_0 b_1} & b_0 + \sigma^2 & 0 & 0 & 0 & 0 \\ b_0 q & b_0 q & b_1 & \mu\sqrt{b_0 b_1} & b_0 q & 0 \\ 0 & 0 & \mu^*\sqrt{b_0 b_1} & b_0 + \sigma^2 & 0 & 0 \\ b_0 q^2 - b_1 & b_0 q^2 - \mu\sqrt{b_0 b_1} & 0 & 0 & b_1 - b_0 q^2 & \mu\sqrt{b_0 b_1} - b_1 \\ 0 & 0 & 0 & 0 & \mu^*\sqrt{b_0 b_1} - b_1 & t1 \end{pmatrix} \tag{E.1.4}$$

where

$$t1 = b_0 + b_1 + \sigma^2 - 2\mu\sqrt{b_0 b_1} \tag{E.1.5}$$

Expanding this determinant from the bottom right hand corner, we get

$$D_3 \approx \left[(b_1 - b_0 q^2)(b_0 + b_1 - 2\mu\sqrt{b_0 b_1}) - (b_1^2 - 2\mu b_1\sqrt{b_0 b_1} + \mu^2 b_0 b_1)\right] D_2 \tag{E.1.6}$$

Here we use the approximation sign because two terms of the expansion have been neglected. The neglected terms tend to zero as $q \to 0$ and $\sigma^2 \to 0$.

Continuing in this manner, we get

$$D_L \approx \left[(b_1 - b_0 q^2)(b_0 + b_1 - 2\mu\sqrt{b_0 b_1}) - (b_1^2 - 2\mu b_1\sqrt{b_0 b_1} + \mu^2 b_0 b_1)\right]^{L-2} D_2 \tag{E.1.7}$$